Design and Fabrication of RF MEMS Devices for Wide-Band VHF Applications

Munira Bengashier

Supervisor: Prof. Ivan Grech
Co- Supervisor: Owen Casha

May 2024

Submitted in partial fulfilment of the requirements

for the degree of Doctor of Philosophy

L-Universita' ta' Malta
Faculty of Information & Communication Technology
Department of Microelectronics and Nanoelectronics

Dedicated to my family,

my parents, my two daughters

and especially, my husband Mohamed.

COPYRIGHT NOTICE

DECLARATION OF AUTHENTICITY

ICT-2024-00185

Munira Bengashier

Doctor of Philosophy (Faculty of ICT)

Title of Dissertation:

Design and Fabrication of RF MEMS Devices for Wide-Band VHF Applications.

(a) Authenticity of Dissertation

I hereby declare that I am the legitimate author of this dissertation and that it is my original work. No portion of this work has been submitted in support of an application for another degree or qualification of this or any other university or institution of higher education. I hold the University of Malta harmless against any third party claims with regard to copyright violation, breach of confidentiality, defamation and any other third party right infringement.

(b) Research Code of Practice and Ethics Review Procedure

I declare that I have abided by the University's Research Ethics Review Procedures. As a Ph.D. student, as per Regulation 49 of the Doctor of Philosophy Regulations, I accept that my thesis be made publicly available on the University of Malta Institutional Repository.

____

MUNIRA BENGASHIER

____

Date

___31/May/2024___________________

LIST OF PUBLICATIONS

The peer-reviewed conference publications that came from this research project are listed below.

- M. Bengashier, I. Grech, O. Casha, B. Portelli, R. Farrugia and E. Gatt, **"A Feasibility Study on Piezoelectric MEMS Lateral Bulk Acoustic Wave Resonators including Thermal Effect,"** 2019 Symposium on Design, Test, Integration & Packaging of MEMS and MOEMS (DTIP), Paris, France, 2019.
- M. Bengashier, I. Grech, O. Casha, B. Portelli, and R. Farrugia, "**Experimental Validation of Tuning Mechanisms Applied on Aln Piezoelectric Contour Mode Mems Resonators",** 2020 Symposium on Design, Test, Integration & Packaging of MEMS and MOEMS (DTIP)*, Paris, France 2020.*
- M. Bengashier, I. Grech, O. Casha, R. Farrugia and B. Portelli, **"Investigation of a Mechanical Contact Type RF-MEMS Switch for VHF Band Applications,"** 2021 Symposium on Design, Test, Integration & Packaging of MEMS and MOEMS (DTIP), Paris, France, 2021.
- M. Bengashier, I. Grech, O. Casha, R. Farrugia and B. Portelli, **"Mechanical Contact Type RF-MEMS Switches for Microwave Band Applications,"** 2023 Symposium on Design, Test, Integration & Packaging of MEMS and MOEMS (DTIP), Valletta, Malta.

Piezoelectric actuated MEMS Resonators for low VHF applications

ABSTRACT

This Ph.D. research work investigates the potential application of PiezoMUMPs technology to the design of a Lateral Bulk Acoustic Piezoelectric MUMPs (LBAW PiezoMUMPs) resonators that can operate in the VHF band. By analysing the effects of resonator size, number of electrode elements, and tether shape on parameters like resonant frequency and Quality factor (Q_f). This work is based on analytical, Finite Element simulations, validated by prototype characterisation.

Fine tuning through is essential in order to compensate for process related variation, for this reason thermal tuning using both ovenisation as well as on chip electrothermal tuning was investigated. Furthermore, volage tuning was also evaluated. Tuning via ovenisation achieved a tuning range of 300KHz over temperature range of 273 to 573K. Voltage tuning achieved a 30KHz over a range of 1 to 9 V. Electrothermal tuning resulted a 50KHz range for a thermal power of 50mW. This part of the study showed that thermal tuning results in a wider tuning range than voltage tuning.

The study also investigates mechanical contact type RF-MEMS switches for VHF band applications, implemented on the same PiezoMUMPs process, in order to achieve a cost-effective wide frequency tuning. In this investigation, several electrostatically actuated switches, having different signal contact profiles were analytically studied and simulated using CoventorWare FEM software. These switches were optimized for different parameters depending on the design geometry and actuator comb fingers. Subsequently, different switch prototype configurations such as 1-way including the deep off option, as well as 2-way structures have been manufactured and characterised.

ACKNOWLEDGMENTS

Firstly, I thank my spouse Mohamed for his assistance, patience, and motivational remarks during my doctoral study.

I owe much of my success to my parents, who gave their all to make sure I had everything I needed to fulfil my ambitions. I also want to thank my mother for her support and prayers throughout this educational experience.

I extend my gratitude to my friends, Gihan Morabet for her sociological and emotional support, as well as Dr. Russell Farrugia and Dr. Barnaby Portelli for their invaluable assistance in establishing the optical characterization facility and for our many conversations during my studies.

My sincere appreciation goes extended to my Ph.D. supervisor, Professor Ivan Grech, for his priceless advice and direction. Additionally, I want to thank Professor. Owen Cacha, my co-supervisor, for all his assistance and support throughout this study.

The Ministry of Higher Education and Scientific Research in Libya as part of the National Programme funded this research for Increasing Universities' International Competitiveness. Gratitude owed to everyone who provided this support.

Finally, I express my gratitude to the Department of Micro & Nanoelectronics for providing me with access to their resources and expertise in the fields of MEMS design and fabrication.

Table of Contents

Table of Contents i

List of Figures v

List of Tables x

Nomenclature xii

List of Acronyms xiii

1. Introduction 1

1.1 Motivation 2

1.1.1 PiezoMUMPs Resonators 3

1.1.2 Electrostatic Actuated Switches 3

1.2 Existing Research Problem 4

1.3 Proposed Solution 4

1.4 Thesis Outline 5

2. Literature Review on RF MEMS Devices 7

2.1 RF MEMS Actuation Mechanisms 7

2.1.1 Electrostatic Actuation 8

2.1.2 Piezoelectric Actuation 9

2.2 Piezoelectricity and Piezoelectric Principles 10

2.2.1 Piezoelectricity in Concept 11

2.2.2 Piezoelectric Materials 12

2.3 Resonator Mechanical-Electrical Modelling 14

2.3.1 One-Port Piezoelectric Resonator Electrical Model 18

2.3.2 Two-Port Piezoelectric Resonator Electrical Model 19

2.4 Acoustic Wave and Vibration Modes at Resonance 20

2.4.1 Surface Acoustic Wave (SAW) 21

2.4.2 Flexural Mode 21

2.4.3 Torsional Mode 22

2.4.4. Bulk Acoustic Wave (BAW) 23

2.4.5 Shear Mode 25

2.5 Piezo MEMS Resonators Performance Measures 26

2.5.1 The Quality Factor (Q_f) 27

2.5.2 The Piezoelectric Coupling Factor 28

2.6 State of Art on Piezo MEMS Resonators 31

2.7 Performance Control in RF MEMS Resonators 32

2.7.1 Tuning...32

2.7.2 Trimming...33

2.8 Piezoelectric MUMPS Resonators...34

2.8.1 PiezoMUMPs Fabrication Steps 34

2.9 MEMS Simulation Tools...36

2.10 RF MEMS Switches 37

2.10.1 Electrostatic RF MEMS Switches 41

2.10.2 State of Art of Electrostatic RF MEMS Switches 43

2.11 Research Gap 44

3. Design Optimization Issues for LBAW MEMS Resonators.....................................45

3.1 Design Methodology 45

3.2 Design Steps and Simulation Analyses 46

3.3 LBAW PiezoMUMPs Resonator..49

3.3.1 Mesh Study for 1st Mode LBAW PiezoMUMPs Resonator 49

3.2.2 DC Analyses for LBAW Piezo MUMPs Resonator..51

3.2.3 Harmonic Analysis for LBAW PiezoMUMPs Resonator......................................52

3.3.4 Quality Factor (Q_f) Analysis 53

3.4 LBAW PiezoMUMPs Resonator Design Adjustments 56

3.4.1 Electrodes Dimension Adjustment 56

3.4.2 Resonator Dimension Adjustment...56

3.4.3 DC and Harmonic Analysis Comparison 57

3.4.4 LBAW PiezoMUMPs Resonators / Different Numbers of Electrode Elements 58

3.5 Mesh Study for the 5th Mode LBAW PiezoMUMPs Resonator.......................59

3.5.1 Modal frequency separation versus resonator width variation 62

3.6 Impact of Resonator Parameter Variations on Q_f.......................64

3.6.1 Effect of Number of Electrode Fingers 64

3.6.2 Variation in Q_f due to resonator width.......................65

3.6.3 The Variation in The Resonator's Length-to-Width ratio Impact.......................66

3.6.4 Tether Geometry Variation 67

3.6.4.2 Tether Curvature.......................69

3.7 LBAW PiezoMUMPs Resonators Prototype Fabrication.......................71

3.7.1 Fabrication Results 71

3.7.2 Characterisations of LBAW PiezoMUMPs Resonators.......................74

3.7.3 Discussion 82

4. Tunability Techniques for LBAW PiezoMUMPs Resonators.......................84

4.1 Theory and Analytical results on LBAW PiezoMUMPs Resonators.......................85

4.1.1 Material Property and Temperature Effect 85

4.1.2 Analytical Results.......................86

4.2 Temperature Variation Effect on SOI Layer Using FEM 88

4.2.1 Analytical and FEM Simulations Results Comparison.......................88

4.2.2 Temperature Variation Effect on PZTMEMS and PiezoMUMPs Resonators 89

4.2.3 Quality Factor 91

4.3 Design and Simulation of the 5th order PiezoMUMPs resonator.......................91

4.4 Experimental Validation of Tuning Mechanisms.......................94

4.4.1 Fabrication and Characterisation 94

4.4.2 Fine Tuning in LBAW PiezoMUMPs Resonator.......................96

4.5 Discussion....................... 105

5. Electrostatically- Actuated Switches Using PiezoMUMPs.......................106

5.1 Design Concept and Process Description 108
5.2 Design steps and Geometry Adjustments 110
5.2.1 Switch Pull-in 110
5.2.2 Switch Spring Design 112
5.3 Comparison 113
5.3.1 Three-State Switch Design 113
5.3.2 Two-State Low-Voltage Switch Design 114
5.4 Switch Optimization 115
5.4.1 Actuation Electrode Design Optimization and The Pull-in Voltage 115
5.4.2 Signal Line Contact Surface Profile 117
5.5 Fabrication and Testing 118
5.5.1 Non-Wire Bonded Switches Prototypes 118
5.5.2 Wire Bonded Switches prototypes 122
5.6 Discussion 127
6. Conclusions and Future Work 130
6.1 Conclusions 130
6.2 Future work 132
REFERENCES 134

List of Figures

Figure. 2. 1: Parallel plate capacitor structure used in electrostatic actuation [14, 32]...............8
Figure. 2. 2: Electrostatic comb-drive configurations: (a) Longitudinal comb actuator; (b) Transverse actuator [14, 28-32]..9
Figure. 2. 3: Schematic diagram of the piezoelectric actuator [14, 35]..................................10
Figure. 2. 4: A simplified layout of piezoelectric modes, (a) d_{31} mode, (b) d_{33} mode [40].......12
Figure. 2. 5: The energy flow mechanism in the piezoelectric resonator [42]. 15
Figure. 2. 6: Modelling from mechanical to electrical representations [48]............................15
Figure. 2. 7: The Typical Mason lumped circuit model for a piezoelectric transducer (one port) [39]...17
Figure. 2. 8: The BVD electrical representation for a one-port piezoelectric resonator referred to the primary side of the transformer [39,50,51,52]..19
Figure. 2. 9: The schematic viewgraph of a two-port piezoelectric resonator [39]. 19
Figure. 2. 10: The electrical model of the two-port piezoelectric resonator [39,50, 54]……...20
Figure. 2. 11: Acoustic wave energy travels along the surface of the surface layer of the resonator [49]...21
Figure. 2. 12: General types of flexural modes according to their boundary conditions: Clamped End, (b) Clamped –Clamped, (c) Free – Free [5]……………………………….................22
Figure. 2. 13: Torsional mode in paddle resonator [5]..22
Figure. 2. 14: The acoustic wave standing through the thickness of the resonator’s piezoelectric layer [49]. 23
Figure. 2. 15: Different bulk mode shapes in different resonators; a) length-extensional (LE), (b) width-extensional (WE) modes in rectangular plates,(c) square-extensional (SE) mode in square plates, (d) radial breathing mode in circular disks [5]...25
Figure. 2. 16: Lateral shear mode; (a) Lame, (b) Face shear, (c) Wine glass mode [5,55,58,59]. 25
Figure. 2. 17: A one-port TPoS resonant structure [39]..26
Figure. 2. 18: The typical impedance measurement for a one-port piezoelectric resonator [39]. 30
Figure. 2. 19: Cross sectional view including all material’s layers in PiezoMUMPs Process file [7]...35
Figure. 2. 20: TRENCH to SOI overlay tolerance [7]. 36
Figure. 2. 21: CoventorWare design flows [90]. 37
Figure. 2. 22: Primary design of a 3 state non-contact Switch, including spring shape [9]. 41

Figure. 3. 1: The 3D model of RES1_2E based on the PiezoMUMPs technology using CoventorWare (RES1_2E). 46
Figure. 3. 2: Resonator simulation steps using CoventorWare simulation toolkit...................48
Figure. 3. 3: Mesh used for simulating the resonant frequency of RES1_2E..........................50
Figure. 3. 4: 1st resonant mode mesh convergence Study for LBAW PiezoMUMPs (RES1_2E). 51
Figure. 3. 5: 1st resonant mode lateral deformation of RES1_2E. 52
Figure. 3. 6: A 3-D model of one side of the substrate used in the FEM simulation on RES1_2E, applying symmetry boundary conditions and the same mesh size. 55
Figure. 3. 7: 1st resonant mode of Res1_2E_V2 with Large Electrode Elements.....................56
Figure. 3. 8: 1st resonant mode of RES2_2E_V2 with Large Electrode Elements...................57
Figure. 3. 9: Mem-Mech model analysis with mesh setting for 5E-electrode LBAW............60
Figure. 3. 10: A mesh Convergence study was conducted for the LBAW PiezoMUMPs resonator (RES3_5E_TH) in the 5th mode...60
Figure. 3. 11: 5th Mode Mesh *Qf* convergence study for LBAW PiezoMUMPs resonator with substrate..62
Figure. 3. 12: The frequency separation of RES3_5E_V1's 5th resonant mode with varying widths measured in µm. 63
Figure. 3. 13: The average frequency separation frequency of the 5th resonant mode applied on RES3_5E_V1. 64
Figure. 3. 14: Comparison between the *Qf* value of RES3_5E_V1 at 5th mode versus different resonator's width..66
Figure. 3. 15: Figure. 3. 0.1: Comparison between the *Qf* value at 5th mode versus different resonator's W/L %...67
Figure. 3. 16: The 3D model Re (Displacement X) at 5th resonant mechanical mode............69
Figure. 3. 17: Five-element electrode LBAW PiezoMUMPs resonator (RES3_5E_CT). 70
Figure. 3. 18: GDS layout of a five-element electrode LBAW PiezoMUMPs resonator at the 5th resonant mode with curved Tether (RES3_5E_CT). 70
Figure. 3. 19: RES2_2E_Th, LBAWPiezoMUMPs resonator including thermal elements.... 72
Figure. 3. 20: A GDS layout of 2E_elctorods PiezoMUMPs resonator including thermal elements..72
Figure. 3. 21: Micrograph of Two ports PiezoMUMPs resonators, including thermal elements. 73
Figure. 3. 22: Fabricated PCB layouts. 74
Figure. 3. 23: Micro-photo of the fabricated LBAW PiezoMUMPs resonators (a) 2-element, (b) 3-element, and (c) 5-element electrode versions...76

Figure. 3. 24: Measurement of S21 transmission parameter for the fabricated LBAW PiezoMUMPs resonators (a) 2-element, (b) 3-element, and (c) 5-element electrode versions..71

Figure. 3. 25: Micro-photo of the fabricated RES2_5E_TH and its measurement of S21 transmission parameter…………………………………………………………………...78

Figure. 3. 26: Micro-photo of the fabricated RES3_5E_V2 and its measurement results of S_{21} transmission parameter…………………………………………………………………….. 79

Figure. 3. 27: Micro-photo of the fabricated RES3_5E_CT and its measurement results of S_{21} transmission parameter……………………………………………………………………… 80

Figure. 3. 28: Micro-photo of the fabricated RES3_5E_V3 _CT and its measurement results of S_{21} transmission parameter……………………………………………………………… 80

Figure. 3. 29: Micro-photo of the fabricated RES3_5E_V4 and its measurement results of S_{21} transmission parameter..81

Figure. 3. 30: Micro-photo of the fabricated RES4_5E_V3 and measurement results of S_{21} transmission parameter..81

Figure. 3. 31: Micro-photo of the fabricated RES4_5E_V3 and measurement results of S_{21} transmission parameter..82

Figure. 4. 1: Almost linear decrease in silicon's Young's modulus 87

Figure. 4. 2: Analytically derived 1st mode resonant frequency variation with 88

Figure. 4. 3: Comparison between FE and analytical results for the resonant 89

Figure. 4. 4: Comparison of the 1st mode resonant frequency versus temperature change for the PZTMEMS when only the SOI layer is included and when all layers are included. 90

Figure. 4. 5: Comparison of the 1st mode resonant frequency versus temperature change for the PiezoMUMPs when only the SOI layer is included and when all layers are included. 90

Figure. 4. 6: Simplified diagram of the rectangular resonator outlining the pads used for voltage tuning including two current heating elements. 92

Figure. 4. 7: Modal Analysis shows the 5th mode shape having 93

Figure. 4. 8: Micrograph of the designed and fabricated (RES2_5E_TH) 95

Figure. 4. 9: The PCB having the fabricated die interfaced through SMI connectors. 95

Figure. 4. 10: Plot of the transmittance spectrum |S21| for the 5th mode (f_{res} simulation = 60.367 MHz, f_{res} measured = 61.348 MHz). 96

Figure. 4. 11: (a) Linear decrease in the resonant frequency (simulation and measured) versus temperature for the range of 278-358 K. (b) shows the measured transmission magnitude plots for different temperatures in steps of 5 K. 98

Figure. 4. 12: Simplified diagram of the rectangular resonator (RES3_5E_CT) 100

Figure. 4. 13: Micrograph of the designed and fabricated LBAW PiezoMUMPs resonator

including two electrothermal elements. 100
Figure. 4. 14: The electrical circuit for current in mA variation using variable resistance in KΩ in series with two thermal electric element’s and RES3_5E_CT in a MEMS Chip. 101
Figure. 4. 15: The transmission magnitude plots for different heating current mA. 102
Figure. 4. 16: Linear decrease in the resonant frequency (measured) 102
Figure. 4. 17: Change in the resonant frequency (measured) versus 103
Figure. 4. 18: SOI bulk resistance almost constant over electrical heating power range. 103
Figure. 4. 19: (a) Monotonic decrease in the resonant frequency over a voltage tuning range of 1-9 V. (b) The transmission magnitude plots for different tuning voltages in steps of 1V. 104

Figure. 5. 1: Three state non-contact one direction switch (SW1_1D_3S_FL_1_V0). 106
Figure. 5. 2: Three state non-contact one direction switch (SW1_1D_3S_FL_7_V2). 109
Figure. 5. 3: Two state,two-way (double throw) switch (SW2_2D_2S_FL_7_V2). 109
Figure. 5. 4: Cross-section of the designed switch and resonator. 110
Figure. 5. 5: Maximum displacement versus actuation voltage for (i) the 7-finger comb actuator, 3-state switch (SW2_2D_3S_FL_7_V2) and (ii) the 14-finger comb actuator, 2-state switch (SW3_1D_2S_FL_14_V1) 115
Figure. 5. 6: One direction-actuated Switch (SW3_1D_2S_FL_14_V1). 116
Figure. 5. 7: Two direction-actuated Switch (SW2_2D_3S_FL_7_V2). 116
Figure. 5. 8: The two state, two-way (double throw) switch for two different resonant PiezoMUMPs Resonators (SW4_2D_2S_2FL_7_V1). 117
Figure. 5. 9: Micro-photograph of the fabricated three-state one direction switch ((SW1_1D_3S_FL_14_V1)) with a 14-finger comb actuator. 119
Figure. 5. 10: Micro-photograph of the low voltage optimized switch (SW3_1D_2S_FL_14_V1) integrated with the Piezo lateral bulk acoustic wave resonator. 119
Figure. 5. 11: Experimental setup for the (SW3_1D_2S_FL_14_V1) two-state low voltage switch. 120
Figure. 5. 12: The two-state low voltage switch (SW3_1D_2S_FL_14_V1) in actuated ON state. 121
Figure. 5. 13: The three -state low voltage switch (SW2_1D_3S_FL_7_V4) in actuated ON state. 121
Figure. 5. 14: PCB designed for one of the fabricated MEMS switch under the microscope during the characterization experiment of (SW2_2D_3S_FL_7_V4) switch. 122
Figure. 5. 15: (SW2_2D_3S_FL_7_V4) with flat signal line surface profile 123
Figure. 5. 16: SW2_2D_3S_TL_7_V4 with trapezoidal signal line conact surface profile. ... 123

Figure. 5. 17: Micro-photographs of (SW2_2D_3S_FL_7_V4): (a) Comb fingures "ON state", (b) Comb fingures "OFF State", (c) Signal line ON State Flat contact surface, Signal line OFF State Flat contact surface……………………………….……………….124
Figure. 5. 18: Micro-photographs of (SW4_2D_2S_2TL_7_V1) (a) One pare of Signal lines at ON State, (b) Both Signal lines at OFF State, "trapezoidal contact surface 125
Figure. 5. 19: The insertion loss for (a) (SW2_2D_3S_FL_7_V4) the flat contact and (b) SW2_2D_3S_TL_7_V4 the trapezoidal contact. 126
Figure. 5. 20: Scanning electron micrograph (SEM) of the fabricated die orientated 45°...... 127
Figure. 5. 21: SEM Image of the fabricated (SW2_2D_3S_FL_7_V4) SL flat contact area.. 127
Figure. 5. 22: Vertical SEM Image of the fabricated Signal Line (SL) finger, showing the DRIE scallop profile. 128
Figure. 5. 23: Diagram showing the two scalloped DRIE surfaces in contact, where the air gap diameter (2r) is estimated to be 0.33 μm. 128

List of Tables

Table.2. 1: Commonly used piezoelectric materials along with their performance parameters [40, 43]....14
Table.2. 2: Mechanical and electrical variable translation Table [39]....18
Table.2. 3: Two main groups of sources of loss [42]....27
Table.2. 4: The maximum piezoelectric coupling factor, for the most commonly used piezoelectric materials in resonator fabrication [39,64, 65]....29
Table.2. 5: Reported Thin-Film Piezo-actuated MEMS resonators, including year of publication, technology used, resonant modes....31
Table.2. 6: Tuning in PiezoMEMS Resonators....34
Table.2. 7: Latest Research on PiezoMUMPs resonators....36
Table.2. 8: Contact-type switches reliability problems [8]....41
Table.2. 9: The development of MEMS switches over the past 27 years in 43

Table.3. 1: Resonator Notation along variations in resonator geometry, tether structure, number of electrode elements, and thermal elements existence....47
Table.3. 2: Mesh convergence on the 1st Resonant mode of RES1_2E....50
Table.3. 3: Four different LBAW PiezoMUMPs resonators and their geometry variations....57
Table.3. 4: DC and Harmonic Analysis for LBAW PiezoMUMPs Resonators....58
Table.3. 5: LBAW PiezoMUMPs resonators with different electrode elements....58
Table.3. 6: Resonator geometry parameters, including layer thickness....59
Table.3. 7: Mesh convergence on the 5th mode LBAW PiezoMUMPs resonator (RES3_5E_TH)....60
Table.3. 8: Resonant frequency and Q_f values obtained from the mesh convergence study of the designed resonator during anchor losses analysis....61
Table.3. 9: The 5th mode frequency modal separation versus width variation RES3_5E_V1...63
Table.3. 10: Number of electrode elements effect on resonance frequency and Q_f....65
Table.3. 11: Q_f value of RES3_5E_V1 versus width variation....66
Table.3. 12: Q_f versus different resonator's (width/ length %) at resonant frequency....67
Table.3. 13: Q_f value at 5th resonant mode under the effect of tether geometry....71
Table.3. 14: Characterisation results obtained for three LBAW PiezoMUMPs resonators having different number of electrode elements: (a) 2-element, (b) 3-element, and (c) 5-element electrode versions....75
Table.3. 15: The 5th resonant mode for different LBAW PiezoMUMPs resonators....83

Table.4. 1: Extracted lumped circuit's parameters BVD - Fast PZE Results [121]..................94
Table.4. 2: Total resistance in series (Rs) effect on resonant frequency, ...101

Table.5. 1: The nomenclature of different switches discussed in the current Chapter. 108
Table.5. 2: Three different designs of a 3 state non-contact Switch, (a), (b), (c). 111
Table.5. 3: Different designs of a 2, 3 state non-contact Switch. 112
Table.5. 4: Design Parameters of (SW3_1D_2S_FL_14_V1). 113
Table.5. 5: Operation of the three-state switch. 114
Table.5. 6: Different signal line surface profiles for a two state switch SW2_2D_2S_FL_7_V3 : (a) Flat SW2_2D_2S_FL_7_V4, (b) Zigzag SW2_2D_2S_ZL_7_V3, (c) Trapezoidal SW2_2D_2S_TL_7_V4. 118
Table.5. 7: Measurements carried out using a 100X lens 120
Table.5. 8: Simulated and measured pull-in voltages. 122
Table.5. 9: Simulated capacitance values for different SL surface 129

Nomenclature

Symbol	SI Units	Description
D	[C/m^2]	Electrical Displacement
E_f	[V/m]	Electric Field Strength
T	[N/m2]	Stress
S	[m/m]	Strain
d, d_{31}, d_{33}	[C/N]	Piezoelectric coefficient 'Strain Factor'
ε_r	[F/m]	Dielectric constant 'Relative Permittivity'
s	[Pa^{-1}]	compliance
d^t	[C/N]	The piezoelectric coefficient matrix
s^E	[Pa^{-1}]	Compliance matrix
ε	[F/m]	Permittivity of the material
ε_0	F/m]	Permittivity of free space
e	[C/m^2]	Piezoelectric constant
e_{31}, e_{33}	[C/m^2]	Piezoelectric constant at normal stress mode
d_{15}	[C/N]	Piezoelectric coefficient at shear stress mode
E	[GPa]	Elastic constant (Young's modulus)
ρ	[kgm^{-3}]	Density
i	[A]	Electrical current
k_{eq}	[N/m]	Mechanical stiffness coefficient
m_{eq}	[kg]	Equivalent mass
b	[-]	Damping
q_{total}	[C]	Total Charge
x	[m]	Displacement
u	[m/s]	Velocity
v_{max}	[m/s]	maximum velocity
F	[Nm]	Force
L	[m]	Length of the device
A	[-]	Unitless value
f, f_0	[Hz]	Resonant frequency
C	[F]	Capacitance
C_0	[F]	Intrinsic Capacitance
L_{m^*}	[H]	Motional Inductance
R_{m^*}	[Ω]	Motional Resistance
Cm^*	[F]	Motional Capacitance
η	[-]	Turn ratio
λ	[m]	Wave length
n	[-]	Mode number
K_c	[m]	Empirical introduced correction factor
f_s	[Hz]	Series resonant frequency in BVD circuit
f_p	[Hz]	Parallel resonant frequency in BVD circuit
k^2_{eff}	[-]	Effective electromechanical coupling factor
Q_f	[-]	Quality factor
T	[K]	Temperature
g_s	[m]	Signal Line gap in Switch
g_a	[µm]	Comb Finger gap in Switch
k_z	[-]	Spring constant in Switch
W_c	[m]	Actuating finger width in Switch
y_a	[-]	Actuation Figure. overlap length in Switch
n_f	[-]	Number of comb fingers in Switch
$\bar{g}$	[m]	Capacitor air gap

List of Acronyms

AlN	Aluminium nitride
BAW	Bulk Acoustic Wave
BVD	Butterworth Van Dyke
CAD	Computer Aided Design
CMOS	Complementary Metal-Oxide-Semiconductor
CMR	Contour-Mode Resonator
FBAR	Film Bulk Acoustic Resonator
FEA	Finite Element Analysis
FEM	Finite Element Modelling
GDS	Geometrical Database Standard
LBAW	Lateral Bulk Acoustic Wave
LN	Lithium Niobate
MEMS	Microelectromechanical System
Mo	Molybdenum
MPW	Multiple Project Wafer
PiezoMEMS	Piezoelectric MEMS
PiezoMUMPs^{TM}	Piezoelectric Multi-User MEMS Processes
PZT	Lead Zirconate Titanate
SAW	Surface Acoustic Wave
SCS	Single Crystal Silicon
SOI	Silicon-on-Insulator
TCF	Temperature Coefficient of Frequency
TED	Thermoelastic Damping
TPoS	Thin-Film Piezoelectric-on-Substrate
ZnO	Zinc Oxide

1. Introduction

Recently, micro-electro-mechanical systems (MEMS) devices have demonstrated immense potential as a viable alternative to traditional solid-state and mechanical components in the field of radio frequency (RF) applications. This is mainly due to their well-established benefits and performance enhancements, such as dimensional downscaling that results in a significant reduction in size [1]. Through the utilisation of silicon and fabrication methods compatible with integrated circuit technology, MEMS mechanical components can be seamlessly fabricated monolithically, paving the way for complete smart system-on-chip solutions [2]. In the domain of MEMS resonators, the piezoelectric transduction mechanism has proven advantageous when compared to its electrostatic counterpart. Capacitive MEMS resonators, fabricated using low acoustic loss materials like single crystal silicon, can achieve frequencies in the GHz-range and demonstrate high quality factors [3,4]. However, capacitive actuation necessitates high drive voltages. On the contrary, piezoelectric MEMS resonators offer a high electromechanical coupling coefficient, allowing them to operate at lower voltages [4]. These resonators operate based on the reciprocal relationship between electrical polarization and mechanical stress in specific piezoelectric materials [5].

There exist two primary types of thin-film piezoelectric micro resonators. The first type employs a thin-film piezoelectric layer as a transducer to either generate or sense acoustic waves in a secondary substrate material like silicon, known as thin-film piezoelectric-on-substrate (TPoS) resonators. These devices can benefit significantly from a carefully chosen substrate material to optimize their specifications [5]. The second type utilizes the piezoelectric film both as the transducer and as the acoustic medium and leverages a sophisticated thickness-mode film bulk acoustic resonator (FBAR) technology [6].

Utilizing the technology of Piezoelectric Multi-User-MEMS Process (PiezoMUMPs) [7] in designing, fabrication, and characterising Lateral Bulk Acoustic Wave PiezoMUMPs resonators (LBAW PiezoMUMPs) and electrostatically-actuated switches is the core work of this dissertation. The Finite Element software program CoventorWare was used for the design and simulation of these devices, while Euro practice was used for the prototype production process.

The radio frequency band that is the focus of this research is the 30-300 MHz (VHF) range. RF-MEMS switches have been designed using a variety of actuation modes, including electromagnetic, electrothermal, piezoelectric, and electrostatic. These switches can be categorised as contact or non-contact depending on their connectivity; contact switches are further divided into metal contacting and capacitive coupling variants [8,9]. Using the technology of PiezoMUMPs, this research work investigates the feasibility of designing and fabricating an electrostatically actuated switches to attain a wide range of frequency tuning by incorporating selector switches with piezoelectrically actuated resonators.

1.1 Motivation

The research work will employ PiezoMUMPs technology to design and fabricate LBAW PiezoMUMPs resonators with several resonant modes. Understanding how resonator design and associated parameters affect resonant frequency and its quality factor will be a part of the research. Post-fabrication fine-tuning approaches, such as thermal ovenisation, voltage, and electrothermal tuning, need to be thoroughly researched and implemented to address process and environmental implications on the resonant frequency. Additionally, an approach to enhancing frequency tunability and cutting production costs across a wide tuning range is achieved via the integration of electrostatic switches with LBAW PiezoMUMPs resonators on a single die.

1.1.1 PiezoMUMPs Resonators

This type of resonators employs aluminium nitride (AlN) as the piezoelectric material resonating in the lateral bulk acoustic mode (LBAW). The PiezoMUMPs MPW process consists of a 0.5 µm layer of AlN above a 10 µm silicon-on-insulator (SOI) layer [6]. The resonators' operation has been explored in the first, third, and fifth lateral resonance LBAW modes, emphasising the importance of energy efficiency (quality factor Q_f) at the resonant frequency in the design of piezoelectric resonators. Comprehensive details regarding the variables influencing the resonator's Q_f value are thoroughly analysed in this thesis. The selection of the 5th resonant mode (60MHz) LBAW Piezo resonator proved to be the most suitable candidate for a fine-tuning study involving the application of thermal and voltage tuning techniques. The experimental outcomes aligned well with the theoretical studies and simulation results, validating the effectiveness of the chosen approach.

1.1.2 Electrostatic Actuated Switches

This study also utilised PiezoMUMPs technology to design and fabricate lateral electrostatically-actuated RF-MEMS switches, enabling the implementation of a switchable array of resonators. This study focuses on mechanical contact switch types that can be integrated with the LBAW resonators using the same PiezoMUMPs methodology. The two-directional actuated switches exhibited no stiction, whereas the unidirectional actuated switches displayed stiction issues and some out-of-plane surface profiles due to post-fabrication effects or sensitivity to humidity. CoventorWare was mainly used to conduct pull-in voltage simulations, achieving low power consumption. The fabrication results validated these findings, with lift-off voltages of 7V and pull-in voltages of 14V being attained. Following fabrication, the performance variations for different contact surface profiles were evaluated.

1.2 Existing Research Problem

MEMS resonators still face challenges such as resonant frequency shifts caused by differences in ambient conditions such as temperature and pressure, as well as tolerances in the fabrication process brought on by variations in geometric dimensions and material properties [10,11]. For this reason, in some high-precision applications, the ability to accurately control the resonator's frequency is essential. Many studies have been conducted on how to adjust the frequency of MEMS resonators, and these are generally divided into three categories: trimming, tuning, and compensating. Every category includes variety of methods and techniques intended to control the frequency of the resonator at device or system level [12,13]. It is interesting to note that LBAW PiezoMUMPs resonators functioning in the VHF region have not yet been combined with thermal and voltage fine-tuning procedures. This points to a possible direction for further research and development in the field of MEMS resonator frequency control techniques.

The design and fabrication of electrostatically actuated switches on the same die as LBAW PiezoMUMPs resonators, which allows for wideband frequency tuning has not been achieved prior to this work.

1.3 Proposed Solution

Precise frequency adjustments can be made via deducing the effects of temperature and voltage tuning methods. The research will investigate the effects of temperature on frequency shifts in ovenised LBAW PiezoMUMPs resonators using theoretical analysis and simulations. Experiments will validate the results. Furthermore, the integration of two heating electrodes using PiezoMUMPs technology on opposite sides of the resonator body allows for the fine-tuning capability to heat the SOI bulk layer electrothermally. Finding out that electrostatically actuated RF MEMS switches can be integrated with the planned LBAW PiezoMUMPs resonators on a single die is one of the main objectives of this work. By increasing its adjustable range inside the VHF band, this integration aims to showcase the features and capabilities of the most recent advancements in RF MEMS resonator technology.

1.4 Thesis Outline

This thesis includes six chapters: in-depth literature analysis on the RF piezoelectric MEMS resonators is covered in Chapter 2. It offers a thorough explanation of the theory and underlying principles of these RF-MEMS resonators, including material characteristics, basic ideas, and fabrication details. In addition, Chapter 2 presents different resonant vibration modes, performance assessment methods, and optimisation techniques. The chapter also looks at the various actuation techniques used, explaining the theoretical underpinnings of switch actuation as well as the working principles of RF MEMS resonators. It provides information on resonant vibration modes, fabrication guidelines, material attributes, performance evaluation procedures, and frequency control methods. Recent PiezoMUMPs resonator design, tuning methods, electrostatic RF MEMS switches, and new developments in the field of study are all covered.

Chapter 3 investigates how PiezoMUMPs technology can be used to create MEMS resonators. It highlights factors like the resonant mode of these resonators in the lateral bulk acoustic wave mode, the modes relevant to resonant frequency of interest, and the possibility of running into manufacturing and design issues. These difficulties may include the size of the design, the number of electrode elements, the geometry of the tether, and how these affect anchor losses. This extensive analysis attempts to clarify how PiezoMUMPs technology can be best applied in the development and manufacturing of MEMS resonators, considering several variables that may affect their efficacy and performance.

A feasibility study using PiezoMUMPs technology to fabricate piezoelectric MEMS lateral bulk acoustic wave resonators is provided in Chapter 4. This chapter combines theoretical research with preliminary simulation results that account for the effect of temperature variations on the resonant frequency. This work demonstrates how these resonators can be tuned and emphasises how high-precision timing circuits such as frequency counters can benefit from their use. The chapter also goes into detail regarding the experimental results that support the effectiveness of voltage and thermal tuning methods on PiezoMUMPs resonators.

Chapter 5 primarily discusses the design and fabrication of electrostatically actuated MEMS switches, specifically the two- and three-state mechanical contact types for microwave band applications. These switches, which are necessary for achieving a broad frequency tuning range via cost-effective frequency switching inside the VHF band, are developed using PiezoMUMPs technology. Based on the concept of a three-state non-contact switch, the design has three operating states: ON, OFF, and deep-OFF. The objective is to evaluate the feasibility PiezoMUMPs technology to incorporate an electrostatically-actuated switch in the same die with resonators, and thereby drive new developments in MEMS technology. Several switches are manufactured, and the 3D models for them are realised using CoventorWare software, which builds upon the foundation of a previous design [8].

Chapter 6 presents the conclusions and future work of this dissertation, where the achieved results are summarised including a comparison between different fine-tuning techniques. Also, summarised results of wide-band tuning using the electrostatically actuated switches design and fabrication are presented briefly including their characterization outcomes.

2. Literature Review on RF MEMS Devices

This chapter presents a literature review on radio frequency (RF) micro-electro mechanical system (MEMS) resonators and switches with particular emphasis on their underlying principle of operation and actuation mechanisms. State-of-the-art Piezoelectric MEMS resonators and their frequency tuning mechanisms and resonant modes of vibration are covered, as well as electrostatic RF MEMS switches, while highlighting the latest research advances and performance measurement methods. This chapter also discusses the material properties, the fabrication concepts and the design rules employed in implementing these devices. This literature review aims to identify research gaps such as the integration of RF MEMS switches with lateral bulk acoustic PiezoMUMPs resonators on the same die to achieve a wider tuning range in the very-high frequency (VHF) band from 30 MHz to 300 MHz.

2.1 RF MEMS Actuation Mechanisms

In RF MEMS devices, the input electrical energy is converted into mechanical motion by means of an actuation mechanism. The most common actuation mechanisms used in RF MEMS devices are summarised below [14, 15, 16, 17]:

Electrostatic actuation is based on the principle of electric charges that create attractive or repulsive forces between conductive elements, which can be used to move or control microscale mechanical components [14, 18, 19]. Electrostatic actuators are quite widespread due to their fast response and low power consumption [14].

Electrothermal actuation is based on the principle of thermal expansion and temperature variation. It provides a large driving force but a small displacement under a low driving voltage with a slow response [14, 20, 21, 22, 23].

Electromagnetic actuation utilizes the interaction between a magnetic field and an electric current to induce mechanical movement. This type of actuation provides a fast response and a large displacement. However, this type of actuation requires large die area [14, 15, 25].

Piezoelectric actuation is based on piezoelectric materials and their ability to convert electrical energy into mechanical energy and visa-versa. Piezoelectric materials can vibrate at different frequencies depending on the mode of vibration and the driving voltage [14, 25, 26].

The following sections will present a comprehensive understanding of electrostatic and piezoelectric actuation methods, since this research work was mainly based on these two forms of actuation.

2.1.1 Electrostatic Actuation

The main principle of electrostatic actuation relies on the electric field of a parallel plate capacitor, which is generated by a voltage applied across two parallel plates with opposite charges accumulating on each plate [14, 27]. Electrostatic actuation uses the attractive electrostatic force between the two oppositely charged electrodes to move a membrane, which is usually one of the two electrodes. Coulomb's law describes the force between two charges separated by a given distance, which is generated between fixed and moveable plates in electrostatic actuation. Electrostatic actuation mechanisms have a simple design, a fast response time, are easy to fabricate, and consume little power. On the other hand, the associated non-linearities and the required high actuation voltage $\boldsymbol{v}$, are the main drawbacks of this type of actuator [14, 28,29].

The most common electrostatic actuation designs are based on either a parallel plate capacitor structure, with a movable and a fixed plate as shown in Figure. 2.1 [14,30] or comb-drive structures made up of several interdigitated or non-interdigitated fingers as presented in Figure. 2.2 [14, 28-32].

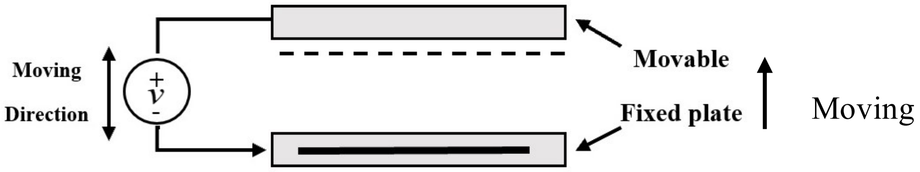

Figure. 2. 1: Parallel plate capacitor structure used in electrostatic actuation [14, 32].

Comb-drive actuators are generally preferred since they provide a large displacement (a few tens of micrometres are possible), and the force is not proportional to the displacement [14]. Electrostatic actuation is employed in a broad range of micromechanical actuator applications, including RF MEMS switch applications [14, 33, 34].

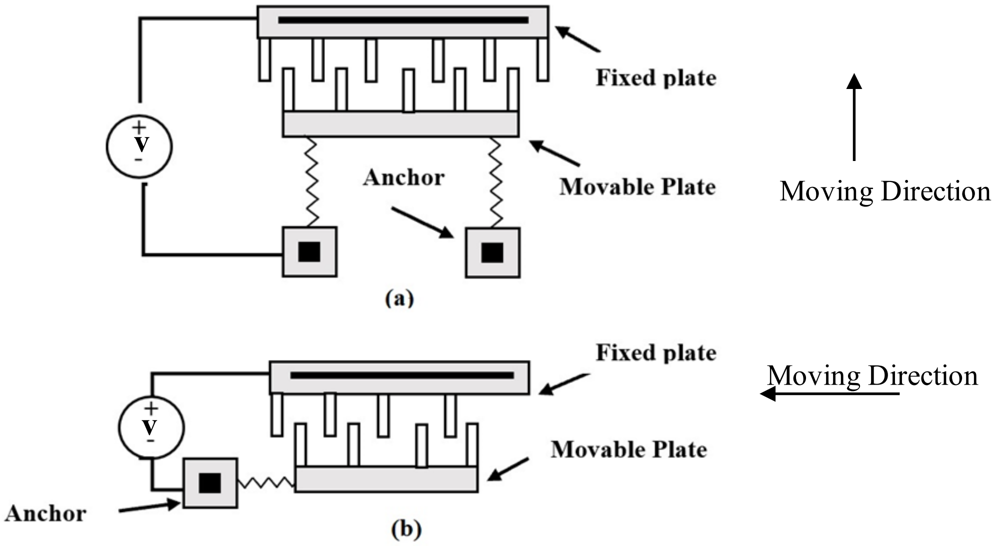

Figure. 2. 2: Electrostatic comb-drive configurations: (a) Longitudinal comb actuator; (b) Transverse actuator [14, 28-32].

2.1.2 Piezoelectric Actuation

Piezoelectric materials are electrical insulators that are sandwiched between two conductive electrodes to respond to an electric field via an interdigitated electrode or a sandwich structure [14]. The basic principle of piezoelectric actuation in MEMS devices is to use a thin piezoelectric layer deposited as part of the MEMS beam between flexible electrodes. When a voltage is applied to the piezoelectric layer, the piezoelectric material expands or contracts due to the polarization of the applied voltage, which causes an axial bending across the length of the flexible beam as shown in Figure. 2.3 [14, 33,34, 35].

In general, piezoelectric actuators provide several benefits, including a high output force, a wide operating bandwidth, small size, light weight, low power consumption and short reaction time [14, 35, 36].

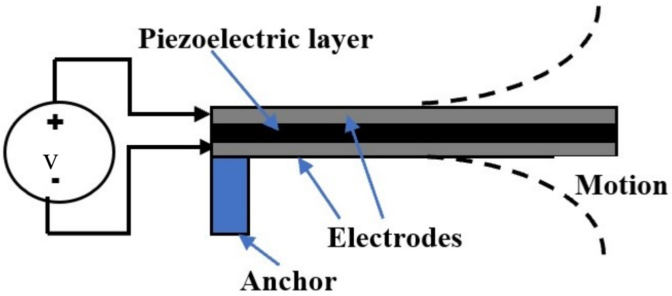

Figure. 2. 3: Schematic diagram of the piezoelectric actuator [14, 35].

Unfortunately piezoelectric actuators typically provide small displacements and feature a high temperature sensitivity [14, 28]. Piezoelectric actuators are used in a large variety of applications but are limited by their non-linear operation and associated hysteresis [14]. Additionally, the materials used in piezoelectric devices are extremely fragile and are rarely used on their own. Piezoelectric materials are frequently used in conjunction with a flexible structure for actuation and sensing applications. Several works based on the piezoelectric actuation [14, 25, 35, 36,37,38] have studied the possibility of using a piezoresistive microcantilever for environmental applications, especially in humidity sensing using Thin-Film Piezoelectric-On-Silicon (TPoS) resonators [14, 38].

2.2 Piezoelectricity and Piezoelectric Principles

The piezoelectric effect describes a material's ability to generate an electrical voltage in response to applied mechanical stress. The Curie brothers discovered piezoelectricity in 1880, and the word 'piezo' comes from a Greek word that means 'press' or 'push.' A piezoelectric actuator is a type of transducer that uses piezoelectric effect to turn an applied potential into a mechanical movement or strain. [14, 28].

To understand piezoelectric actuation in detail, it is first necessary to outline the basic piezoelectric concepts, including piezoelectric material’s properties, which will be discussed in the following sections.

2.2.1 Piezoelectricity in Concept

Piezoelectricity in a material is a coupled electrical and mechanical phenomenon and the electrical behaviour of its material can be described by [39].

$$D = \varepsilon E_f \tag{2.1}$$

D is the electrical displacement, ε is the permittivity of the material, and E_f is the electrical field strength. Likewise, to express the mechanical behaviour of materials, Hooke's law states:

$$S = sT \tag{2.2}$$

S is the strain, s is the compliance, and T is the stress. Piezoelectric materials combine the above two equations into one coupled field described by the electro-mechanical set:

$$D = \varepsilon_r E_f + dT$$

$$S = d^t E_f + s^{Ef} T \tag{2.3}$$

Where, d= piezoelectric coefficient, E_f = electric field strength, d^t the piezoelectric coefficient matrix, ε_r = relative permittivity, s^{Ef} = compliance matrix [39].

The two most important parameters which contribute to the piezoelectric material's performance are:

Piezoelectric Coefficient (strain factor) (*d*):

This factor refers to the coupling relationship between the piezoelectric elastic effect and the electric polarization effect. When the value of d is higher, that represents a stronger coupling effect. The three functioning modes of the piezoelectric effect are d_{31}, d_{33}, and d_{15}, Normal stress is experienced by d_{31} and d_{33}, while shear stress is experienced by d_{15}, Figure. 2.4 Shows a simplified layout of both d_{31} and d_{33} modes [40].

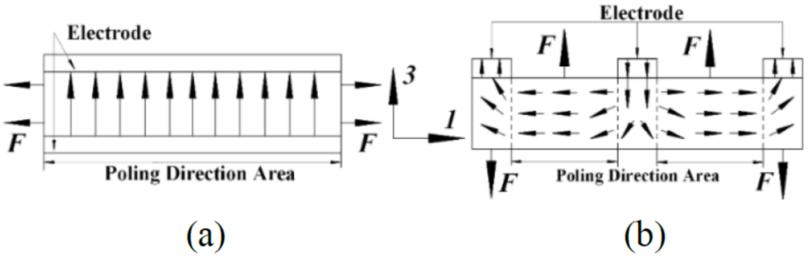

Figure. 2. 4: A simplified layout of piezoelectric modes,
(a) d_{31} mode, (b) d_{33} mode [40].

In parallel plate electrodes in d_{31} mode, the direction of polarization is perpendicular to the direction of applied stress: research on d_{31} mode has shown this design to be relatively simple to fabricate [40].

Relative Permittivity (dielectric constant) (ε_r):

Commonly known as the relative permittivity, this coefficient indicates how quickly a material be polarized by applying an electrical field to an insulator. The ratio of " the permittivity of substance to the permittivity of space or vacuum" is known as relative permittivity. For a piezoelectric ceramic material ε_r is the dielectric displacement per unit electric field. High frequency of piezoelectric ceramics requires low ε_r constant [40].

2.2.2 Piezoelectric Materials

The discovery of a large number of piezoelectric materials has offered a surge in MEMS devices that use the piezoelectric effect as their primary mechanism of actuation, resulting in a wide range of applications in science and technology [41].

There are various natural and manufactured materials with piezoelectric properties, which can be divided into two groups: piezoelectric ceramics and piezoelectric crystals. The piezoelectric effect occurs naturally in monocrystalline materials like quartz. Because of its material features such as low dielectric loss, thermal stability, and high mechanical strength, quartz crystals are in high demand for MEMS applications [41]. However, the challenges of downsizing, as well as its relatively moderate piezoelectric effect compared to piezoelectric ceramics, have prevented it from being wildly utilized in MEMS technology. Due to the ease with which this technology can be integrated with current semiconductor microfabrication technologies, piezoelectric ceramics have become the optimum choice for MEMS piezoelectric devices. Additionally, the electrical and mechanical properties of piezoelectric ceramics are comparable to or superior to those of quartz crystals. Thin films of piezoelectric materials such as lead-zirconate-titanate (PZT), lithium niobite ($LiNbO_3$), aluminium nitride (AlN), and zinc oxide (ZnO) have become the most common piezoelectric ceramics in recent years [41].

AlN became widely used in RF applications due to its material properties. Its advantages included stability during the deposition process, the low-temperature sputtering deposition process of thin-film AlN enables stacking of multiple AlN and electrode layers which can be properly configured to efficiently transduce the desired mode of vibration of the structure and simultaneously achieve the optimum input and output impedance values. For these reasons AlN has been often considered as a preferred material for the fabrication of purely piezoelectric laterally vibrating resonators with low thermal drift, good power handling, and chemical compatibility with semiconductor technology [42]. Lithium Niobite, Zinc Oxide and Lead Zirconate Titanate, contain metals with high diffusivity, so they cannot tolerate microfabrication facilities as AlN can do: in addition, AlN is considered environmentally friendly, since it is a lead-free material [42]. Table.2.1 Shows a comparison of commonly used piezoelectric materials along with their performance parameters values [40,43].

Table.2. 1: Commonly used piezoelectric materials along with their performance parameters [40, 43].

Piezo Material	Symbol	Unit	LiNbO3	ZnO	PZT	AlN	Ref No
Piezoelectric coefficient 'strain factor'	d_{31}	pC/N	-7.4	-4.7	-130	-1.8	[41]
Relative permittivity	ε_r	F.m	44	9-11	400-1900	8-10	[41]
Piezoelectric Constant	e_{33}	C/m^2	0.23	-0.57	-6.5	-0.58	[43]
Elastic Modulus	E	GPa	203	201	68	308	[43]
Density	ρ	kgm^{-3}	4640	5676	7600	3260	[43]

The piezoelectric characteristics of AlN, ZnO, PZT, and LiNbO3 are shown in Table.2.1. The piezoelectric materials chosen are determined based on application. Although PZT thin films have the highest piezoelectric coefficients, deposition of PZT thin films typically necessitates processing at temperatures above 600 °C, which is incompatible with several microfabrication procedures. Furthermore, due to the toxicity of PZT ceramic, which contains dangerous lead compounds, AlN and ZnO have emerged as piezoelectric materials for bio-applications in recent years [43].

2.3 Resonator Mechanical-Electrical Modelling

RF MEMS resonators' main concept is based on their transduction mechanisms, which are divided into two types: capacitive (electrostatic) and piezoelectric. The piezoelectric RF MEMS resonators have lately become widely marketed due to their distinct advantages [3, 44, 45] over the capacitive micro resonators which need to operate in vacuum to reach frequencies in the GHz-range, have a high-quality factor, and are fabricated on a low acoustic loss material, such as single crystal silicon [3, 4]. In RF applications, TPoS devices have managed to produce excellent oscillator performances by use of MEMS resonators with both high quality factor (Q_f) and low motional resistance [5,6,46]. Low-motional resistance at very high frequencies is a feature of devices made with Film Bulk Acoustic Resonator (FBAR) technology, making them a viable choice for filtering applications [6,47]. The resonant system performance is determined by both electrical and mechanical energy mechanisms, which operate at a resonance frequency, through coupling (forward and backward) between stress and the electric field in a piezoelectric material, as shown in Figure. 2.5 [42].

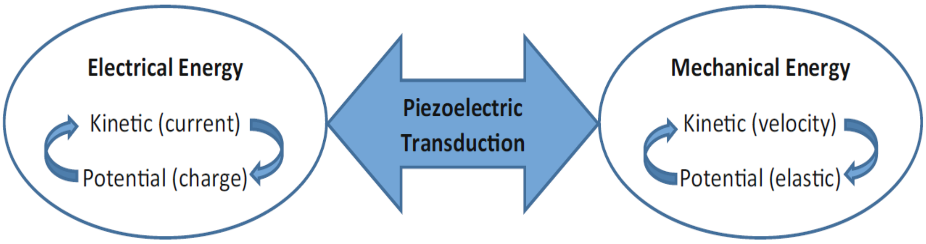

Figure. 2. 5: The energy flow mechanism in the piezoelectric resonator [42].

Fundamentally, every mechanical resonator can be approximated by an equivalent lumped mass-spring-damper system, as it is shown in Figure. 2.6 [48]. The mass is linked to a fixed support using a spring. All the three components share the same displacement and therefore in the electrical model, they are represented by components connected in series [48].

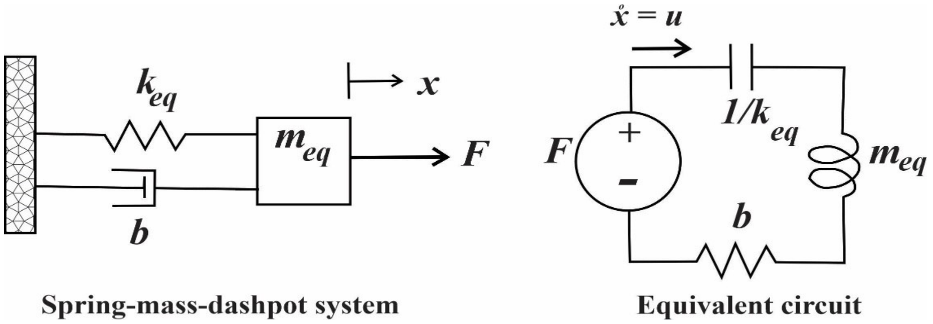

Figure. 2. 6: Modelling from mechanical to electrical representations [48].

The equivalent circuit, can be modelled using any of formal dynamical methods (such as state variables and state equations) Therefore, a mechanical resonator can be represented by a simple RLC circuit as was shown in Figure. 2.6 [48].

The differential equation controlling the motion in the equivalent mechanical model of Figure. 2.6 is displayed as [48]:

$$m_{eq}\frac{\partial^2 x}{\partial t^2}+b\frac{\partial x}{\partial t}+K_{eq}x=f(t) \tag{2.4}$$

This equation is comparable to the equation derived for an RLC electrical circuit

$$L\frac{\partial i}{\partial t}+Ri+\frac{1}{C}\int idt=v(t) \tag{2.5}$$

However, in electromechanical resonators, the effect of the transduction mechanism should also be included in the model. Furthermore, a feedthrough capacitance should be added in parallel with the RLC path to account for a portion of the electrical signal that is not converted to acoustic energy and passes through a parasitic capacitance from the input directly to the output or to ground [46].

In general, for any resonator whose material is isotropic, the natural resonant frequency can be calculated using the following formula [39]:

$$f=\frac{A}{L}\sqrt{\frac{E}{\rho}}=\frac{1}{2\pi}\sqrt{\frac{k_{eq}}{m_{eq}}} \tag{2.6}$$

where *A* is a unitless value, *L* is the device (cantilever) dimension having the units of length, *E* is the Young's modulus, and ρ is the density of the material. The damping coefficient (*b*) is a measure of energy loss in the system and is related to the quality factor Q of the resonator [39]:

$$b=\frac{2\pi f m_{eq}}{Q} \tag{2.7}$$

The corresponding circuit for a piezoelectric transducer is a simplified form of the Mason's model as shown in Figure. 2.7. This model is used in one port resonators, to analyse their basic characteristics [39].

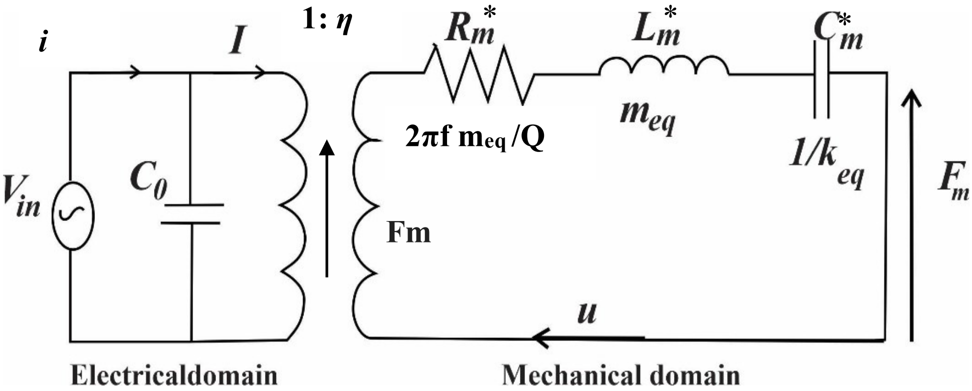

Figure. 2. 7: The Typical Mason lumped circuit model for a piezoelectric transducer (one port) [39].

From Figure. 2.7, the piezoelectric transducer has been modelled by researchers [39]:

An intrinsic capacitance, C_0, to represent the physical capacitance of the electrode part of the piezoelectric device [39]. C_m* it is the real value before the transformation.

A transformer, has a turn ratio (η), to represent the electrical to mechanical convergence at a specified position of the device (maximum displacement point).

Capacitance C_m^*, resistance R_m*, and inductance L_m*, these motional electrical variables are representing the mechanical properties of the MEMS resonators referring to the primary side of the transformer, and they are linked to the compliance ($\frac{1}{k_{eq}}$), damping (b) and mass (m_{eq}), respectively.

Thus:

$$C_0 = \varepsilon_P \frac{\text{Electrode Area}}{\text{Thickness of Electrode Area}}$$

$$\eta = \frac{F}{V} = \frac{I}{u}$$

$$C_m{}^* = \frac{1}{k_{eq}}, \qquad R_m{}^* = b, \qquad L_m{}^* = m_{eq} \tag{2.8}$$

Where ε_P, is the permittivity of the piezoelectric material, and F is the applied force, V is the electrical voltage, I *is* the electrical current, and u is the velocity, and the rest of the variables are described in Table.2. 2 [39].

Table.2. 2: Mechanical and electrical variable translation Table [39].

Mechanical Variables	Electrical Analogue
Force (F)	Voltage (V)
Velocity (u)	Current(I)
Compliance ($1/K_{eq}$)	Capacitance (C_m)
Damping (b)	Resistance (R_m)
Mass (m_{eq})	Inductance (L_m)

2.3.1 One-Port Piezoelectric Resonator Electrical Model

A one-port piezoelectric device has a single pair of input/output connections to the device and in the structure, the static capacitance of the device is in parallel with the motional components of the resonator. In designing the piezoelectric resonators, care must be taken in patterning the electrodes since it will affect the motional impedance of the device, its coupling coefficients (k_t^2), and the excitation of its mechanical modes, as it is shown in Figure. 2.8 [39].

In this configuration the illustrated static capacitance (C_0) between the two metal electrodes is in parallel with the motional resistance branch in the electrical model. The piezoelectric transduction is represented by a transformer with turns ratio of 1: η.

The electromechanical coupling coefficient is η, and is defined as the ratio of the current (i) passing through the resonator to the maximum velocity (v_{max}), or alternatively the ratio of total charge stored (q_{total}) on an electrode to maximum displacement (u_{max}), that gives the following formula:

$$\eta = \frac{q_{total}}{u_{max}} = \frac{i}{v_{max}} \tag{2.9}$$

It should be noted that there is always some parasitic capacitance found between the two connections to the device and this is included in the parallel capacitance of C_0.

The resonator model of Figure. 2.7 can further be simplified to the model known as Butterworth Van Dyke (BVD) as shown in Figure. 2.8 [39,50,51,52].

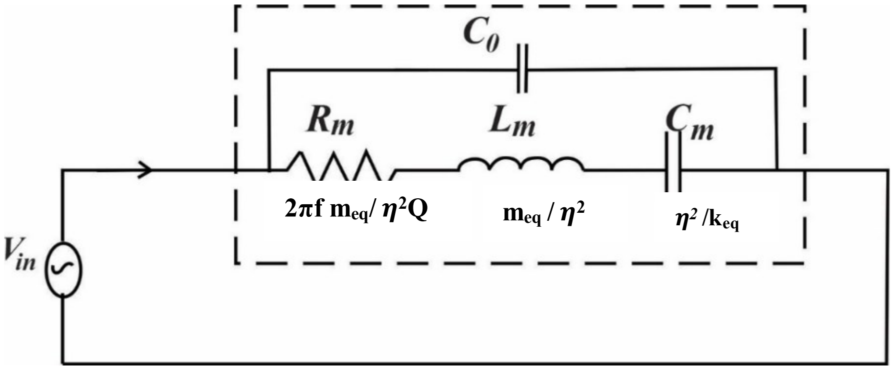

Figure. 2. 8: The BVD electrical representation for a one-port piezoelectric resonator referred to the primary side of the transformer [39,50,51,52].

2.3.2 Two-Port Piezoelectric Resonator Electrical Model

Two-port devices have two pairs of connections as shown in Figure. 2.9, whereas the voltage signal applied to the input port is converted to vibration in the structure while the output port converts the vibration back to an electrical signal [39].

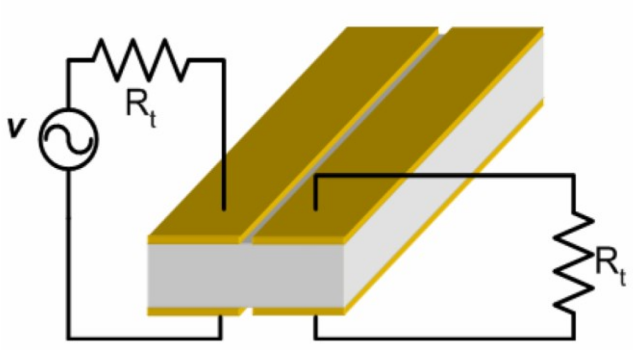

Figure. 2. 9: The schematic viewgraph of a two-port piezoelectric resonator [39].

The equivalent electrical model of the resonator should contain the transduction components for both input and output ports, is shown in Figure. 2.10 [39, 50, 54].

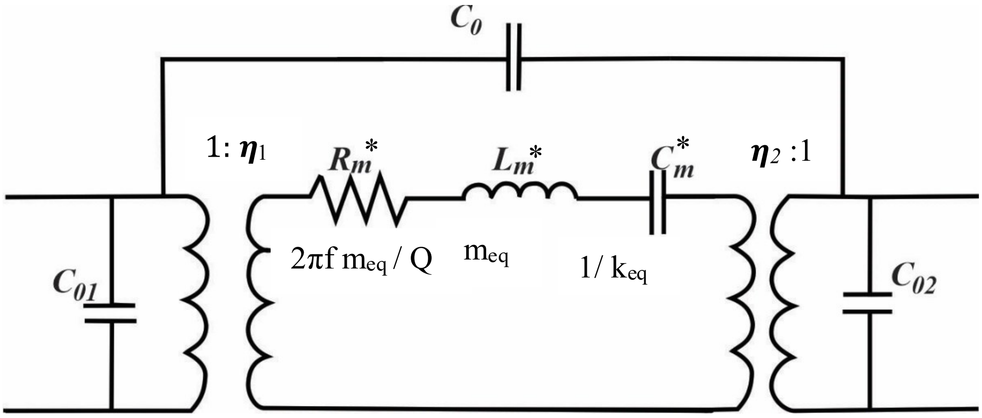

Figure. 2. 10: The electrical model of the two-port piezoelectric resonator [39,50, 54].

C_0 is the parasitic feedthrough capacitance between the input and output electrodes. Both input and output coupling coefficients (η_1, η_2) as well as the static shunt capacitors (C_{02}, C_{01}) can have different values [39].

2.4 Acoustic Wave and Vibration Modes at Resonance

MEMS resonators can resonate at different modes and the shape of its vibration depends on its design and the technology used [49]. Both surface-acoustic-wave (SAW) and bulk-acoustic-wave (BAW) components use acoustic waves to operate, but the two acoustic component types and technologies are fundamentally different. Oscillators, filters, and delay lines are among the resonant-type components that can be supported by both technologies. In comparison to their BAW counterparts, SAW components have a lower frequency [51]. Both technologies, however, provide functional circuits within their frequency ranges and have compact sizes, making them appealing for a wide range of commercial, industrial, and military applications [51]. The electromechanical properties of some materials, particularly an isotropic piezoelectric material, are used in both SAW and BAW components. Piezoelectric materials can transfer mechanical stress into electrical energy and vice versa [51]. A brief review about SAW and BAW resonant acoustic waves and vibration modes is presented in the following sections.

2.4.1 Surface Acoustic Wave (SAW)

Early MEMS techniques were successfully employed to design acoustic resonators with gradual increases in resonance frequency achieved [49]. These included surface-wave and bulk-wave resonators. A surface acoustic wave (SAW) occurs when the piezoelectric layer, and acoustic waves move together on the surface resonator's material as shown in Figure. 2.11. The acoustic wave energy moves along the surface layer of the resonator, between sets of interdigitated electrodes, [49] and creates a surface propagation wave at resonant frequencies.

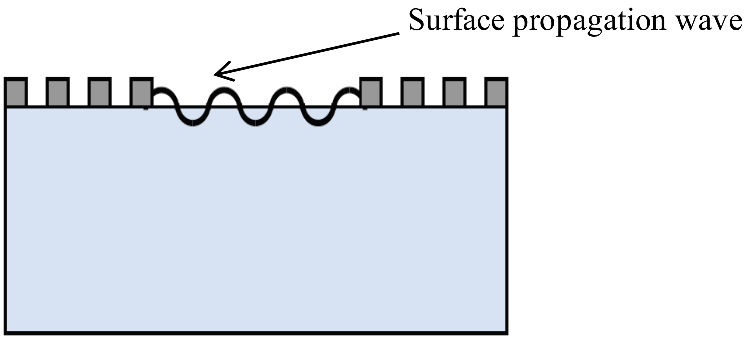

Figure. 2. 11: Acoustic wave energy travels along the surface of the surface layer of the resonator [49].

2.4.2 Flexural Mode

These modes of vibrations are characterised by a bending of the structure along its length (L), such that motion is in the transverse direction and perpendicular to the length. Both beam and plate structures can be excited in flexural modes. The movement of the beam structure, can be identified either by its width (w) or its thickness (t). Equation 2.10 implies the beam is made of a single material, with E denoting Young's modulus and ρ denoting density and β is a dimensionless coefficient that depends on the respective boundary conditions applied to the structure and is determined by the form of the vibration mode [5].

$$f_{flexural} = \beta \left(\frac{t}{L^2}\right) \sqrt{\frac{E}{\rho}} \tag{2.10}$$

These flexural modes can be classified into three types: clamped-end, clamped –clamped and free – free [5], as shown in Figure. 2. 12.

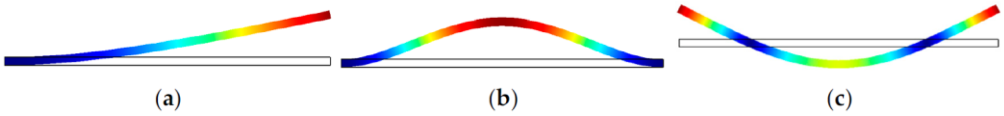

Figure. 2. 12: General types of flexural modes according to their boundary conditions: clamped end, (b) clamped –clamped, (c) free – free [5].

2.4.3 Torsional Mode

Paddle resonators, which consist of a plate supported on two opposite ends by beams, are the most common type of torsional mode resonator. As shown in Figure.2.13, the paddle resonator oscillates by rotating along the axis along which the supporting beams lie. Since the plate oscillates around the axis of rotation, the supporting beams are clamped at their ends and twist [5, 56].

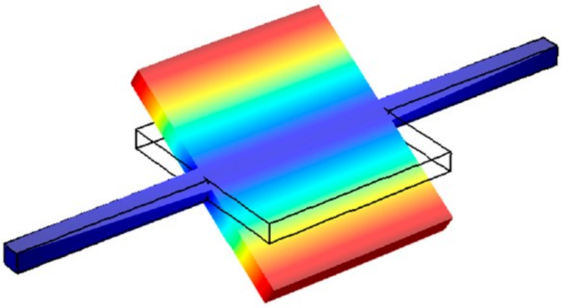

Figure. 2. 13: Torsional mode in paddle resonator: colours represent the out of plane displacement (red means high dissplasment) [5].

To summarise, in TPoS resonators the electric field is orthogonal to the substrate plane. The resonance mode is called a thickness mode when the acoustic wave propagation direction is parallel to the electric field, and the resonance frequency is mainly determined by the structure thickness. If the elastic-wave motion is transverse to the electric field, a lateral mode is excited, and the resonance frequency is largely determined by the resonant structure's in-plane dimensions.

2.4.4. Bulk Acoustic Wave (BAW)

BAW resonators are produced when a thin film of piezoelectric material is deformed in response to a transverse electric field, resulting in acoustic waves standing within the bulk material, rather than along its surface. Figure. 2.14 shows how the acoustic energy travels in the bulk material, and how it propagates through the thickness of the piezoelectric layer in the resonators [49].

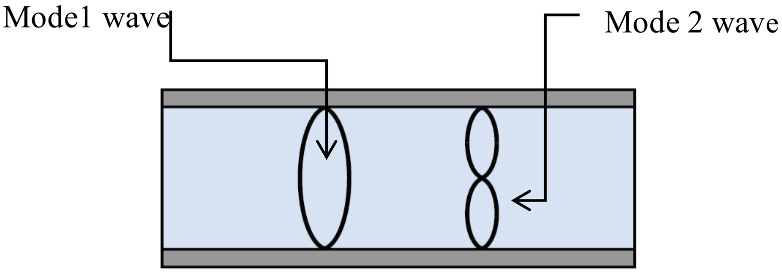

Figure. 2. 14: The acoustic wave standing through the thickness of the resonator's piezoelectric layer [49].

Bulk mode resonators change the structure by planar expansions or contractions rather than bending. The resonant frequencies of bulk modes are only geometrically dependent on the structure's lateral physical dimensions (e.g., width or length), this means that the vibration mode is determined only by the structure's lateral properties (L) in the case of lateral movement, B represent number of modes and other factors, ρ is the material density [5].

$$f_{bulk} = \frac{\beta}{2L}\sqrt{\frac{E_{bulk}}{\rho}} \tag{2.11}$$

Where E_{bulk} is the effective Young's modulus of the plate structure defined for a given axis of motion [5], bulk mode can be excited as:

Lateral (width / length): This mode of vibration is considered much stiffer than flexural mode resonators, that explains why bulk mode resonators with similar dimensions as flexural ones have higher resonant frequencies. Contour mode resonators (CMR) are lateral bulk modes of resonance that are applied to piezoelectric resonators in which the acoustic radiation patterns are perceived as contours in the manufacturing plane [44]. The CMR device employs a thickness extensional contour mode, in which the resonant frequency is determined by the width of the structure rather than the thickness [5]. PiezoMEMS resonators are designed using a thin piezoelectric film and resonate in what is called the lateral mode, known as Lateral Bulk Acoustic Wave PiezoMEMS (LBAW PiezoMEMS). In this design, the nodal points of the main length extensional resonance mode are fixed at the film's midpoint. When an electric field is applied through the thickness, it excites a strain field in the lateral direction: $S_1 = d_{31}E_3$. This kind of piezoelectric resonator has a resonant frequency f, which can be deduced using the in-plane geometry. An approximate value for the resonant frequency f for a rectangular mechanical resonator with isotropic elastic properties can be found using [3]:

$$f = \frac{n}{2L}K_c\sqrt{\frac{E_{eff}}{\rho_{eff}}} = \frac{1}{2\pi}\sqrt{\frac{k_{eff}}{m_{eff}}} \tag{2.12}$$

Where n refers to the mode number, L is the resonator's length, E_{eff} and ρ_{eff} refer to the equivalent unidirectional elastic modulus and density of the resonator stack respectively. The coefficient K_c is an empirically introduced correction factor. The parameters k_{eff} and m_{eff} are the effective stiffness and mass respectively of the mechanical vibrating system.

Thickness mode: A vibration across the thickness of the film of the piezoelectric plates (circular or rectangular), is the main mode of vibration for the AlN FBAR [56, 57].

TPoS resonators is orthogonal to the substrate plane, when the acoustic wave propagation direction is in parallel with the electric field, the resonance mode is called a thickness mode and the resonance frequency is defined mainly by the thickness of the structure [33, 41]. In Figure. 2.15, different bulk mode shapes in resonators are illustrated: (a) length-extensional (LE) (b) width-extensional (WE) modes in rectangular plates, (c) square-extensional (SE) mode in square plates, (d) radial breathing mode in circular disks [5].

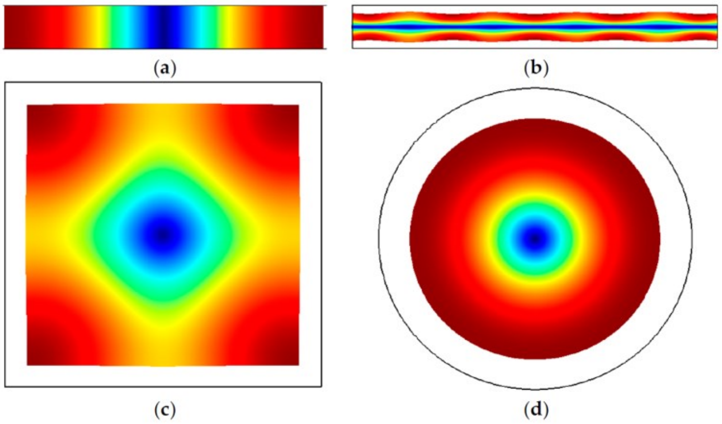

Figure. 2. 15: Different bulk mode shapes in different resonators;
(a) length-extensional (LE), (b) width-extensional (WE) modes in rectangular plates,
(c) square-extensional (SE) mode in square plates, (d) radial breathing mode
in circular disks [5].

2.4.5 Shear Mode

Shear mode resonators, like bulk mode resonators, have an acoustic wavelength that is defined solely by the structure's lateral characteristics. However, shear modes are defined by shear waves rather than longitudinal waves, as opposed to bulk modes. The Lamé mode [5, 55] and Face shear (FS) mode [5, 58] have been observed in square plates, and the Wine glass mode in circular disk [51, 59]. These are all shown in Figure. 2.16 (a), (b), (c) respectively.

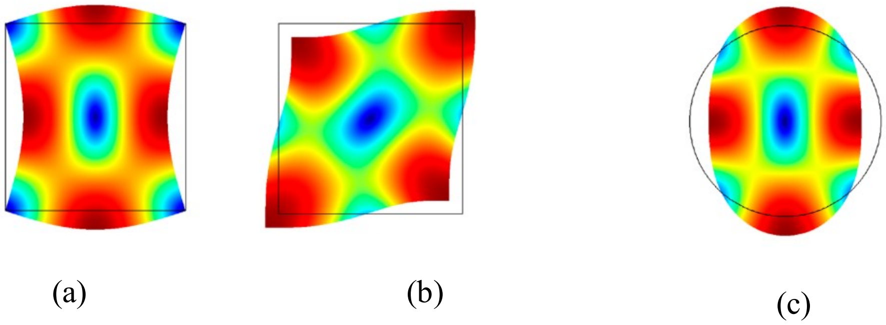

Figure. 2. 16: Lateral shear mode; (a) Lame, (b) Face shear, (c) Wine glass mode [5,55,58,59].

This research focuses on lateral mode resonators, because the lateral dimension of the resonator is defined lithographically. The piezoelectric materials employed in TPoS resonators are sputtered polycrystalline materials that are typically transversely isotropic. An example of one port TPoS resonators was presented in a recent research paper [39].

The resonant structure is disengaged from the remainder of the substrate and is supported by anchors positioned around the resonator edge, and the piezoelectric layer is sandwiched between two metallic electrodes layered on top of a comparatively thick (>2 µm) layer of low acoustic-loss material (such as single crystal silicon) as shown in Figure. 2.17 [39].

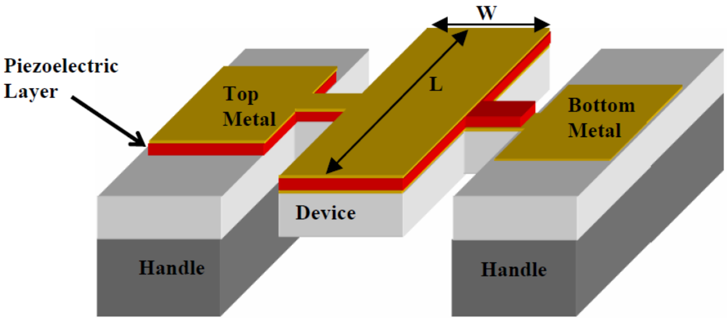

Figure. 2. 17: A one-port TPoS resonant structure [39].

2.5 Piezo MEMS Resonators Performance Measures

Through the two-way connection between stress and electric field in a piezoelectric material, a piezoelectric-based resonator is an electromechanical device in which electrical and mechanical energies are reciprocally transformed to each other at a resonance frequency [42]. Furthermore, at every vibration half cycle, the mechanical energy in the resonator body and the applied electrical energy through the metallic electrodes transfer from potential to kinetic and back as shown in Figure. 2.5. As a result, both energy convergence methods outlined above determine the overall performance of a resonant system [42]. There are two specific parameters specified as electromechanical coupling factor (k_t^2) and quality factor to quantify the efficiency of these energy transformations in a resonator (Q_f) [42], both are discussed in details in the following section.

2.5.1 The Quality Factor (Q_f)

During electrical and mechanical energy convergence, part of this energy contained in the resonator will either be directly dissipated to the surrounding structure, or it will turn into a form of heat. The Q_f is used to measure this kind of loss in a resonator, which is generally defined as [42]:

$$Q_f = 2\pi \frac{\text{peak energy stored}}{\text{energy dissipated per cycle}} \tag{2.13}$$

In a piezoelectric resonator, there are three different sources of loss: electrical, electromechanical, and mechanical/elastic losses which are described briefly below [57, 60, 61]:

Electrical Losses: This loss includes the resistive losses, which represents the conductive resistance of electrodes and dielectric materials.

Electromechanical (i.e., piezoelectric losses): This loss happens when there is non-ideal mutual convergence of electrical and mechanical energies.

Mechanical / Elastic Losses: This type of loss occurs during mechanical energy convergence into heat, or when there is a leakage of mechanical energy from the system.

These loss mechanisms are categorized into intrinsic and extrinsic types, as presented in Table.2. 3 [42].

Table.2. 3: Two main groups of sources of loss [42].

Intrinsic loss	Extrinsic loss
Dielectric loss	Anchor
Piezoelectric loss	Air fluidic
Phonon- phonon interaction	Surface
Phonon- electron interaction	Ohmic

2.5.1.1 Quality Factor in Piezoelectric Resonators

The total quality factor Q can be determined from the individual quality factor components by [39]:

$$Q_f = \left(\frac{1}{Q_{material}} + \frac{1}{Q_{anchor}} + \frac{1}{Q_{air}}\right)^{-1} \tag{2.14}$$

where $(\frac{1}{Q_{material}})$, $(\frac{1}{Q_{anchor}})$, and $(\frac{1}{Q_{air}})$ are terms related tomaterial damping, anchor loss and air damping respectively. The loss component due to air damping $(\frac{1}{Q_{air}})$ can be prevented by operating the resonator in vacuum [39]. In comparison to capacitively-transduced resonators, piezoelectric resonators are less vulnerable to air damping because the required narrow capacitive gap is not present in piezoelectric resonators. Anchor loss is caused by the resonant body radiating acoustic energy through the anchors that hold the resonator in place. These anchors can take many various forms depending on the resonator's design, but they all contribute to the resonator's final quality factor in the same way. The acoustic waves do not remain totally contained within the resonator, but rather radiate through the anchors and leak into the substrate [39]. Because the acoustic energy delivered by these waves is not conserved in the resonator, it is considered lost. Various design techniques have been considered to reduce anchor loss [39, 62].

2.5.2 The Piezoelectric Coupling Factor

Various methodologies are used to understand the resonator's electromechanical coupling factor as outlined below. In order to compare different piezoelectric material's efficiency, particularly in electrical to mechanical energy convergence or vice versa, the unitless piezoelectric coupling factor (k_t^2) can be used. One way to determine this factor is by considering a loss-free scenario as [36]:

$$k_t^2 = \frac{W_M}{W_M + W_E} \tag{2.15}$$

- W_M is the delivered energy to a mechanical load by a piezoelectric actuator.
- $(W_M + W_E)$ is the preloaded potential energy by connecting to an electrical source [63].

This ratio can also be represented as a function of material properties, under the 1D scenario's condition (the stress is only a non-zero in one direction) [36]:

$$k_t^2 = \frac{e^2}{E\ \varepsilon_r} \tag{2.16}$$

Where

e is the piezoelectric constant directed in the same path as that of the electric field and mechanical stress.

E is the elastic constant with zero electric field.

ε_r is the dielectric constant, in the same direction as the electric field at zero stress.

The maximum piezoelectric coupling factor achieved for the most used piezoelectric materials in resonator fabrication are listed in Table.2. 4 [39,64, 65].

Table.2. 4: The maximum piezoelectric coupling factor, for the most commonly used piezoelectric materials in resonator fabrication [39,64, 65].

Material	**Quartz**	**AlN**	**ZnO**	**PZT**	**$LiNbO_3$**
k_t^2 (%)	0.86	6.5	8.5	23	23

2.5.2.1 The Effective Electromechanical Coupling Factor

In piezoelectric resonators, their energy convergence efficiency at resonant frequency is one of the most important factors that designers focus on. This effective electromechanical coupling factor can be defined by measuring the resonant frequencies (f_s and f_p), when the impedance of the BVD circuit Figure. 2.8 (shown earlier in section) is at minimum and maximum magnitude respectively. The graph of impedance with frequency is presented in Figure. 2.18 [39], and the following equations can be extracted.

$$f_s = \frac{1}{2\pi\sqrt{L_m C_m}} \tag{2.17}$$

$$f_p = f_s \sqrt{\frac{C_0 + C_m}{C_0}} \tag{2.18}$$

$$Q_f = \frac{1}{R_m}\sqrt{{L_m}/{C_m}} \tag{2.19}$$

$$k_{eff}^2 = \frac{f_p^2 - f_s^2}{f_p^2} \tag{2.20}$$

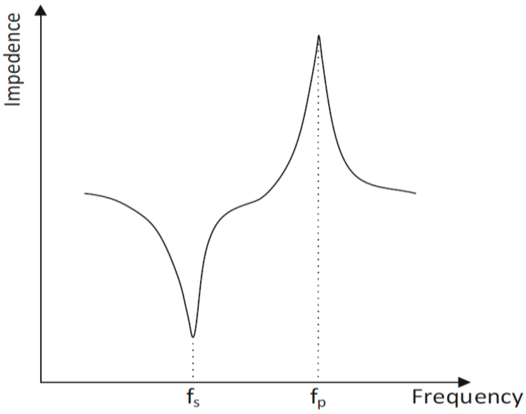

Figure. 2. 18:The typical impedance measurement for a one-port piezoelectric resonator [39].

Piezoelectric material properties are considered the main aspect, that contribute to coupling factor; another definition for this coupling factor has been developed, using the most common equivalent circuit of a resonator (the BVD one-port) [39, 64]. This model consists of a series RLC circuit (C_m the motional capacitance) in parallel with a static capacitance (C_0) as shown previously in Figure. 2.8 From that comparison, the definition of the electromechanical coupling factor of the resonator can be represented as [39, 65,66]:

$$k_{eff}^2 = \frac{C_m}{C_0} \tag{2.21}$$

Both above definitions for the effective coupling factor came from the fact that the piezoelectric coupling factor can be approximated by the same equations described in this section, for an ideal 1D loss-less piezoelectric resonator consisting solely of a piezoelectric body with thin electrodes. As a result, the coupling factor for any piezoelectric-based resonator may be calculated using the same equations [39].

2.6 State of Art on Piezo MEMS Resonators

A good number of utilised piezo-actuated MEMS resonators, designed using different technologies and operating in different modes, were reviewed during this literature review. A summary of these different MEMS resonators is shown in Table.2.5. The year of fabrication, technology used, resonant frequency range, vibration mode and Q_f are given.

Table.2. 5: Reported Thin-Film Piezo-actuated MEMS resonators, including year of publication, technology used, resonant modes.

Ref	**Year**	**Technology Used**	**Vibration Mode / No of Ports**	**f_r MHz**	**Q_f**
[44]	2006	Piezoelectric AlN MEMS	Contour	19 to 656	4300
[67]	2006	Piezoelectric AlN MEMS	Contour / One and Two	80 - 800	1,000 - 4,000
[70]	2007	AlN Film Piezoelectric Sandwiched Between a bottom Platinum Electrode and a Top Aluminium electrode.	Contour	93 - 236	-
[51]	2007	1.5 µm thick AlN film sandwiched between Pt electrodes.	Contour	200 - 800	1,000 – 2,500
[64]	2008	Thin-Film Piezoelectric-on-Substrate (TPoS)	Lateral Bulk Acoustic	94	≈ 3,000
[67]	2008	Zinc Oxide Film Over Silicon-on Insulator Substrates	Lateral Bulk Acoustic	90	3,400
[52]	2010	AlN Film 250 Nm Sandwiched Between 2 Metal Electrodes	Contour Laterally Vibrating / Two	3 - 4.5 x103	566.6
[68]	2011	Thin-Film Piezoelectric-on Substrate (TPoS)	Lateral Bulk Acoustic Wave	2.4 - 3.25 x 103	1,500
[69]	2014	Thin-Film Piezoelectric on Silicon Substrate (TPoS)	Lateral - Extensional	990	2,900
[3]	2015	Thin-Film Piezoelectric-on Substrate (TPoS)	Contour	40	5,637

2.7 Performance Control in RF MEMS Resonators

Maintaining high precision and reliability across numerous performance criteria becomes increasingly crucial as microelectromechanical resonators progress from research labs to commercial applications. The centre frequency (f_0), temperature coefficient of frequency (TCF), quality factor (Q_f), and motional resistance are all important performance measures for MEMS resonators (R_m) [50, 69, 71-74]. Additional characteristics such as power handling and linearity may also be relevant for their application.

Significant research is also directed at the accurate control of MEMS resonator characteristics, and such methods of control can be divided into two types [50,72].

2.7.1 Tuning

This technique can be used in MEMS resonators, to influence the sensitivity of one or several resonator's metrics performance in responding to environmental variations or processing uncertainties, and it is applied to control the following factors:

Thermal Effect: the majority of MEMS resonators has been well characterized, and uncompensated MEMS resonators show large linear temperature dependency, methods of thermal compensation techniques are mentioned in many studies [50,72].

Manufacturing Uncertainties: frequency variation can develop as a result of manufacturing process-induced variations in the device geometry, as well as lithographical errors, and an imperfect etching process used to define the device on the substrate. Other compensation methods and techniques to overcome these issues are described in more detail in recent publications [50,72]. A full correction for resonant frequency variation produced by aging effects requires dynamic modification, which can be achieved by tuning mechanisms requiring extra circuitry. Such frequency tuning can be applied at device level [50,72] These different device- level tuning techniques are described below:

Electrostatic tuning: tan be applied when, a tuneable stiff electrical spring is added in series with the effective mechanical resonators, to create a continuous tuned resonant frequency. This type of tuning is more suited to low-frequency flexural mode resonators [50, 72, 75].

Thermal tuning: this is achieved by a DC current passing through a heating element which results in an increasing resonator temperature and hence creates controlled frequency changes according to the TCF of the resonators [50,72, 76].

Piezoelectric tuning: this tuning method is dependent on the piezoelectric stiffening effect, and it can be applied to piezoelectrically-transduced MEMS resonators. Here the stiffness of the piezoelectric film is controlled by tuning its electric terminals at the tuning port [50, 72, 77], it also called (Voltage tuning). Tuning can also be applied at system levels, where MEMS resonators function as a frequency reference. This technique includes the use of phase-locked loops or the addition of tuneable electrical impedances and phase-shifters (in series and or in parallel) with the resonator [50, 72, 78].

2.7.2 Trimming

Trimming is applied when any device suffers from a permanent shift in one or more of its parameters. This method can be utilised after device fabrication. It can be achieved using selective addition or removal of metal deposits [50, 72, 79]. Another method includes growth of an oxide on the thermally actuated silicon resonators [50, 72, 80] and metal diffusion by the formation of metal-silicon compounds at high temperatures [50,72, 81]. Packaging can create drift in resonance frequency as well, and so trimming is necessary to correct for this, and this can be done by selective laser trimming through a transparent lid of the resonator package [50].

Tuning techniques prompted a review of the state-of-art in tuning, in order to evaluate the possibility of utilising several of these mechanisms to optimise the performance of the present researcher's own fabricated resonators using PiezoMEMS technology. A comparison between different tuning techniques on various types of MEMS resonators is shown in Table.2.6.

Table.2. 6: Tuning in PiezoMEMS Resonators.

Ref No	**Year**	**Technology**	**Vibration Mode**	**Resonant Frequency (MHz)**	***Q_f***	**Type of Tuning**
[44]	2004	Piezoelectric Single-Crystal Silicon (SCS)	Clamped – Clamped	1.72	6200	Voltage
[82]	2011	Thin-Film Piezoelectric-On-Silicon (TPoS)	Lateral	~29.5 -~31.5	-	Passive
[83]	2012	Two AlN-on-Silicon	Latera Bulk Acoustic	427	1400	Voltage
[77]	2008	PZT-on- Silicon	Length - Extensional	13.65 - 15.94	3,820 - 5,040	Voltage
[84]	2010	Piezoelectric AlN MEMS	-	625	-	Thermal
[75]	2011	Thin-Film AlN-on-SOI	Width Extensional	100	3500	Voltage
[85]	2015	Thin-Film Piezoelectric-on-Silicon (TPoS)	Lateral	990	2900	Temperature

2.8 Piezoelectric MUMPS Resonators

The University of Malta has an existing arrangement for research students to create, fabricate and study their own device designs through EUROPRACTICE using MEMSCAP one of its three main foundries. MEMSCAP offers three standard processes as a part of its MUMPs program: POLY MUMPS, SOI MUMPS, and PiezoMUMPs. Access to this technology allows fabrication and testing of MEMS devices and is also cost efficient.

2.8.1 PiezoMUMPs Fabrication Steps

The PiezoMUMPs multi-project wafer (MPW) process can support various designs on one silicon wafer, as a layer's thickness and design [7]. This process begins with a silicon-on-insulator (SOI) wafer having, silicon thickness: 10 ± 1 μm, oxide thickness: 1 ± 0.05 μm, and handle wafer (substrate) thickness: 400 ± 5 μm. It starts with doping of the silicon layer, which is then patterned and etched down to the oxide layer; these two layers act as a mechanical structure. The substrate can be patterned and etched from the “bottom” side to the oxide layer. After that, the thermal oxide layer is patterned and etched in order to provide isolation between the SOI layer and both the AlN and Pad Metal layers [7]. Design and mandatory rules are followed to ensure that all layouts will be compatible with MEMSCAP MEMS’ lithographic and etch process tolerances. A cross-sectional view describing all the layers of the PiezoMUMPs is shown in Figure. 2.19 [7].

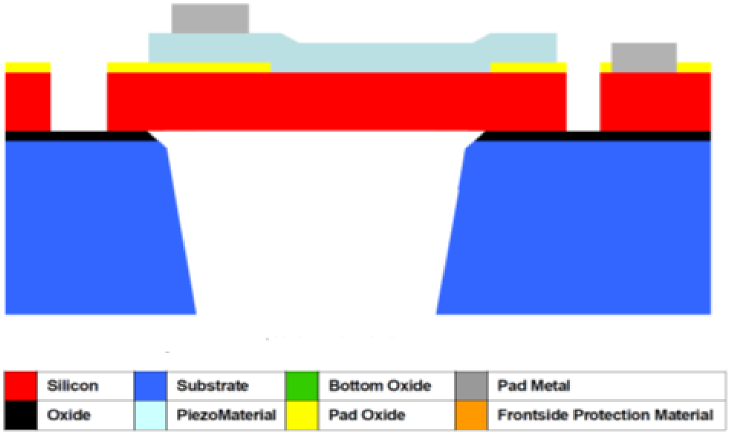

Figure. 2. 19: Cross sectional view including all material’s layers in PiezoMUMPs Process file [7].

2.8.1.1 TRENCH to SOI Overlay

A very crucial step is the TRENCH to SOI overlay tolerance, where the TRENCH to SOI “Edge to Edge” bias accounts less than 50 µm of the etch profile through holes in the Substrate layer and the “blow-out” of the etch profile at the substrate- oxide interface as illustrated in Figure. 2.20 [7].

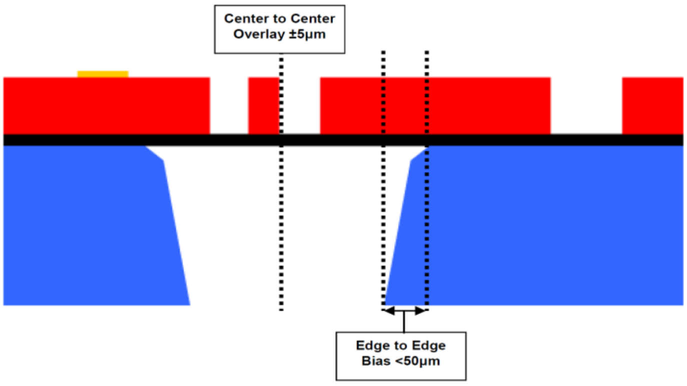

Figure. 2. 20: TRENCH to SOI overlay tolerance [7].

The PiezoMUMPs process is a low-cost technology based on a few process stages. Nevertheless, it is not extensively employed in the design of RF MEMS resonators, including thermal and voltage tuning, making it a challenge for this study. Table.2.7, shows some of the resonators designed using PiezoMUMPs technology, as documented in recent publications.

Table.2. 7: Latest Research on PiezoMUMPs resonators.

Ref	**Year**	**Design Shape / Type**	**Vibration Mode**	**Resonant Frequency (MHz)**
[86]	2014	Rectangular, triangular and trapezoidal cantilevers,	out-of-plane / in-plane bending.	1.370
[87]	2014	Rectangular	Clamped-Clamped	1.6
[88]	2015	Rectangular	Laterally	900
[89]	2016	Square	Clamped plate	0,6
[62]	2018	Rectangular	Laterally	142.1

2.9 MEMS Simulation Tools

Finite Element Analysis (FEA) [86], involves the numerically solution of a set of differential equations describing the physics of a system (such as heat flow and structural mechanics).: these equations are controlled by a set of boundary conditions During the design phase for creating new products, FEA is considered as one of the most flexible methods for anticipating and optimising the performance of MEMS resonators [90]. Furthermore, the cost of MEMS resonator research and development as well as the design cycle may also be significantly decreased. CoventorWare is an integrated set of software tools that may be used to design and simulate MEMS devices. CoventorWare has two independent design flows that can be used separately or in combination, as shown in Figure. 2.21 [90]. While the ARCHITECT module offers a distinctive system-level approach to MEMS design, the DESIGNER and ANALYZER modules work together to provide a more conventional physical design flow. Both design flows require fabrication process knowledge as a starting point, which is provided by a process editor and the material properties database [90].

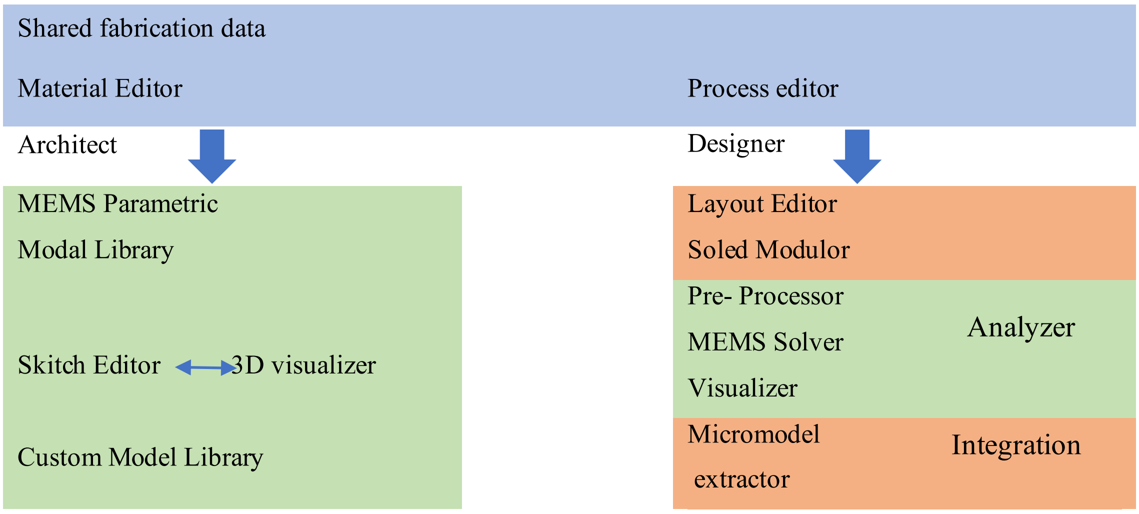

Figure. 2. 21: CoventorWare design flows [90].

The layout editor in DESIGNER is used to first build a 2-D layout. The Solid Modeller creates a 3-D solid model automatically using the layout and layer stack information from the process editor. Subsequently a 3-D model for (Finite Element Modelling) FEM meshing in the Preprocessor's 3-D view will be created [90].

2.10 RF MEMS Switches

Switches for radio-frequency micro-electro-mechanical systems (RF-MEMS) were among the first MEMS devices fabricated using photolithographic processes, including applications such as reconfigurable microstrip antennas, tuneable filters, attenuators, phase shifters and switching networks. [91]. RF MEMS switches utilise the mechanical motion of suspended microstructures to achieve ON and OFF states. These switches outperform classical semiconductor switches [91].

RF MEMS switches can be actuated using electrostatic, electrothermal, electromagnetic, and piezoelectric techniques. Electrostatic actuation is the most widely utilised, due to its simplicity, excellent isolation, low insertion losses, and low power consumption [91], RFMEMS switch can also be categorized depend on their application configuration, deflection behaviour of the suspended plate, and their contact interface [91].

Application configuration: There are two types of RF MEMS switch application configurations [91]:

The series type RF-MEMS switches: are linked in series with the transmission line, allowing no signal to travel through the line when the switch is in the normal position.

The shunt type RF-MEMS switches: are in the 'on-state' in the typical position, allowing the RF signal to flow. With the application of an actuation force, the top suspended plate contacts the bottom fixed electrode, providing a ground channel for the RF signal and turning the switch into a 'off-state'.

Deflection behaviour of the suspended plate: RF-MEMS switches are categorized into Lateral or Vertical type depend on the direction of movement [91]:

Lateral: The suspended plate is moved in the wafer plane direction using any of the actuation methods in the lateral configuration, and switching behaviour is obtained by contact of the suspended plate with the sidewall [91].

Vertical: The suspended plate is moved out of the wafer plane in the vertical configuration, and the switching behaviour is achieved by the suspended plate's contact with the bottom fixed electrode. The suspended plate in vertical RF-MEMS switches is either manufactured as a fixed-free microbeam (microcantilever) or as a clamped-clamped microbeam (microbridge) [91].

Contact Interface: In RF-MEMS switches, the contact interface can be categorised into [91]:

Ohmic (Electrical – Mechanical Contact): Between the top suspended plate and the bottom fixed electrode, there is an air gap. However, when an actuation force is applied, the air gap closes, resulting in a metal to-metal contact between the plate and the fixed electrode. For low-frequency applications, this design is frequently favoured [91].

Capacitive (Electrical Contact): A thin dielectric layer covers the bottom fixed electrode, and an air gap exists between the suspended plate and the dielectric. The top plate lands on the dielectric when the actuating force is applied [91.

Capacitive (Mechanical Contact): Series lateral electrocoated switches there is no dielectric layer covering the side wall of the SOI layer, when force is applied there is a mechanical contact between the SOI layers at ON state [91].

Capacitive (Non-Contact): The switch is independent of stiction and charge injection problems that arise in contact-type RF MEMS switches, especially when they have gold plated side wall in their signal line profile resulting in increased reliability and longevity. The contactless switch uses electrostatic actuators to regulate changing capacitance between signal lines and moveable grounded electrodes. Because the moveable grounded electrode may slide in both directions, the switch can be switched between ON, OFF, and deep OFF states [8,9].

Although both ohmic and capacitive switch interfaces can be used with both series and shunt type RF MEMS switch topologies, ohmic interfaces are more commonly used with series type RF-MEMS switches and capacitive interfaces with shunt type RF MEMS switches [91].

The performance of RF MEMS switches is measured using a variety of metrics including:

1. Pull-in Voltage: Electrostatically-actuated RF-MEMS switches are one of the most popular and essential mechanisms having had many research papers focussed on it. Its actuation (or pull-in) voltage V_p can be given theoretically by the equation (2.22) [112]. This equation allows for reduction of the actuation voltage, by either lowering the spring constant and air gap or by increasing the overlapping area of the actuation electrodes.

$$V_{pull-in} = \sqrt{\frac{8k_z\, g_0^3}{n27\varepsilon_0 A}} \tag{2.22}$$

Where, k_z is the total spring constant; g_0 is the initial air gap between the membrane and the signal line; ε_0 is air permittivity, n is the number of gaps and A is the overlapping area of the actuation electrodes [112].

2. Insertion Loss: The RF loss dissipated in the switch during the 'on-state' is known as insertion loss. It is a measurement of the signal transmission efficiency of an RF-MEMS switch. Equation 2. 23 gives the insertion loss for a signal entering and leaving the RF-MEMS switch [91].

$$Insertion\ loss = 10\ log_{10}\frac{P_B}{P_A} \tag{2.23}$$

Where P_B denotes the power received by the load before the RF MEMS switch was inserted into the transmission line, and P_A denotes the power received by the load after the RF MEMS switch was inserted into the transmission line [91].

3. Bandwidth: The frequency band in which the RFMEMS switch can operate with minimal losses is referred to as bandwidth [91].

4. Switching Time: The time it takes for an electrostatically actuated RF MEMS switch to change from on to off and vice versa is known as switching time. Equation 2.24 can be used to compute the switching time [91].

$$t_s = 3.67\,\frac{V_p}{V_s}\,\sqrt{\frac{m}{k_m}} \tag{2.24}$$

where V_p is the pull-in voltage, k_m is the mechanical spring constant, m is the structure's effective mass, and V_s is the actuation voltage [90].

2.10.1 Electrostatic RF MEMS Switches

RF-MEMS switches have gained substantial interest due to their remarkable electrical performance, low cost, reduced insertion loss and small size make them preferable to the traditional solid-state solutions [8].

Contact type switches are categorised into two kinds: metal contact and capacitive coupling switches. However, in general these switches are limited by various problems which impacts their reliability. Examples of contact type switch's range of reliability problems are listed in Table.2.8 [8].

Table.2. 8: Contact-type switches reliability problems [8].

Switch	**Problem**
Metal contact	- Contact resistance increment in value. - Micro welding.
Capacitive coupling	- Between the dielectric layer and the metal, there is friction. - Dielectric layer charge injection, trapping.

Therefore, to overcome the problems in Table. 2.8, a non-contact type RF MEMS switch was proposed in [8] and [9], and was successfully implemented and fabricated using the technology of SOI MUMPs [9] as shown in Figure. 2.22.

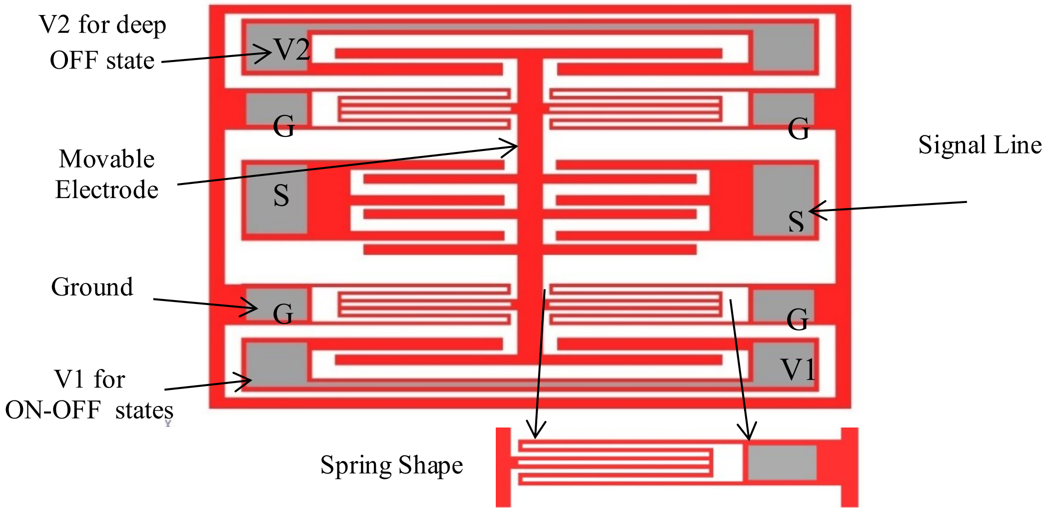

Figure. 2. 22: Primary design of a 3 state non-contact Switch, including spring shape [9].

The non-contact switch presented in [9], is a capacitive shunt type: its operation mechanism is based on the signal line and laterally movable grounded electrodes' capacitance variation. This switch can operate as a two state (ON, OFF) or three state (ON, OFF, deep-OFF) switch as reported in [9]. In the case of two state operation. in the OFF state, the capacitance between the fixed and movable electrodes is small enough to block most RF by large impedance. When an actuation voltage (V_1) is applied across the two capacitive actuation electrodes, the laterally movable grounded electrodes are brought closer to the signal lines. Therefore, large capacitance and low impedance can be achieved to allow RF signal to pass through. As a small air gap 3µm exists between the signal lines and movable grounded electrodes in ON state. Furthermore, the device has the capability to provide the deep-OFF state by applying the voltage (V_2) between two electrodes to achieve a deep-OFF state [9].

2.10.2 State of Art of Electrostatic RF MEMS Switches

For a more comprehensive view of the developing direction of RF MEMS switches over the past 25 years, the switches and their characteristics covered in some published articles are listed in the following Table.2.9 in chronological order [87].

Table.2. 9: The development of MEMS switches over the past 27 years in chronological order [90].

Ref	Year	Actuation Voltage (V)	Pull–in Voltage (V)	Insertion Loss (dB) / Frequency (GHz)	Isolation (dB) / Frequency (GHz)
[92]	1995	28	N/A	0.1 / 4	-50 / 4
[94]	1999	N/A	50	0.14, 0.25 / 20, 35	24, 35 / 20, 35
[95]	2000	N/A	9	0.16 / 40	-15, -26 / 15, 40
[96]	2001	8	8 – 15	0.08 / 10	42 / 5
[98]	2004	N/A	23.3	< 0.2 / 15	>20 / 1 – 25
[97]	2005	50	37	-2.3 / 30	N/A
[99]	2008	N/A	36	-0.7, -2.8 / 4, 15	-30, -21 / 4, 15
[8]	2009	25 V	N/A	1.43 - 30.1	30.1- 50.5
[100]	2010	N/A	10.7 –12	0.13 – 0.2 / 2, 5, 10, 15	41.25–23.57/2,5,10,15
[101]	2010	19, 23	16.2, 19.4	1.15 – 1.3 / up to 40	23, 27 / up to 40
[102]	2011	50	N/A	-0.2 / 20	-22 / 20
[103]	2011	55	N/A	0.2, 0.35 / Up to 20	23, 12-26 / 3, 10
[105]	2011	40	N/A	< -1 / 25	-60 / 25
[104]	2012	N/A	5.8 – 15	< 0.65 / 65	> 40 / 61, 73
[106]	2014	N/A	20	-0.1 / 20	-43 /9.5
[107]	2015	15	9	-0.3 - 0.4 / 3 – 20	-20 to -44 / 3-20
[108]	2015	N/A	11.75	< 0.11 / 1 -25	N/A
[110]	2015	0 – 60	30	N/A	N/A
[9]	2015	123 V	N/A	−3.98 -−0.86	-20.15 – 13.81
[109]	2016	N/A	6	0.01-0.10 / 1-25	3.98-16.74 / 1-25
[111]	2016	60	N/A	9.13 / 70	24.37 /70
[112]	2016	N/A	18.75	0.25 / 20 – 35	> 20 / > 20
[113]	2017	N/A	14.6	-0.85 / 22	N/A
[114]	2017	42, 36	42	< 0.4 / 40	>20 / 11.28-30.28
[115]	2017	18.3	18.3	0.29 / 35	20.5 / 35
[116]	2017	2.9	-	-10/ 40	-58/ 27
[117]	2019	2.2	-	-11.5 /40	-71/ 30.5
[118]	2022	9.1	-	-0.065/ 30	-40/30

The optimisation of electrostatic MEMS switches is mainly involves reducing its actuation voltage, by optimization of comb fingers, actuator gap, and reduction of the spring constant. However, the reliability problems of contact type switches resulting from micro welding and non-zero contact resistance have not been entirely investigated.

2.11 Research Gap

In this literature review, a comprehensive study of the state of art on RF-MEMS resonators has been presented. However, PiezoMUMPs technology in designing and fabricating LBAW PiezoMUMPs resonators has not received a detailed analysis of the temperature effect on the performance of this type of resonator to date. Furthermore, to obtain a wider range of frequency tuning, it is necessary to utilise multiple resonators and associated switching elements.

In this Ph.D. research the access to PiezoMUMPs technology permits a feasibility study on the design of piezoelectric MEMS lateral bulk acoustic wave resonators, with reference to thermal effects on the resonant frequency. This will be the first time the viability of implementing thermal and voltage fine tuning techniques on this type of RF-MEMS resonators will be investigated. Design considerations for a number of these high Q-factor LBAW Piezo MEMS resonators, is also investigated and reported. The application of fine-tuning techniques using thermal and voltage approaches has not been previously implemented on PiezoMUMPs resonators. A non-contact type of RF MEMS switch was also proposed and then successfully implemented and fabricated using the technology of SOI MUMPs [88]. This has prompted a new range of opportunities to experiment with PiezoMUMPs technology because the fabrication processes are nearly identical. Furthermore, this work will proceed by implementing a switchable array of resonators to achieve a wide tuning range and this will be achieved by a non- mechanical contact using electrostatic actuation. Another novel addition is the integration of switches with resonators in the same chip, this will be resulting in a cost reduction.

3. Design Optimization Issues for LBAW MEMS Resonators

This chapter investigates the use of PiezoMUMPs technology to design and fabricate Lateral Bulk Acoustic Wave (LBAW) MEMS resonators operating in the range of 30 - 62 MHz. The design methodology, resonant mode, number of modes, and quality factor are thoroughly examined, with verification results provided for two devices differing in their dimensions: RES1_2E (216 x 100 μm). An optimised version of this device, RES2_2E (350 x 250 μm), is also introduced, where E denotes the number of electrode elements. Additionally, detailed discussions on design considerations and optimisations are presented, along with simulation results obtained using CoventorWare FEM simulation tools. The chapter further includes characterisation results for these two LBAW PiezoMUMPs resonator prototypes.

Furthermore, when designing piezoelectric resonators, one of the most significant factors designers need to consider is determining their Quality factor (Q_f) at the resonance frequency. This chapter comprehensively details the parameters that influence the value of the resonator quality factor.

3.1 Design Methodology

The primary steps of this study involve conducting simulations using CoventorWare's design tool, inspired by the work presented in [3], this project aims to develop a PiezoMUMPs resonator that can effectively operate in an LBAW mode. Begin by creating two PiezoMEMS resonators with identical dimensions, but utilize different piezoelectric materials: one with aluminium nitride (ALN) and the other with lead zirconate titanate (PZT). Design considerations are also discussed, including the effect of the number of electrodes on the mode shape and the effects of the tether and resonator geometry on the quality factor. It is important to note that all these studies are conducted following the mesh convergence study. This will lead to the designing and manufacturing an optimised LBAW PiezoMUMPs resonator operating in the 30 -62 MHz range.

3.2 Design Steps and Simulation Analyses

Using CoventorWare simulation tools, RES1_2E will be created by replicating the same layout shown in [3], and the 3D model will be simulated. When simulating RES 1_2E, the same design dimensions (L x W = 216 x 100 µm) described in [3] have been used. The two considered resonators differ in the piezoelectric material type and, thicknesses, and SOI thickness. The 1st resonator features a 1 µm thickness of PZT and a 5.5 µm SOI layer (referred to as PZT_RES_2E) while, the 2nd resonator incorporates 0.5 µm of AlN and a 10 µm SOI layer. Figure. 3.1 illustrates the 3-D model of an LBAW PiezoMUMPs resonator (RES1_2E), and Table.3.1 provides information on the resonators' notation to be studied in this chapter along with their corresponding geometric properties.

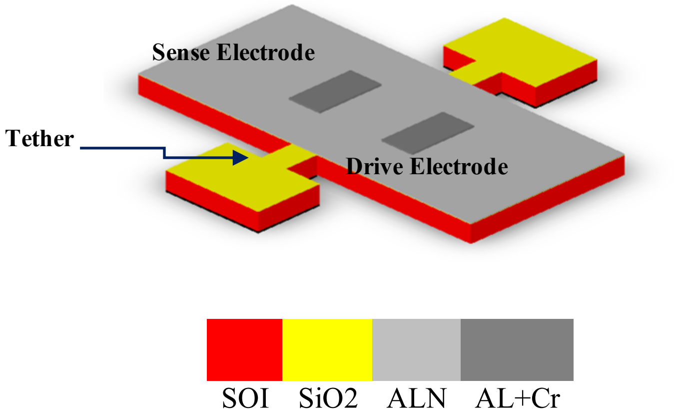

Figure. 3. 1: The 3D model of RES1_2E based on the PiezoMUMPs technology using CoventorWare (RES1_2E).

Table.3. 1: Resonator Notation along variations in resonator geometry, tether structure, number of electrode elements, and thermal elements existence.

Resonator Notation	Resonator Dimensions (µm)	Tether Dimensions (µm)	Curved Tether	No of Electrode Elements	Thermal Element
RES1_2E	216 x 100	20 x 16	-	2	-
RES2_2E	350 x 250	20 x 38	-	2	-
RES2_2E_Th	350 x 250	20 x 38	-	2	✓
RES2_5E_TH	350 x 250	20 x 38	-	5	✓
RES3_5E_V1	350 x 250	20 x 38	-	5	-
RES3_2E	350 x 250	20 x 38	-	2	-
RES3_3E	350 x 250	20 x 38	-	3	-
RES3_5E_V2	350 x 250	20 x 22	-	5	-
RES3_5E_CT	350 x 250	20 x 22	✓	5	-
RES3_5E_V3	350 x 250	35 x 22	-	5	-
RES3_5E_V3_CT	350 x 250	35 x 22	✓	5	-
RES3_5E_V4	350 x 250	50 x 22	-	5	-
RES4_5E_V1	350 x175	20 x 38	-	5	-
RES4_5E_V2	350 x 175	20 x 22	-	5	-
RES4_5E_V3	350 x175	35 x 22	-	5	-
RES4_5E_V3_CT	350 x175	35 x 22	✓	5	-
RES5_5E_V1	350 x 350	20 x 38	-	5	-
RES5_5E_V2	350 x 350	20 x 22	-	5	-
RES5_5E_V3	350 x 350	35 x 22	-	5	-
RES5_5E_V3_CT	350 x 350	35 x 22	✓	5	-
RES5_5E_V4	350 x 350	50 x 22	-	5	-

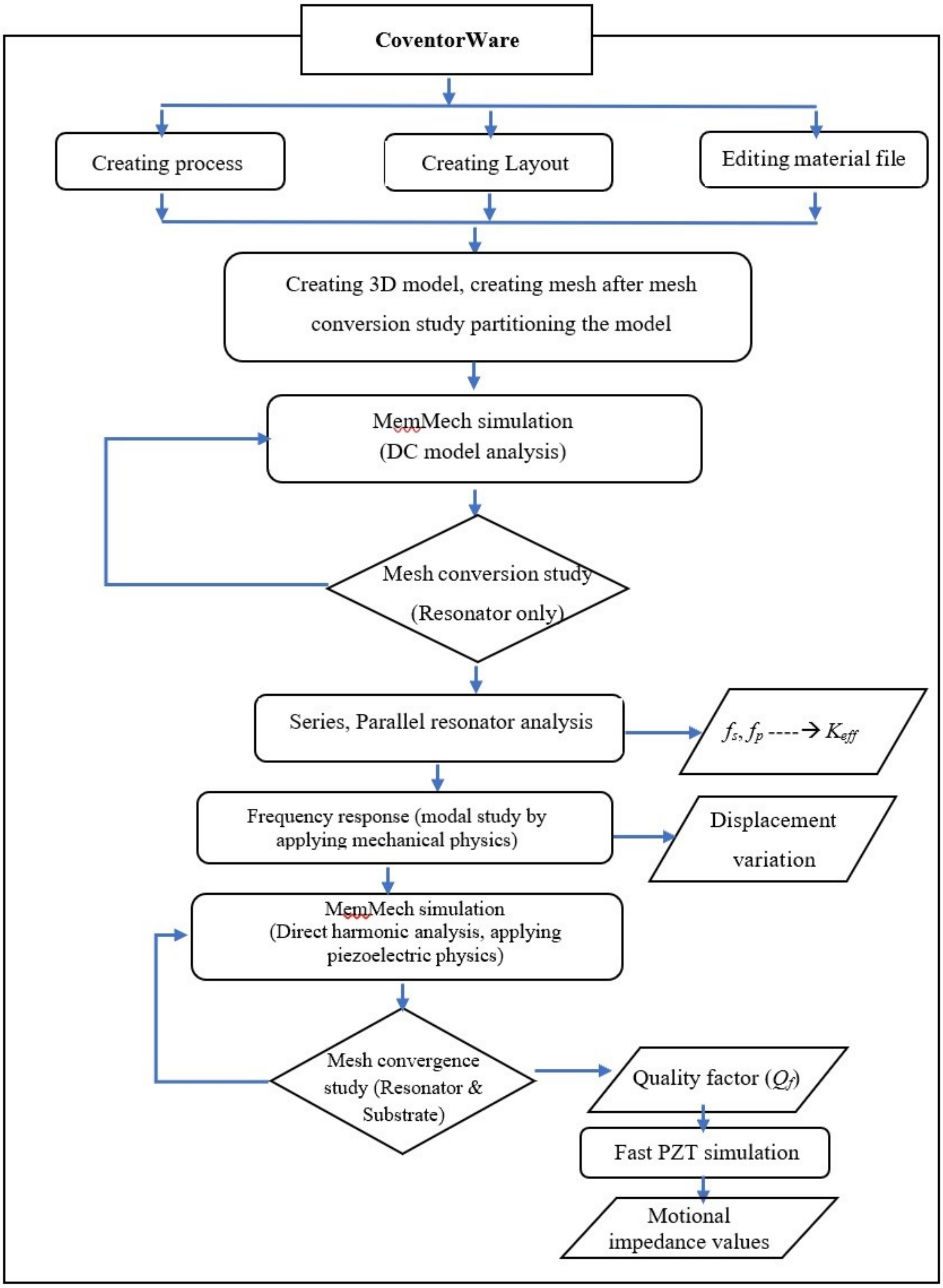

Figure. 3. 2: Resonator simulation steps using CoventorWare simulation toolkit.

3.3 LBAW PiezoMUMPs Resonator

The 3-D finite-element method (FEM) of the mechanical solver (Mem-Mech) is one of the leading numerical approaches in solving partial differential equations for any mathematical physics of any 3-D model in CoventorWare analyser. This solver is used to determine displacement and stress values, by applying a (fix-all) in boundary surface condition (BCs) at fixed points where the anchors are connected to the substrate from both sides and its derived meshes are created in the solver modules, often under constraints set by the user in the solver setup [118].

The density of the mesh determines the accuracy of the discrete partial differential equation [118].

3.3.1 Mesh Study for 1st Mode LBAW PiezoMUMPs Resonator

Mesh convergence is the process of measuring the accuracy of an FEM analysis, which can be assessed by comparing results on meshes with increasing degrees of freedom (number of elements or density) [90]. To conduct an effective mesh convergence study, it is essential to consistently refine the mesh to maintain appropriate element aspect ratios [90]. In this study, multiple models are created with different element sizes and applied to the 1st mode LBAW PiezoMUMPs resonator. For this purpose, Manhattan bricks with parabolic interpolation are selected as the mesh type, and the element size is adjusted in the X, Y, and Z directions. After generating the mesh, the Mem-Mech modal solver is executed to determine the resonant 1st mode and determine the effective mass for each mesh size. The initial mesh is created with 15 x 15 x 7.5 μm element sizes, and the smallest mesh has element sizes of 5 x 5 x 2.5 μm. Table.3.2 and Figure. 3.3 show the mesh for simulating the resonant frequency for RES1_2E. The numerical solution of the model will approach a unique value as the density of the mesh increases. The convergence of the mesh occurs when additional refinement results in a negligible change in the solution. The model yields a mathematically accurate solution if the two meshes produce the same result. A logarithmic representation illustrates the values of the independent variables obtained through an efficient mesh refinement scheme, as showed in Figure. 3.4.

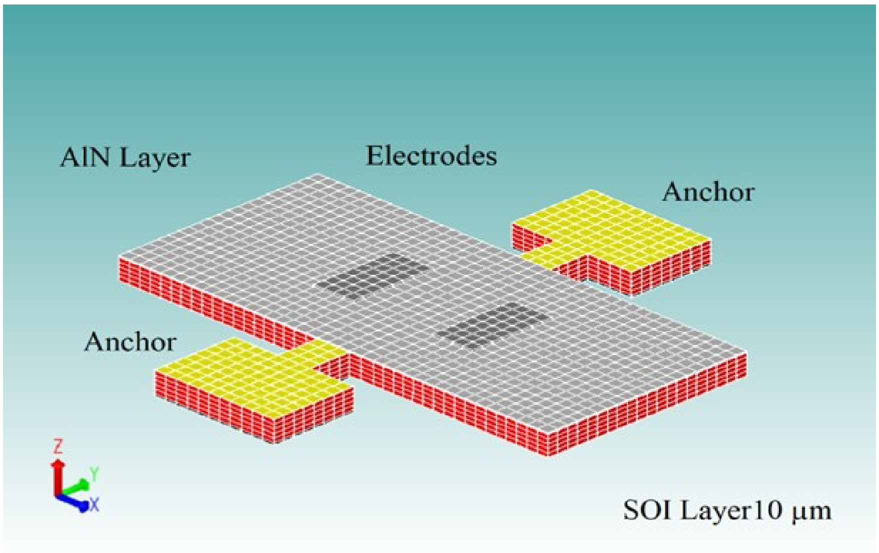

Figure. 3. 3: Mesh used for simulating the resonant frequency of RES1_2E.

Table.3. 2: Mesh convergence on the 1^{st} Resonant mode of RES1_2E.

Mesh Size (µm)	Volume - Nodes	1/Nodes	Resonant Frequency, f_r (MHz)	Effective Mass (ng)	log (f_r)
15*15*7.5	280	3.571E-03	20.030	69.322	7.30168
10*10*7.5	952	1.050E-03	20.000	69.322	7.30103
7.5*7.5*3.5	1644	6.083E-04	19.995	69.322	7.30092
5*5*2.5	7204	1.388E-04	19.969	69.322	7.30036

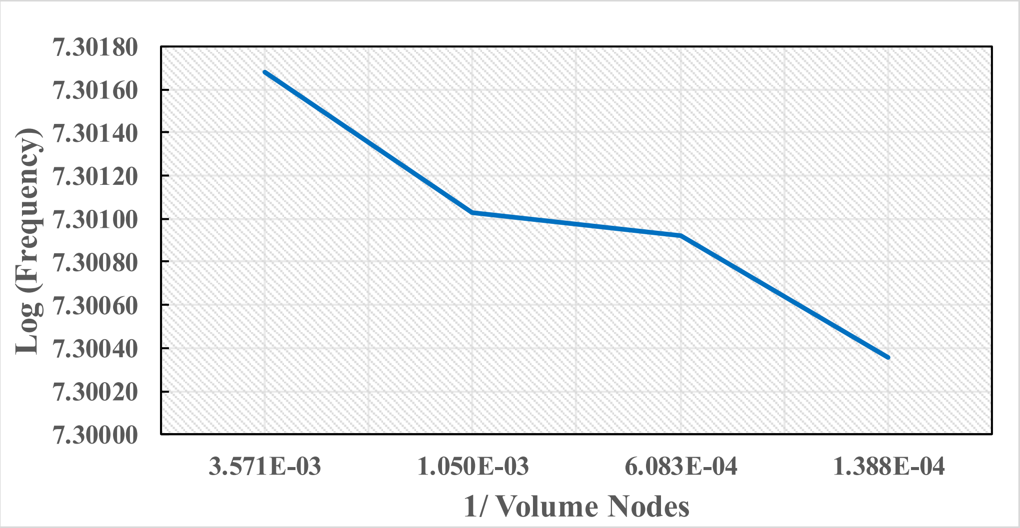

Figure. 3. 4: 1st Resonant Mode Mesh convergence Study for LBAW PiezoMUMPs (RES1_2E).

3.2.2 DC Analyses for LBAW Piezo MUMPs Resonator

The Mem-Mech solver performs a DC analysis on the piezo stack of RES1_2E, a nominal value of 1V is applied to the top electrode, resulting in a maximum displacement of 13 µm in the X direction for 1V. The charge response, obtained through the Mem-Mech simulation, indicates a total charge of 1.07 pC on each of the opposite piezo surfaces. This simulation is conducted by selecting the mechanical physics and employing the Manhattan brick mesh type. To examine the 1st lateral bulk acoustic resonant mode, the natural resonant frequency for this mode was determined to be 19.969 MHz for the PiezoMUMPs resonator. Figure. 3.5 depicts the lateral vibrational deformation of PiezoMUMPs resonator at the first mode resonant frequency.

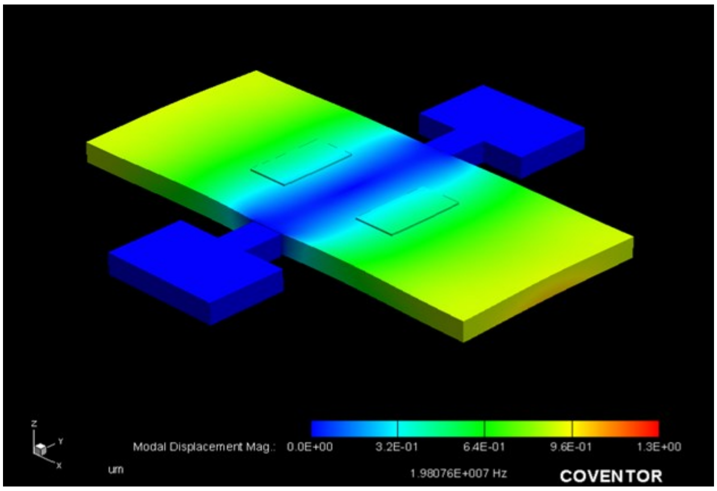

Figure. 3. 5: 1st resonant mode lateral deformation of RES1_2E.

3.2.3 Harmonic Analysis for LBAW PiezoMUMPs Resonator

The Butterworth–VanDyke (BVD) circuit can represent a piezo acoustic resonator as an equivalent impedance model, as discussed in Chapter 2, section 2.3.1, and illustrated in Figure. 2.8. The equivalent circuit's motional inductance, L_m, represents the resonator's effective mass. An analogous motional resistance, R_m, represents the mechanical losses, while a motional capacitance, C_m, represents the resonator's effective spring constant. The electrodes on the piezoelectric surface layer results in a static parallel plate capacitor, or stack capacitance C_o [118]. Assuming no losses in the BVD circuit, the series resonance, which signifies the resonant frequency of the series circuit where L_m and C_m are connected in series, also corresponds to the resonance frequency of the mechanical component of the BVD circuit. Simulating a short circuit piezoelectric modal analysis is conducted in CoventorWare. Since both electrodes in this simulation are grounded, the piezo effect is eliminated, and the resonance frequency is calculated only from structural effects; this simulation is also known as closed-circuit resonance analysis and the resonant frequency will be called series resonant frequency (f_s) [118]. Using Modal analysis , the resonant frequency f_s was found to be 20.0023 MHz.

If driven under constant charge conditions, the simulation is for open circuit, where the resonant frequency this time will be referred to as the parallel frequency (f_p) This represents the resonant frequency of a circuit where motional impedances L_m and C_m are in series in one branch, parallel with C_0, and by running the same simulation for an open circuit, f_p found to be 20.0041MHz.

The parallel resonance frequency in CoventorWare is calculated by running a piezoelectric modal analysis with open circuit conditions. Hence, this simulation is also known as open-circuit resonance analysis, where one electrode is grounded, and the other is left floating [118]. In reference to Equations 2.18, 2.19, and 2.21 in the previous chapter, values of motional impedances C_m and L_m can be calculated as follows:

$$C_m = C_0 \left[\left(\frac{f_p}{f_s}\right)^2 - 1\right] \tag{3.4}$$

$$L_m = \frac{1}{(2\pi f_s)^2\, C_m} \tag{3.5}$$

$$K^2{}_{eff} = \frac{\pi^2}{2} \cdot \frac{C_m}{C_0} \tag{3.6}$$

Thus far, the calculated C_m = 19.205 fF and L_m = 33.00 nH where $K^2{}_{eff}$ is the effective coupling coefficient, and it can be calculated from the fitted values of C_m and the designed values of C_0 (Chapter 2, Section 2.5.2.1). The motional resistance, R_m, is the only element of this circuit that has not yet been evaluated. This analogous model's resistive component contributes to energy dissipation, which is mechanically caused by damping; this will be described in (Chapter 4, Section 4.2) when Q_f is determined via Fast PZE simulation.

3.3.4 Quality Factor (Q_f) Analysis

Piezoelectric transduction-based MEMS resonators often exhibit a relatively low-quality factor, significantly limiting their potential in various applications, such as high-sensitivity sensors, narrowband filters, and low-phase noise oscillators [119,7].

A higher Q-factor can be achieved with lower energy dissipation, and anchor loss is widely acknowledged as the primary contributor to crucial loss processes in piezoelectric resonators [7,86].

An increased Q anchor is contributing to an overall improvement in the total quality factor, as it is also considered the primary source of energy dissipation in this study [118].

In the BVD circuit explained in Chapter 2, section 2.3.2, the quality factor representing the circuit's effectiveness is provided by

$$Q_f = \frac{2\pi f L_m}{R_m} \tag{3.7}$$

Gas/air damping, thermoelastic damping, acoustic radiation losses through anchors, material damping, and other damping that is typically less significant are losses that contribute to this Q_f, the overall quality component, as mentioned in Chapter 2, Section 2.5.1.1.

In Q_f, anchor losses simulation the FE analysis type is Piezo direct harmonic analysis. There are multiple reasons for this preference. Firstly, Piezo Direct harmonic analysis solves the complex steady-state problem at each driving frequency. Additionally, it considers anchor losses [118] and relies on mesh density for support. The representation of the substrate in the simulation is crucial. A cube shape is used to model the substrate, which allows for determining the quality factor value at the resonant point. Numerical calculations suggest that the substrate dimension considered in the simulation should be at least as large as the wavelength of the relevant acoustic pressure wave inside the substrate. This can be determined using the following formula:

$$\lambda = \frac{1}{f}\sqrt{\frac{E}{\rho}} \tag{3.8}$$

Furthermore, when selecting the substrate mesh size, λ must also be considered, and its dimensions must equal or less than λ/10. The following section will explain in more details of the effect of the substrate volume considered as well as the mesh size in simulating the quality factor due to anchor losses.

3.3.4.1 Substrate Modelling for Quality Factor

The quality factor simulation begins with creating the 3D model and meshing both resonator and substrate. Next, the mechanical simulation (Mem-Mech) should be chosen, followed by selecting piezoelectric physics to carry out the direct harmonic analyses. Designing the substrate 2D layout with dimensions of 1000 x 1000 x 400μm having a mesh size of 45 μm and the resonator RES1_2E meshed with size of 15 μm.

The mesh size is crucial factor to consider in this simulation, for instance, running the simulation having two different meshed regions will results Q_f value 237 at first resonant mode 19.14 MHz. Assigning the same 10μm mesh size to both resonator and substrate is an alternate method that saves time. As shown in Figure 3.6, the 3-D model of one half of both of resonator and substrate structure, and by applying symmetrical boundary conditions, the FEM simulation time has reduced to half. Furthermore, this anchor losses simulation was conducted without mesh convergence study, in order to have accurate results a mesh study will conducted and explained in details in section 3.5.

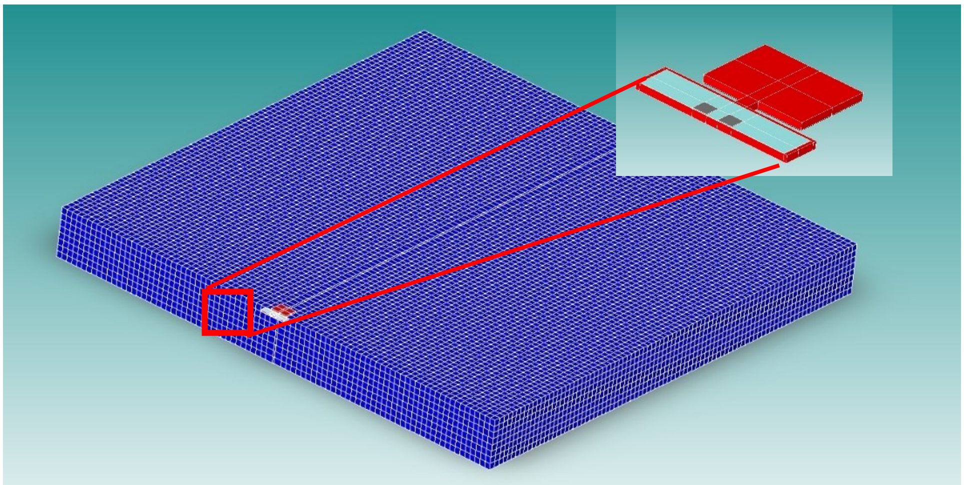

Figure. 3. 6: A 3-D model of one side of the substrate used in the FEM simulation on RES1_2E, applying symmetry boundary conditions and the same mesh size.

3.4 LBAW PiezoMUMPs Resonator Design Adjustments

From previous sections, it can be justified that the technology of PiezoMUMPs can be applied in designing LBAW PiezoMUMPs resonators. The 1st mode resonant frequency was simulated using a prior design, RES1_2E, and a modified copy, RES2_2E. Aside from the number of electrodes, which alone affects the resonant mode, other factors, such as tether size and shape, also impact energy dissipation and the resonant frequency and quality factor. The following sections will cover these factors in more detail.

3.4.1 Electrodes Dimension Adjustment

Given that Res1_2E's electrode dimensions have been altered to the max size, since the previous size, the electrode/sense's size was considered small. Therefore, to verify the first-order resonant frequency, it is necessary to carry out a mechanical modal simulation. Figure. 3.7 shows RES1_2E_V2 with two enlarged electrodes (D$_l$ x D$_W$ = 90 x 80 µm) and a 1st mode frequency of 19,127 MHz.

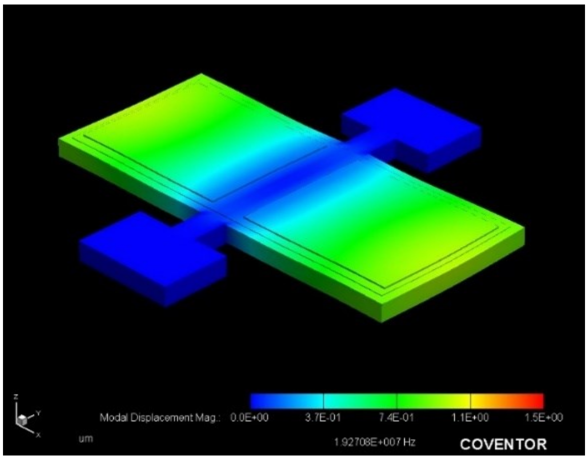

Figure. 3. 7: 1st resonant mode of Res1_2E_V2 with Large Electrode Elements.

3.4.2 Resonator Dimension Adjustment

By expanding the resonator's dimensions to 350 x 250 µm and their tether dimensions T$_l$ x T$_W$ from 20 x 16 µm to 20 x 38 µm, also the electrode elements size (D$_l$ x D$_{W)}$ were increased to 162 x 230 µm. This resonator is designated be as (RES2_2E_V2). It is planned to achieve a higher resonant frequency at a higher mode with an acceptable quality factor value. Following this modification a Mem-Mech simulation with fixed boundary conditions was conducted to verify the 1st mode resonant frequency. Figure. 3.8 shows RES2_2E_V2 modal displacement simulation results having a 1st mode resonant frequency of 19.14 MHz; this device can also operate at the 3rd and 5th modes. Table.3.3 shows the dimensions of these four resonators.

Table.3. 3: Four different LBAW PiezoMUMPs resonators and their geometry variations.

Resonator Notation	Resonator Dimensions (L x W) (µm)	Resonator's tether Dimensions (T_l x T_w) (µm)	Resonator's Electrode Element Dimensions (D_l x D_w) (µm)
Res1_2E	216 x 100	20 x 16	20 x 40
Res1_2E_V2	216 x 100	20 x 16	90 x 80
Res2_2E	350 x 250	20 x 38	20 x40
Res2_2E_V2	350 x 250	20 x 38	162 x 230

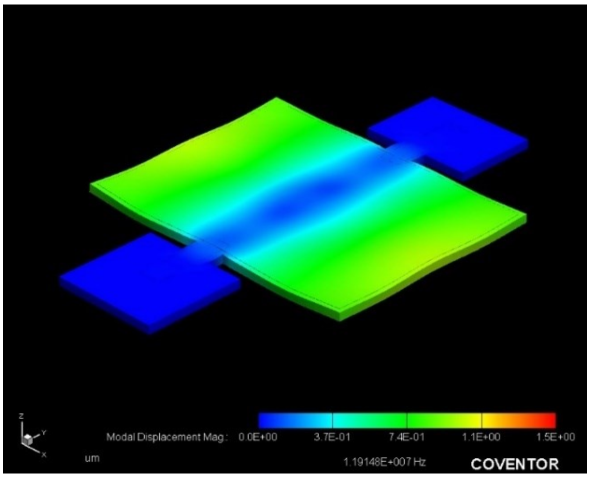

Figure. 3. 8: 1st resonant mode of RES2_2E_V2 with Large Electrode Elements.

3.4.3 DC and Harmonic Analysis Comparison

Conducting DC and harmonic analysis for the four previously discussed resonators was essential in comparing their motional impedance values, as shown in detail in Table.3.4. The value of the motional impedance parameters was adequate at this step to decide on the proper dimensions for the resonator and its electrode elements.

Table.3. 4: DC and Harmonic Analysis for LBAW PiezoMUMPs Resonators with different two-element electrode sizes in the 1st mode.

Small circuit Parameters	**RES1_2E**	**RES1_2E_V2**	**RES2_2E**	**RES2_2E_V2**
C_0 (pF)	1.07	4.5	1.59	9.3
f_s (MHz)	20.0023	19.2724	11.9066	12.0726
f_p (MHz)	20.0041	19.2827	11.9148	12.0738
C_m (fF)	0.19	4.8	0.3	12.8
L_m (H)	0.33	0.0142	0.5505	0.0139
K_{eff}^2	0.0009	0.0053	0.0010	0.0068

As depicted in the preceding table, RES2_2E_V2, which incorporates 2E electrodes, demonstrated the highest Keff2 value, this made it the best choice for the forthcoming study. It should be noted that Lm and Cm are impedance referred to the input port, and thus, their magnitude is scaled by Keff2 coefficient.

3.4.4 LBAW PiezoMUMPs Resonators / Different Numbers of Electrode Elements

To determine resonant frequency at higher modes, such as the 3rd and 5th modes, it was necessary to check the mechanical behaviour by running a mechanical simulation (Mem-Mech) of the designed resonators, and resonant frequencies at the 1st, 3rd, and 5th modes are displayed in Table.3.5 for RES3_2E, RES3_3E, and RES3_5E_V1. All three resonators have the same architecture as RES2_5E_V2, the same dimensions, and the same tether size. Only the number of electrode elements and the electrode shapes are different.

Table.3. 5: LBAW PiezoMUMPs resonators with different electrode elements resonating at the 1st, 3rd, and 5th modes.

Resonator Address	**RES3_ 2E**	**RES3_ 3E**	**RES3_5E_V1**
Design / Electrode shape	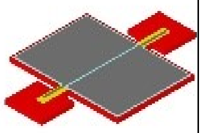	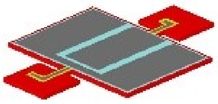	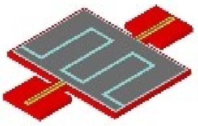
1st resonant Frequency (MHz)	11.9	11.8	11.6
3rd resonant Frequency (MHz)	36.5	36.4	36.0
5th resonant Frequency (MHz)	60.8	59.4	59.9

The mechanical simulations findings do not support the argument sufficiently, that RES2_ 5E_V1, with its five electrode elements, is the best alternative. The following section will discuss more simulations, including quality factor simulation.

3.5 Mesh Study for the 5th Mode LBAW PiezoMUMPs Resonator

The LBAW PiezoMUMPs resonator with RES3_5E_V1 dimensions and a specific number of electrode elements has been identified as the most suitable layout for manufacturing and characterisations in this project. However, before proceeding, several simulations need to be conducted. Figure. 3.9 illustrates the 3D model of the designed resonator, which has a mesh size of 5 x 5 x 2 µm and is ready for simulation. This mesh study aims to determine the appropriate element size to be selected for conducting DC and harmonic analysis simulations (T_l x T_w = 20 x 38 µm). This resonator will be referred to as RES3_5E_TH, where TH signifies the inclusion of the thermal element in the design. Table.3.6 shows the resonator geometry parameters, including layer thickness.

Table.3. 6: Resonator geometry parameters, including layer thickness.

Parameter	**Value (µm)**
Resonator Length, l	350
Resonator Width, W	250
Length of tether, T_l	20
Width of tether, T_W	38
Electrode gap	10
Piezoelectric layer Thickness, Pt	0.5
Electrode Thickness, E_t	1.02
Oxide Thickness	0.5
SOI Thickness	10
Silicon Substrate high	400

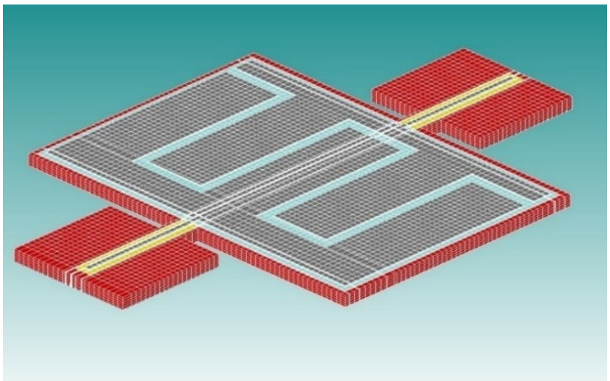

Figure. 3. 9: Mem-Mech model analysis with mesh setting for 5E-electrode LBAW PiezoMUMPs resonator (RES3_5E_TH).

Table.3.7 and Figure. 3.10 show Mesh convergence on the 5th mode LBAW PiezoMUMPs resonator (RES3_5E_TH).

Table.3. 7: Mesh convergence on the 5th mode LBAW PiezoMUMPs resonator (RES3_5E_TH).

Mesh Size (µm)	**Volume Nodes**	**1/Nodes**	**Frequency f_r, (MHz)**	**General Mass**	**log (f_r)**
15*15*6	17816	5.61E-05	58.5	2.84E-10	7.76734
10*10*4	27759	3.60E-05	59.2	4.45E-10	7.77214
5*5*2	83982	1.19E-05	59.8	5.29E-10	7.77694

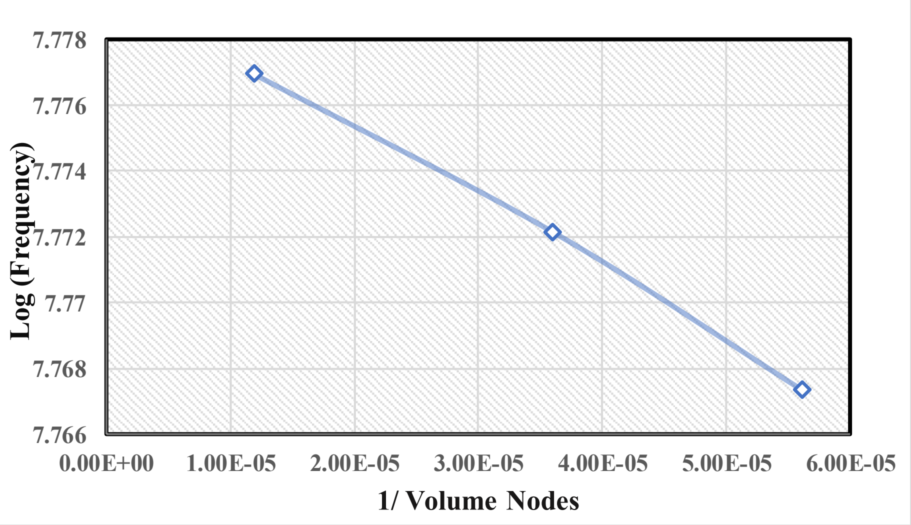

Figure. 3. 10: A mesh convergence study was conducted for the LBAW PiezoMUMPs resonator (RES3_5E_TH) in the 5th mode.

Another mesh convergence study was also performed to determine the appropriate mesh element size for the Mem-Mech simulation. For determining anchor losses and the corresponding Q_f. For this Mem-Mech simulation, linear Manhattan bricks were used to mesh the resonator and the substrate with the same element size. The results of this simulation can be seen in Table.3.8. The used mesh size was 10 μm element size for both the resonator and the one-block substrate size 400x400x400 μm, treated as a single region, along with 50 frequency points. The simulation utilised quiet boundary conditions and symmetry in boundary conditions, as a result, a simulated Q_f value of 2874 was obtained at a resonant frequency (f_r) of 60.367 MHz. This mesh study was conducted as results shown in Figure. 3.11. This resonator intended for thermal tuning, which will be discussed in Chapter 4.

Tether dimensions (T_l x T_w = 20 x 38) μm were chosen to include the connection path for a thermal heating element, which will be used for thermal tuning in the upcoming chapter.

Table.3. 8: Resonant frequency and Q_f values obtained from the mesh convergence study of the designed resonator during anchor losses analysis.

Element size (μm)	**Number of frequency points**	**f_r (MHz)**	**Q_f**
10	50	60.367	2874
	25	60.375	2823
15	50	60.153	2675
	25	60.167	1889
20	50	60.633	1310
	25	60.625	1221

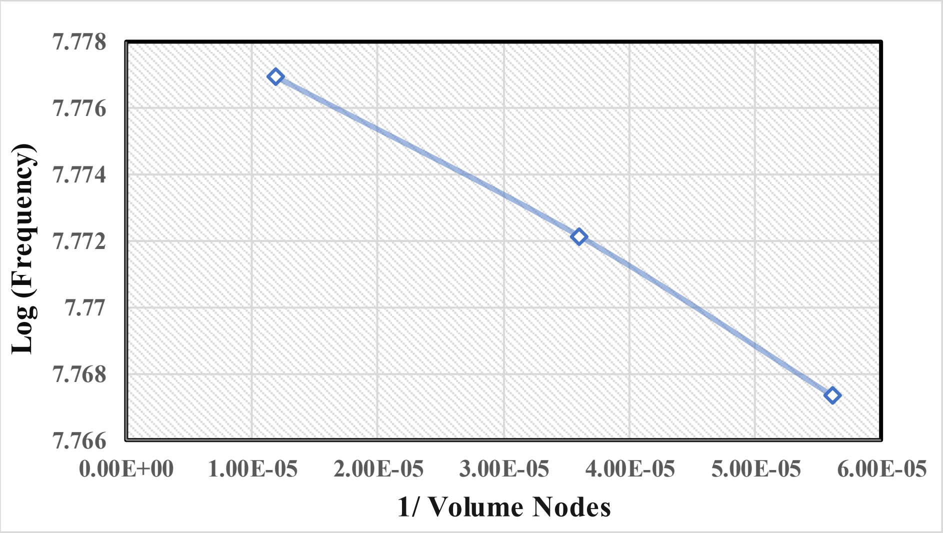

Figure. 3. 11: 5th Mode Mesh Q_f convergence study for LBAW PiezoMUMPs resonator with substrate.

3.5.1 Modal frequency separation versus resonator width variation

The RES2_5E_TH has a thermal element selected from the previous section to be fabricated, characterised, and tested for tuning feasibility. However, it was crucial to analyse the frequency separation of the chosen 5th mode from the adjacent resonant modes. Consequently, for this analysis, the thermal elements were removed to expedite simulation. These results will be referred to as RES3_5E_V1.

Simulations for the resonant frequency f_0 and frequency separation ($f_0 - f_{0-1}$) and ($f_{0+1} - f_0$) have been evaluated using Mem-Mech for different values of resonator width and are shown in Table.3.9. Figure. 3.12 shows the frequency separation of RES3_5E_V1's 5th resonant mode with varying widths measured in µm. Figure 3.13 shows the average frequency separation of the 5th resonant mode applied on RES3_5E_V1. It was evident that the highest modal frequency separation occurs when the resonator width is 275 µm taking account of its Q_f.

Table.3. 9: The 5th mode frequency modal separation versus width variation RES3_5E_V1.

Resonator Width (µm)	f_{0-1} (MHz)	f_0 (MHz)	f_{0+1} (MHz)	$f_0 - (f_{0-1})$ (MHz)	$(f_{0+1}) - f_0$ (MHz)	Average separation (MHz)
50	56.69	57.63	58.55	0.94	0.92	0.93
62.5	62.00	62.43	62.56	0.43	0.13	0.28
75	63.59	64.31	65.02	0.72	0.71	0.71
87.5	62.74	62.94	63.16	0.20	0.22	0.21
100	61.75	61.93	62.22	0.18	0.29	0.23
112.5	61.16	61.30	62.10	0.14	0.80	0.47
125	60.67	60.88	60.93	0.21	0.05	0.13
137.5	59.88	60.23	60.87	0.35	0.64	0.49
150	59.28	59.39	59.72	0.11	0.33	0.22
162.5	62.63	62.64	63.14	0.01	0.50	0.25
175	61.99	62.09	62.48	0.10	0.39	0.24
187.5	61.53	61.72	61.84	0.19	0.12	0.16
200	61.08	61.54	61.67	0.46	0.13	0.30
212.5	60.81	61.14	61.39	0.33	0.25	0.29
225	60.81	60.97	61.30	0.16	0.33	0.24
237.5	60.27	60.58	60.94	0.31	0.36	0.33
250	59.83	60.02	60.31	0.19	0.29	0.24
275	61.30	62.44	62.50	1.14	0.06	0.60
300	61.77	61.98	62.68	0.21	0.70	0.45
325	61.53	61.64	61.89	0.11	0.25	0.18
350	61.11	61.12	61.22	0.01	0.10	0.05
375	62.18	62.21	62.45	0.03	0.24	0.14

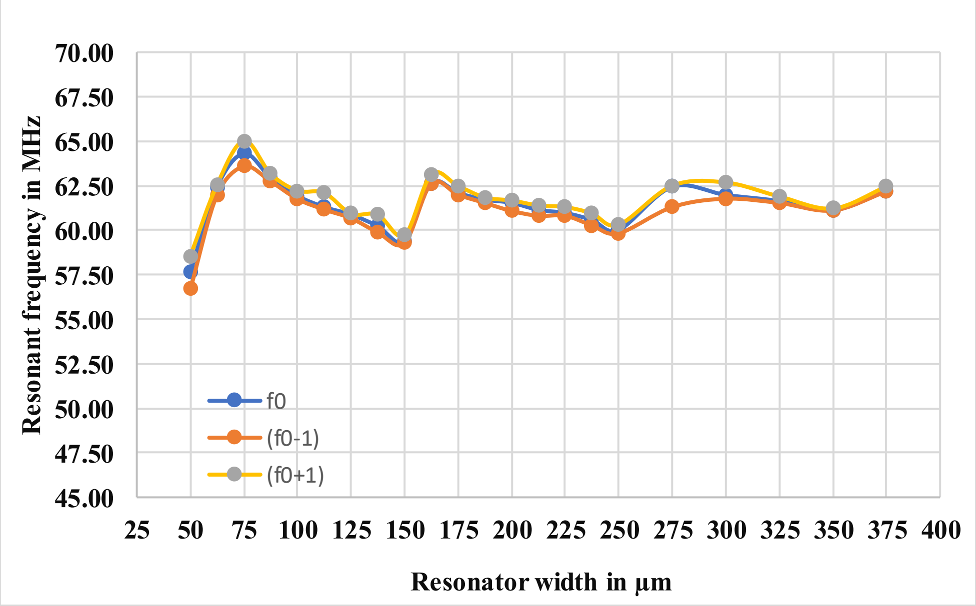

Figure. 3. 12: The frequency separation of RES3_5E_V1's 5th resonant mode with varying widths measured in µm.

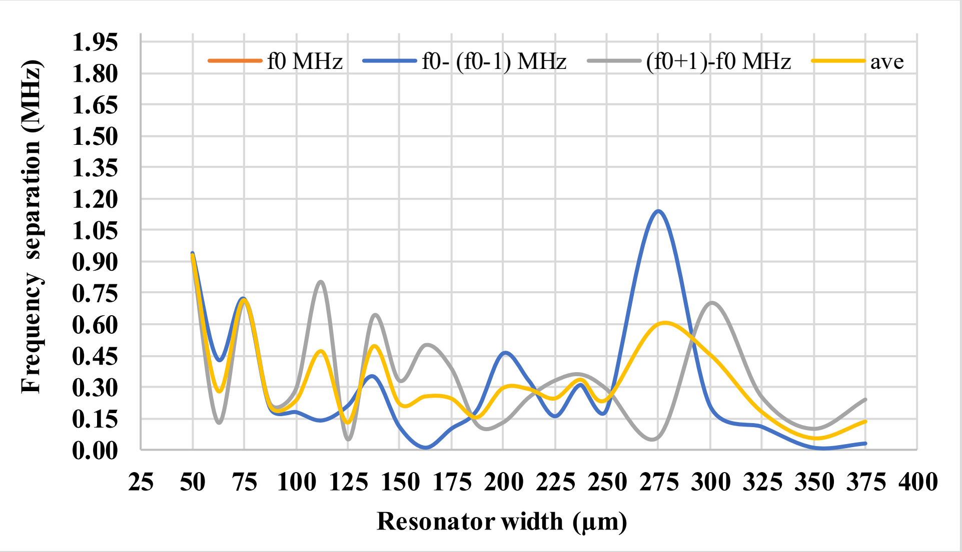

Figure. 3. 13: The average frequency separation frequency of the 5th resonant mode applied on RES3_5E_V1.

3.6 Impact of Resonator Parameter Variations on Q_f

Anchor loss will be the primary focus of this chapter, and it will be investigated with respect to different parameters. One aspect is to explore the effect of the number of electrode elements onthe resonant frequency and its impact on Q_f . Further optimization the resonator quality factor is then carried out by investigating the impact of:

- resonator width;
- resonator's length-to-width ratio.

Finally, the impact of the tether shape and dimension on the quality factor of the resonator operating at 5th resonant mode is also studied.

3.6.1 Effect of Number of Electrode Fingers

To determine the effect of the number of electrode elements on anchor losses, Mem-Mech direct harmonic simulations utilising piezoelectric physics were carried out. Table. 3.10 presents the results for each resonator, all of which have identical size and tether geometry (RES3_5E_V1) (tether (T_l x T_w) = 20 x 38 µm). Among the different configurations with 2, 3, and 5 electrode elements, the resonator design with 2 electrodes displayed a low Q_f on the 5th mode. Furthermore, the 3-electrode configuration showed a quadrupled value of Q_f compared to the 2-electrode configuration, whereas the 5-electrode design exhibited the highest quality factor at the 5th mode.

Table.3.10 indicates that the resonator with five electrode elements exhibits a more significant quality factor than the other two resonators for all three resonant modes.

Table.3. 10: Number of electrode elements effect on resonance frequency and Q_f.

Mech mode f_r	**RES3_2E**		**RES3_3E**		**RES3_5E_V1**	
	MHz	**Q_f**	**MHz**	**Q_f**	**MHz**	**Q_f**
5th	60.8	221	59.39	1094	59.1	3564

3.6.2 Variation in Q_f due to resonator width

This work focuses on the LBAW piezoelectric resonator, in which the resonant frequency equation primarily depends on the resonator body's length (Chapter 2, Section 2.3, Equation 2.6). In this analysis, (Res3_5E_V1) is used to determine the variation of its Q_f with the variation of its width while keeping the resonator length fixed at 350 µm and the tethers (T_l x T_w = 20 x 38) µm. The simulation boundary conditions remain the same as before. A Mem-Mech simulation is run to simulate anchor losses on (RES2_5E_NoTH), as the overall width of the resonator varies between 50 and 350 µm while the tether area remains constant. Piezoelectric physics and direct harmonic analysis are employed for this purpose. Table.3.11 and Figure. 3.14 present the reported resultant Q_f at the resonant frequency. A clear correlation exists between the (variant width / fixed length) W/L ratio of the designed resonator and the value of the anchor losses. The highest quality factor value is achieved when the tether area is 0.87% of the resonator size.

Table.3. 11: Q_f value of RES3_5E_V1 versus width variation.

Resonator's width (µm)	W/L (%)	Q_f	f_r (MHz)
50	0.14	181.5	59
100	28.57	1296	61.9
150	42.86	1056	59.4
200	57.14	1652	61.1
250	71.43	3564	59.1
300	85.71	1618	60.9
350	100	4353	61.9

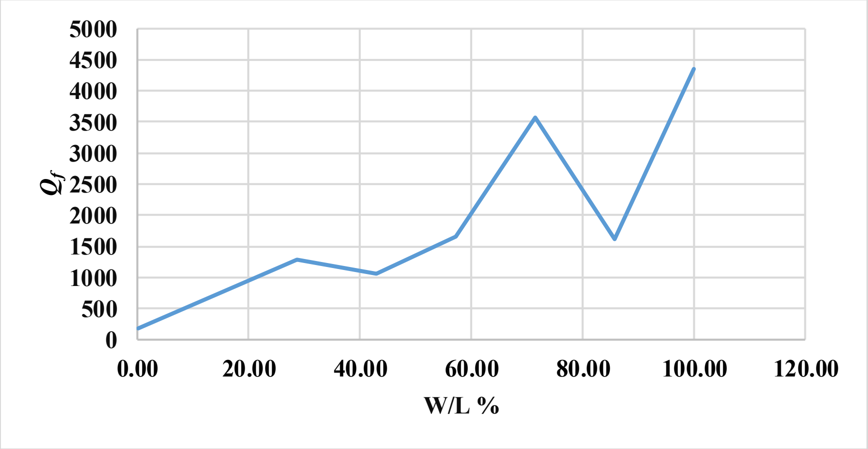

Figure. 3. 14: Comparison between the Q_f value of RES3_5E_V1 at 5th mode versus different resonator's width.

3.6.3 The Variation in The Resonator's Length-to-Width ratio Impact

Following the same procedures as in the previous section on (RES3_5E_V1), change the resonator's length and width to observe how the resonator's area or the percentage of W/L affects the quality factor. Table 3.12 and Figure 3.15 A plot compares the Q_f value under the effect of piezoelectric physics and different resonator width/length ratio in the range of 50–70%.

Table.3. 12: Q_f versus different resonator's (width/ length %) at resonant frequency.

Resonator's L-W (µm)		**W/L %**	**Piezo-physics**	
L	W		Q_f	f_r (MHz)
150	100	66.67	371	140
200	100	50.00	89	107.7
250	100	40.00	643	83.4
250	150	60.00	117	85.7
300	150	50.00	49	73.4
300	250	83.33	173	60.2
350	175	50.00	629	61.9
350	200	57.14	2244	61.7
350	250	71.43	3564	59.1
350	350	100	4353	61.9

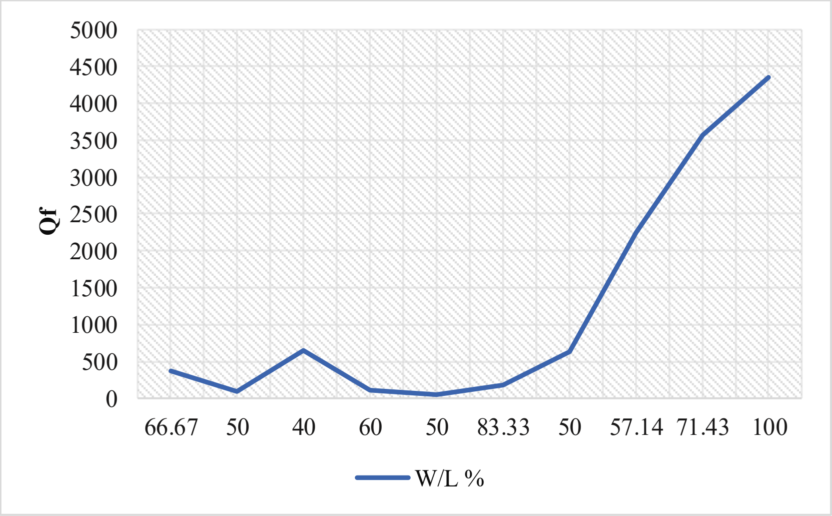

Figure. 3. 15: Comparison between the Q_f value at 5th mode versus different resonator's W/L %.

These results show that anchor losses are significantly affected by the resonator aspect ratio and indicate that optimal Q_f is achieved for aspect ratios close to 100%.

3.6.4 Tether Geometry Variation

The primary pathway for dissipating energy in the resonators is through the tether. This is an important factor as it establishes is the proportional relationship between the Q_f and the length of the tether [60]. Aswell as, the width increases, the surface area of the tether exposed to the surrounding medium also increases, leading to a decrease in Q_f and an increase in energy loss. Conversely, reducing the tether width reduces the surface area and energy dissipation, enhancing energy storage capacity and improving the Q_f [60].

It has already been shown that anchor losses depend on the tether shape connecting the resonator to the anchor point [60]. Therefore, in this study, some of the tethers were curved (radius of 5 µm) at the end corners of the connection point at both the resonator and substrate sides.. The length of each tether—whether curved or not—was varied to allow for mechanical and harmonic simulations of each design. The results demonstrate the effects of implementing curvatures in the tethers and indicate that the length of the resonator affects the quality factor. This study also addresses the limitations associated with excessive curving of resonator tether. Furthermore, the number of LBAW PiezoMUMPs resonators having variant tethers geometry were fabricated and characterized in the following sections, and results were discussed at the end of the chapter.

3.6.4.1 The Optimised LBAW Piezoelectric Resonator

This section compares the simulation results of anchor losses for one resonator, LBAW PiezoMUMPs, that resonates in the 5th mode, including a heating element is referred as Res3_5E_TH. This resonator was the 1st characterised resonator in this study. Anchor loss simulations were run, and results were compared to the characterization outcome. A change of removing the heating element given that the tether width can be at the minimum, considered 22µm instead of 38µm, required by the process fabrication role [7]. This optimised resonator will be referred to as (Res3_5E_V2).

Furthermore, the following will discuss other alterations to the tether's shape that result from adjusting the tether length and curving the contact edges.

Resonator (Res3_5E_V2)

This resonator features a 20 x 22 µm straight tether. Its direct harmonic simulation results indicate that (RES3_5E_V1) is resonating at 58.6 MHz, with a quality factor value of 1168. Figure 3.16 displays the 3D model plot of (RES3_5E_V1)'s mechanical mode results, which indicates that it resonates at 58.8 MHz.

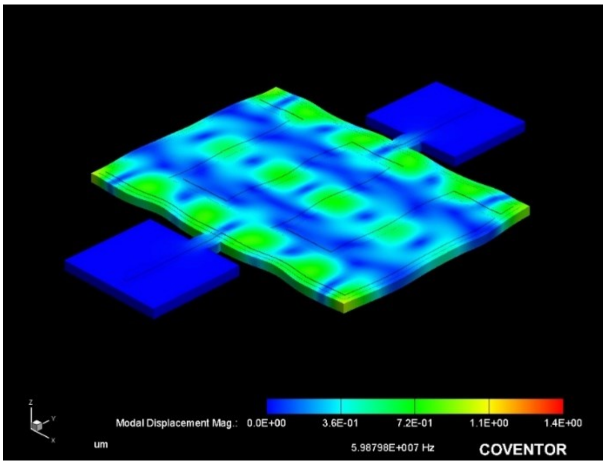

Figure. 3. 16: The 3D model Re (Displacement X) at 5th resonant mechanical mode.

3.6.4.2 Tether Curvature

Applying curvature on both tether contact edges in a resonator will reduce stresses at the contact point. Furthermore, different tether dimensions will affect the resonator's quality factor. Table. 3.11 gives the dimensions of the tether geometry for the different resonators considered, together with the resulting quality factor and resonant frequency.

Resonator (RES3_5E_CT)

The design of this resonator differs from the previous one due to its curved tethers. The 3D model for this resonator can be seen in Figure 3.17, while the 2D layout is provided in Figure 3.18 in GDS file format. This resonator resonates at a mechanical resonance frequency of 61.2 MHz. To simulate its anchor loss with the curved tethers, two distinct mesh types and sizes need to be selected: extruded bricks measuring 5 x 5 x 5 µm for the resonator and Manhattan bricks measuring 10 x 10 x 10 µm for the substrate. Different mesh sizes are necessary due to the curvature of the tethers. Table 3.13 details the modifications made to the tether dimensions to observe their impact on the Q_f value.

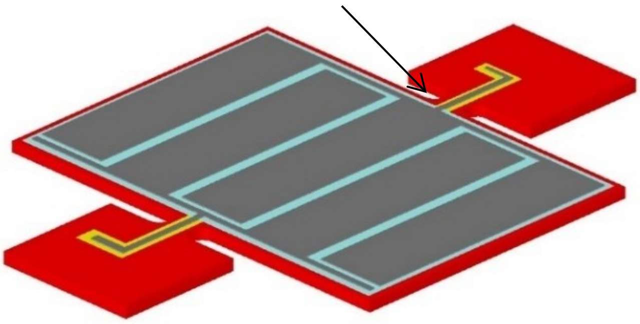

Curved tether

Figure. 3. 17: Five-element electrode LBAW PiezoMUMPs resonator (RES3_5E_CT).

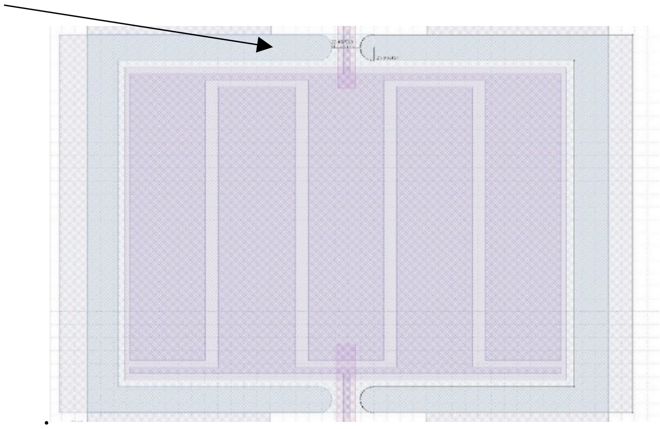

Curved tether

Figure. 3. 18: GDS layout of a five-element electrode LBAW PiezoMUMPs resonator at the 5th resonant mode with curved Tether (RES3_5E_CT).

Table.3.13 displays the simulation results of the relationship between Q_f value under the influence of tether dimension variation for different resonators size. Some of these resonators were chosen to be fabricated for characterisation.

Table.3. 13: Q_f value at 5th resonant mode under the effect of tether geometry variation and resonator's size.

Resonator address	**T_l x T_w (µm)**	**Q_f**	**f_r (MHz)**
Res2_5E_V1	20 x 38	3564	59.1
Res2_5E_V2	20 x 22	1168	58.6
Res2_5E_V3	35 x 22	1250	59.2
Res2_5E_V4	50 x 22	1111	59.1
Res3_5E_V1	20 x 38	627	61.9
Res3_5E_V2	20 x 22	102	61.9
Res3_5E_V3	35 x 22	244	62.2
Res4_5E_V1	20 x 38	4,353	61.7
Res4_5E_V2	20 x 22	896	59.5
Res4_5E_V3	35 x 22	3,102	61.7
Res4_5E_V4	50 x 22	1,562	61.7

3.7 LBAW PiezoMUMPs Resonators Prototype Fabrication

A range of PiezoMUMPs resonators have been fabricated to resonate in LBAW modes and sent for manufacturing. Some of these resonators featured a surface thermal heating element to serve as a thermal element in thermal tuning tests. Once these resonators received, characterisation would be done by applying a potential difference to the drive electrodes to evaluate the piezoelectric layer's coupling coefficient and assess the feasibility of tuning via voltage tuning.

3.7.1 Fabrication Results

As stated in Chapter 2, Section 2.8.1, designing any designed PiezoMUMPs resonator using the CoventorWare 3D builder depends on the involvement of three separate files: the material, layout, and process files. Typically, the software package includes material and process files; however, for PiezoMUMPs technology, the process file was not provided. As a result, the process file was prepared with the general process descriptions and user guide [7]. Figure. 3.19 shows one of the designed resonators RES2_2E_TH which includes a thermal element for tuning purposes, sending the exported layout file as a .gds, as shown in Figure. 3.20, all resonators were designed and sent to MEMSCAP for manufacturing. These resonators were initially designed, and their trenches were positioned with a minimal tolerance using the SOI mask. All these prototypes were received from MEMSCAP in an unreleased state. Figure. 3.21 displays a micrograph of the same resonator, illustrating the size of the TRENCH and how it ended up being smaller than anticipated. This issue resulted from minimal TRENCH dimensions and process variances in the associated side wall angles (Chapter2, Section 2.8.1.1, Figure. 2.19).

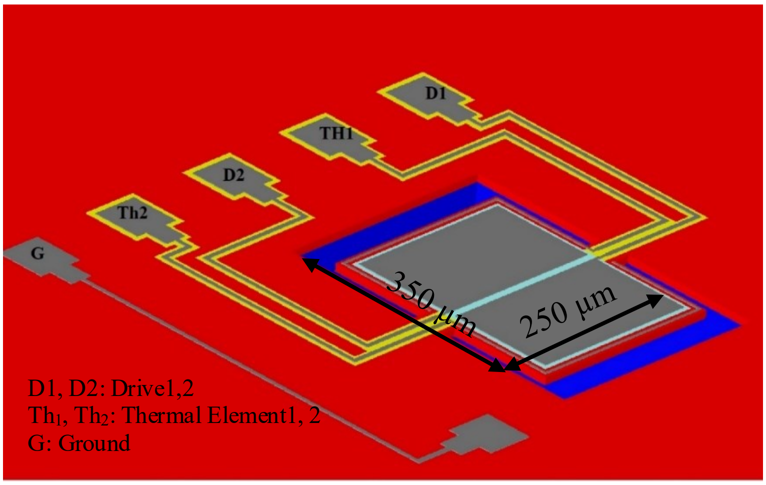

Figure. 3. 19: RES2_2E_Th, LBAWPiezoMUMPs resonator including thermal elements.

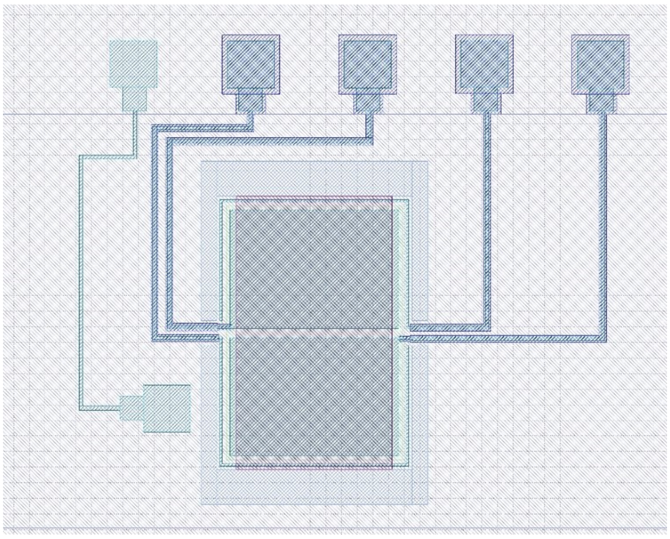

Figure. 3. 20: A GDS layout of 2E_elctorods PiezoMUMPs resonator including thermal elements.

To ensure full resonator release, even in the case of a significant process variation, a second fabrication run was carried out with the trench dimensions increased by 35 µm in both x and y directions.

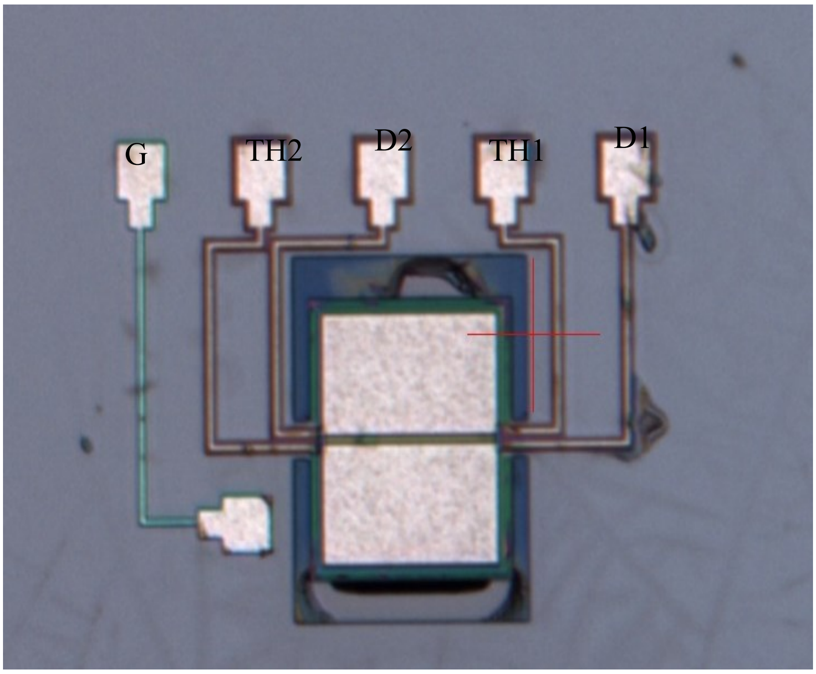

Figure. 3. 21: Micrograph of two ports PiezoMUMPs resonators, including thermal elements.

Various printed circuit boards (PCBs) were created and produced for testing the prototypes, specifically for voltage and thermal tuning characterization. Figure. 3.22 showcases one of these PCBs. These PCB boards were designed to mount the manufactured MEMS die and by attaching SMA pins to the board to contact the bounded resonators within the die. Some resonators were intentionally left unbounded to allow probing using micro-needles.

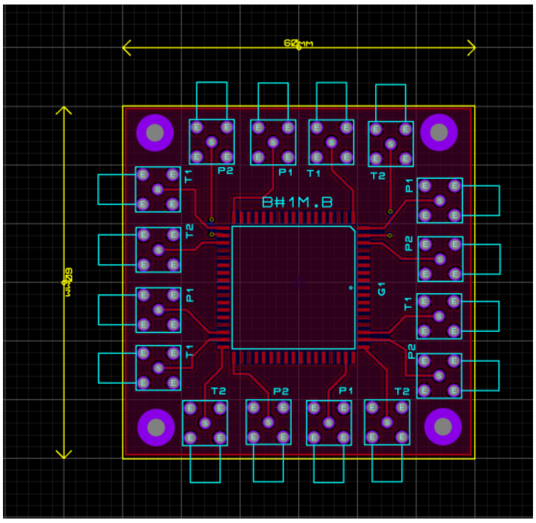

Figure. 3. 22: Fabricated PCB layouts.

3.7.2 Characterisations of LBAW PiezoMUMPs Resonators

After receiving the second set of resonators for fabrication it was possible to characterise the resonators after it was verified that all resonator structures had been released. This section includes the primary characterisation and experimental validation of tuning procedures used on the AlN-based MEMS resonators.

Because the resonator's size is in the micron range and its vibration amplitude when in operation is only tens of nanometres, it is crucial to account for the presence of dust in the air, variations in the surrounding temperature, and humidity during characterisation. The scattering parameters of the resonators at different frequencies were measured using a pocket vector network analyser.

3.7.2.1 Characterisation Results for Different Electrode Element Numbers

The transmission parameter, which measures transmitted waves from the input port to the output port (S_{21}) in decibels, is used to examine the transmission characteristics. It is written as [120]:

$$S_{21}(dB)=10\ \log10\ \left(\frac{P_0}{P_i}\right) \tag{3.9}$$

where P_0 is output power, and P_i is input power.

The test allows for the direct determination of the resonator's centre frequency (f_r) and insertion loss (IL), as well as the loaded anchor quality factor (Q_f), which is obtained by computing the 3*dB* bandwidth provided by the following relation [120]:

$$Q_f = \frac{f_r}{\Delta f_{-3dB}} \tag{3.10}$$

where Δf is the 3*dB* bandwidth.

Several tests were conducted on the fabricated resonators to check the resonant frequency, at the 5th resonant mode, 2E, 3E, and the 5E electrode element number, was used. Table.3.14 shows the fabricated resonators' quality factors for these resonators at the 5th resonant mode. Figure. 3.23 and Figure. 3.24 show the micro-photo of the fabricated LBAW PiezoMUMPs resonators (a) 2, (b)3E, and (c) 5E electrode elements and their measured S_{21} (*dB*) transmission response respectively.

Table.3. 14: Characterisation results obtained for three LBAW PiezoMUMPs resonators having different number of electrode elements: (a) 2-element, (b) 3-element, and (c) 5-element electrode versions.

Resonator Model	**RES3_2E**		**RES3_3E**		**RES3_5E_V1**	
Q_f at resonance, Resonant frequency f_r	Q_f	f_r (MHz)	Q_f	f_r (MHz)	Q_f	f_r (MHz)
	1019	52.01	712	56.9	1250	57.2

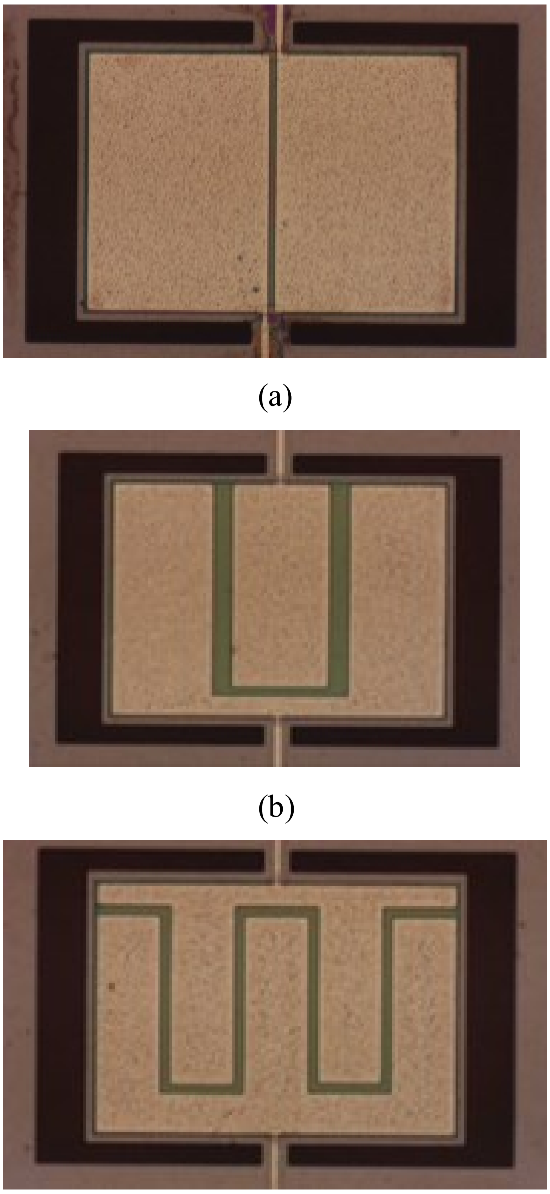

(a)

(b)

(c)

Figure. 3. 23: Micro-photo of the fabricated LBAW PiezoMUMPs resonators
(a) 2-element, (b) 3-element, and (c) 5-element electrode versions.

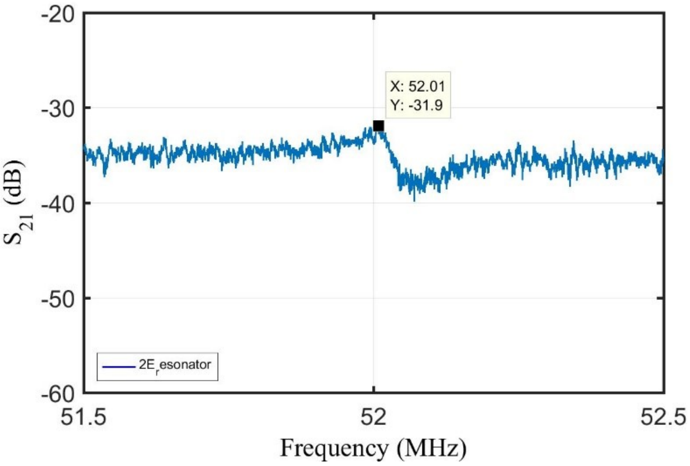

(a)

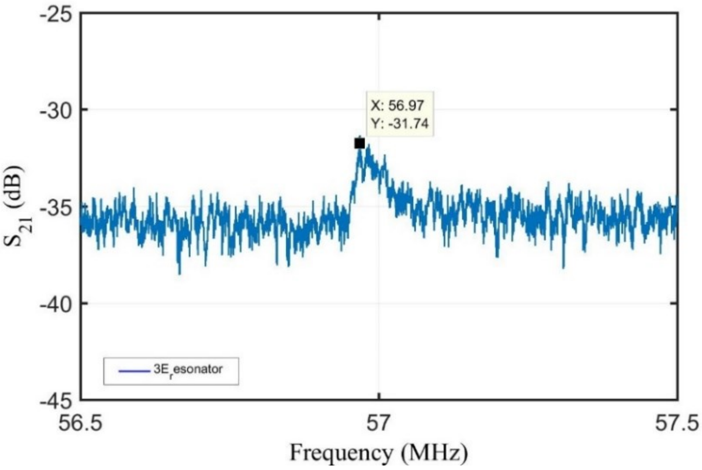

(b)

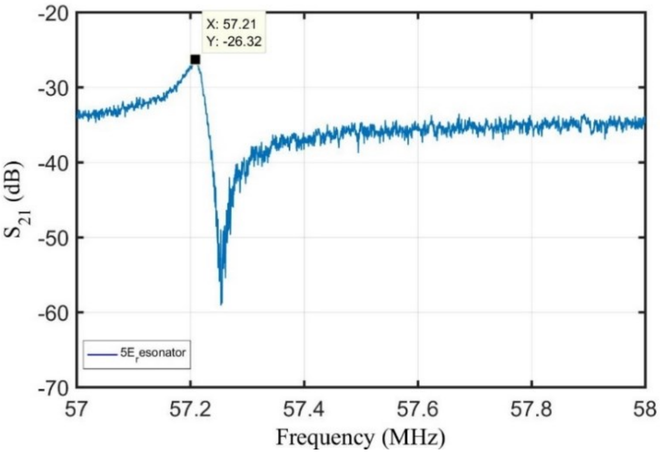

(c)

Figure. 3. 24: Measurement of S_{21} transmission parameter for the fabricated LBAW PiezoMUMPs resonators (a) 2-element, (b) 3-element, and (c) 5-element electrode versions.

The characterization results have demonstrated that the 5-element electrode resonator possesses the highest quality factor, making it the most suitable candidate for additional characterizations and tuning investigations at the fifth resonant mode.

3.7.2.2 Characterisation Results for 5E_Resonator / Different Resonator Tethers

In this section, the characterisation data of seven manufactured LBAW PiezoMUMPs resonators that resonate in the 5th mode are shown, explained, compared, and discussed in detail. These seven resonators differ regarding tether dimensions, shape, and resonator geometry.

i) RES2_5E_TH

This was the 1st fabricated resonator; a thermal element was included in the structure to test the feasibility of thermal tuning. The following chapter will cover this resonator in more detail. The micro-photo of the fabricated RES2_5E_TH and its measured S_{21} (dB) transmission parameter are displayed in Figure. 3.25, this resonator has a resonant frequency at 61.4 MHz, with a quality factor value of 3,067. In Chapter4, this resonator will be used in thermal ovenisation and voltage tuning investigations.

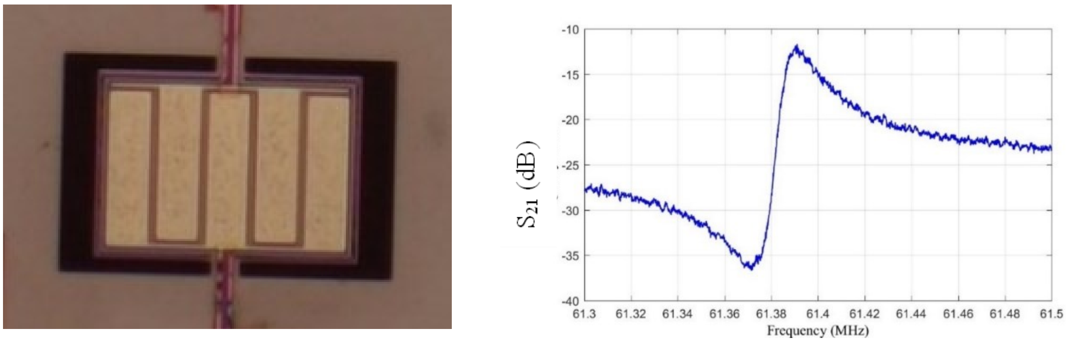

(a) (b)

Figure. 3. 25: Micro-photo of the fabricated RES2_5E_TH and its measurement of S_{21} transmission parameter.

ii) RES3_5E_V2

This resonator has the same geometry as RES2_5E_TH and a straight tether with dimensions of 20 x 22 µm. The thermal element was not included, and the tether width is the minimum for the process fabrication role [7].

The micro-photo of the manufactured RES3_5E_V2 and its measured S_{21} (dB) transmission parameter are displayed in Figure 3.26, as it is shown that it resonates at 57.2 MHz with a quality factor value of 1,683.

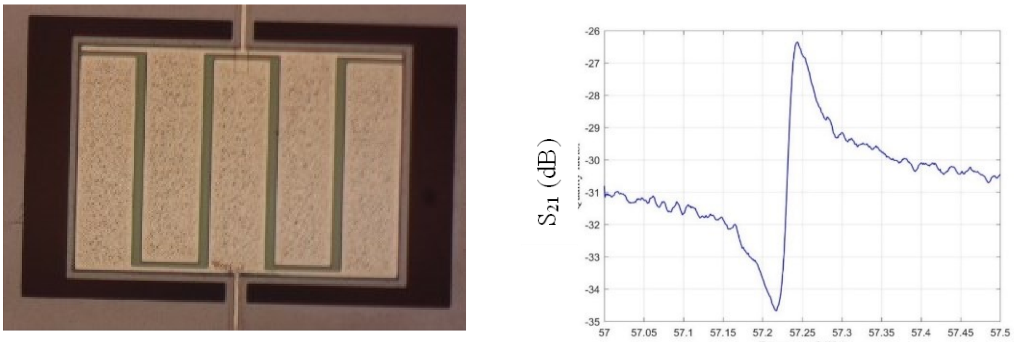

(a)

(b)

Figure. 3. 26: Micro-photo of the fabricated RES3_5E_V2 and its measurement of S_{21} transmission parameter.

iii) RES3_5E_CT

This resonator is the same as RES3_5E_V2, except it has a curved tether. The micro-photo of the fabricated RES3_5E_CT and its measured S_{21} (dB) transmission parameter are displayed in Figure. 3.27, this resonator resonates at 60.9 MHz, with a quality factor value of 1,518, and it will be characterised in electrothermal tuning experiment discussed in Chapter 4, section 4.3.2.1.2.

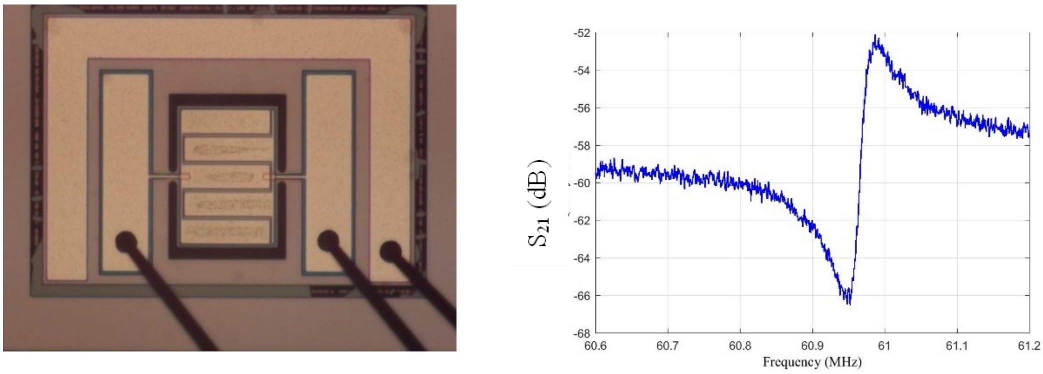

(a)

(b)

Figure. 3. 27:Micro-photo of the fabricated RES3_5E_CT and its measurement of S_{21} transmission parameter.

iv) RES3_5E_V3 _CT

This resonator has a curved tether with dimensions of 35 x 22 μm. Its micro-photo and measured S_{21} (dB) transmission parameter are displayed in Figure. 3.28, which shows that it resonates at 60.9 MHz with a quality factor value of 911.

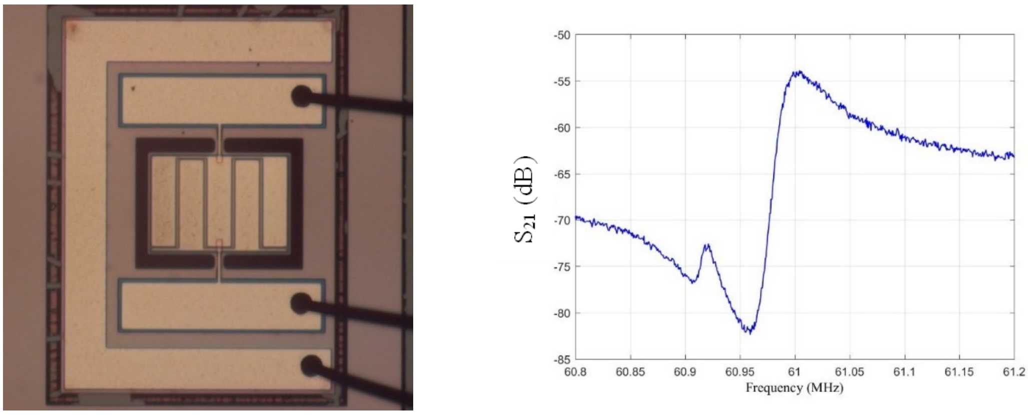

(a)

(b)

Figure. 3. 28: Micro-photo of the fabricated RES3_5E_V3 _CT and its measurement of S_{21} transmission parameter.

v) RES3_5E_V4_CT

This resonator has a curved tether with dimensions of 50 x 22 μm. Its micro-photo and measured S_{21} (dB) transmission parameter are displayed in Figure. 3.29, this resonator resonates at 60.9 MHz with a quality factor value of 887.

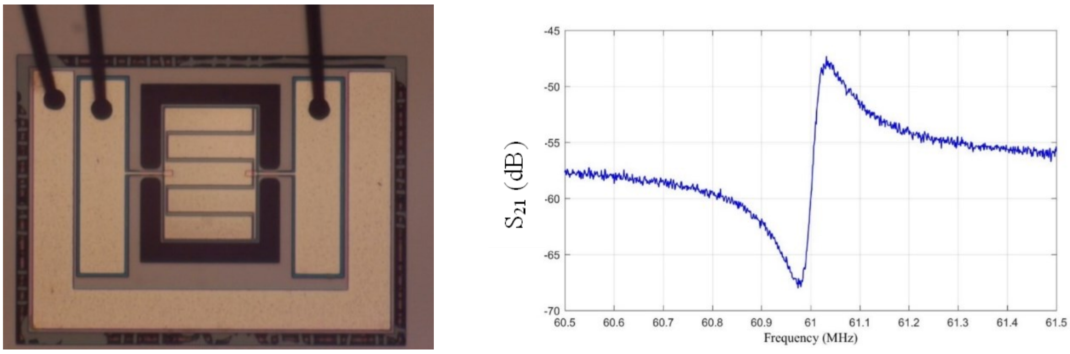

(a) (b)

Figure. 3. 29: Micro-photo of the fabricated RES3_5E_V4 and its measurement of S_{21} transmission parameter.

vi) RES4_5E_V3 _CT

This resonator has a different geometry, measuring 350 x 175 µm and a curved tether measuring 35 x 22 µm. Figure. 3.30 shows a micro-photo of the fabricated RES4_5E_V3 _CT and its measured S_{21} (dB) transmission parameter. This resonator resonates at 60.7 MHz and has a quality factor value of 225.

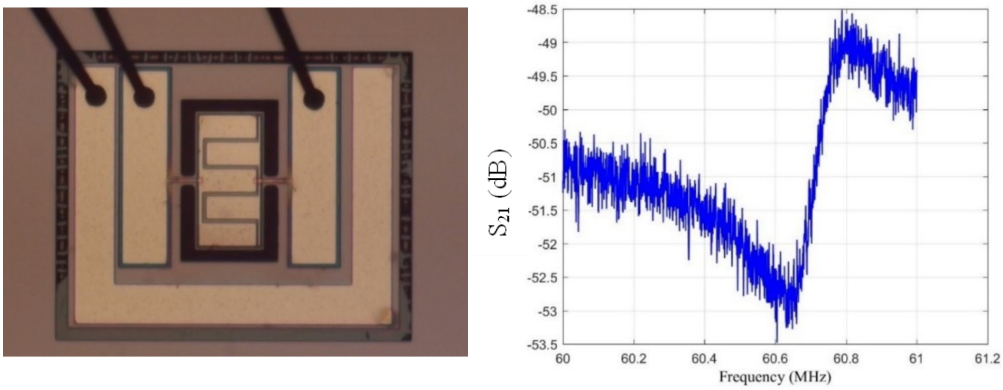

(a) (b)

Figure. 3. 30: Micro-photo of the fabricated RES4_5E_V3 and its measurement of S_{21} transmission parameter.

vii) RES5_5E_V3_CT

This resonator is square-shaped; it measures 350 x 375 µm and has a curved tether that measures 35 x 22 µm. Figure. 3.31 shows a micro-photo of the fabricated RES5_5E_V3_CT and its measured S_{21} (dB) transmission parameter. This resonator resonates at 60.9 MHz and has a quality factor value of 1,563.

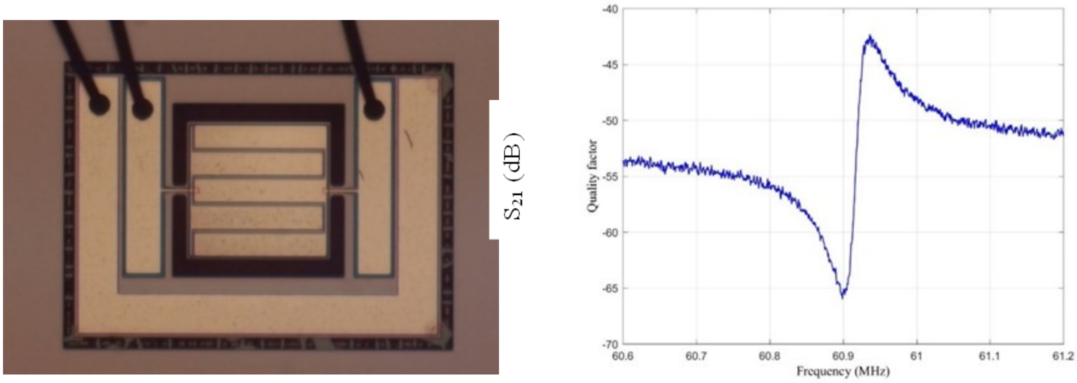

(a) (b)

Figure. 3. 31: Micro-photo of the fabricated RES5_5E_V3_CT and Measurement of S_{21} transmission parameter.

3.7.3 Discussion

The previous sections presented a detailed analysis, definition, and comparison of the simulation and characterisation data of six fabricated LBAW PiezoMUMPs resonators resonating in the 5th mode. These six resonators differ in terms of their tether dimensions, structure, and resonator geometry.

Table.3.15 displays the resonant frequency and quality factor for the LBAW PiezoMUMPs resonators with varying tether dimensions and shapes at their 5th resonant mode. The RES2_5E_TH, with its heating element included, is the best option for thermal-voltage tuning experiments, which will be discussed in detail in Chapter 4.

Even with a 5µm diameter curvature at each linked point, the other resonators did not perform with the same high-quality factor as RES2_5E_TH. Because of this, the 20 x 22 µm was significantly shorter in length than RES2_5E_TH. While the quality factor for RES3_5E_V3 _CT and RES3_5E_V4_CT did not improve when the tether length was extended to 35 µm, there was a noticeable improvement when the resonator's size took a square shape. This indicates that the tether's length, shape, and the resonator's size are significant.

Table.3. 15: The 5th resonant mode for different LBAW PiezoMUMPs resonators having diverse tether geometry including their Q_f.

Resonator No	**Resonator Dimension (µm)**	**Tether Dimension (µm)**	**Straight / Curved Tether**	Q_f	f_r **(MHz)**
RES2_5E_TH	350 x 250	20 x 38	Straight	3067	61.4
RES3_5E_V2		20 x 22	Straight	1683	57.2
RES3_5E_CT		20 x 22	Curved	1362	60.9
RES3_5E_V3 _CT		35 x 22	Curved	911	60.9
RES3_5E_V4_CT		50 x 22	Curved	887	60.9
RES4_5E_V3_CT	350 x 175	35 x 22	Curved	225	60.7
RES5_5E_V3_CT	350 x 350	35 x 22	Curved	1563	60.9

4. Tunability Techniques for LBAW PiezoMUMPs Resonators

This chapter studies the feasibility of Piezoelectric MEMS lateral bulk acoustic wave resonators based on the PiezoMUMPs technology [120], where both theoretical analysis and primary simulations results are presented including temperature effects on resonant frequency: results of this work enable the possibility of fine tuning, which can be applied to high precision timing circuits such as frequency counters. Furthermore, results of validating experimentally the effect of thermal and voltage tuning on PiezoMUMPs resonators are also explained.

Two types of TPoS MEMS resonators were studied and designed and both were actuated using two different types of piezoelectric materials, the PZT and AlN, these two resonators were modelled and simulated using ConvenorWare tool kit, and both resonated in the (LBAW). Both the PZT-based MEMS (PZTMEMS) and the AlN-based PiezoMUMPs processes have been considered in this study, with modified designs based on the design investigated in [3]. Resonator parameters such as resonant frequency, quality factor and temperature variation effect (273-573 K) have been evaluated using finite element methods (FEM) techniques.

The temperature effect on the resonant frequency has also been evaluated analytically and results were compared to those derived from FEM, and the operation of the resonators has been investigated when operating in the first and third lateral resonance LBAW modes. Since it is very important to have low insertion losses, and a high-quality factor, the effect of temperature variation on the optimum quality factor was also investigated. Various prototypes were submitted for fabrication utilizing the PiezoMUMPs process, incorporating an integrated metal heating component to evaluate the feasibility of thermal tuning for these resonators. The initial fabrication attempt was unsuccessful, attributed to a lack of experience in design refinement (trench dimensions being precisely on the edge, necessitating enlargement to ensure resonator release). Consequently, the second fabrication was executed flawlessly to analyse the designated LBAW PiezoMUMPs (RES3_5E_TH), resonating at the 5th mode with the thermal element included. Subsequently, this resonator was characterized, and thermal tuning trials were conducted. Thermal tuning and analytical results were compared and results were discussed including voltage testing and simulation results [121].

The experimental attempt to achieve electric heating via a U-shaped heating element proved to be unsuccessful. The body of the resonator was then heated using a different heating technique that involved passing current through the SOI layer via two metal electrodes on either side of the resonator. The results were recorded and discussed in the following parts.

4.1 Theory and Analytical results on LBAW PiezoMUMPsResonators

This section outlines the theoretical analysis of how temperature change affects the LBAW PiezoMUMPs resonator's material properties and, consequently, how that affects the resonant frequency. The findings of this study were reported in [121] and compared with to simulation results.

4.1.1 Material Property and Temperature Effect

To comprehend how temperature variations affect the resonant frequency of resonators, the mechanical properties of MEMS devices are explained by an analysis of thermal variation of the material properties namely, density, Young's modulus, and device dimension. As shown in [122], these characteristics together define how the MEMS device reacts to temperature variations.

$$E(T) = E_0 - BTe^{-T_0/T} \tag{4.1}$$

where E_0 is the Young's modulus at 0 K while $B > 0$ and $T_0 > 0$ are temperature independent constants, the theoretical studies and measurements have also been performed on silicon cantilevers under the effect of range of temperature variation through their length, showing that the density of silicon ρ is inversely proportional to $(1 + \alpha\Delta T)^3$, and geometrical variations in the thickness t and the length L will also take place due to thermal expansion and these are proportional to $(1 + \alpha\Delta T)$ [123,124], where α is the thermal expansion coefficient of the material. In lateral mode only the length L is considered in the equation.

Therefore, the density and length variations with temperature can be modelled by:

$$\rho(T) = \frac{\rho_0}{(1 + \alpha(T - T_0))^3} \tag{4.2}$$

$$L(T) = L_0(1 + \alpha(T - T_0)) \tag{4.3}$$

4.1.2 Analytical Results

The resonant frequency changes due to temperature variation considering variations in the geometry, density and Young's modulus can be expressed as:

$$\frac{\partial f}{\partial T} = \left(\frac{\partial f}{\partial L}.\frac{\partial L}{\partial T}\right) + \left(\frac{\partial f}{\partial E}.\frac{\partial E}{\partial T}\right) + \left(\frac{\partial f}{\partial \rho}.\frac{\partial \rho}{\partial T}\right) \tag{4.4}$$

Where $\frac{\partial f}{\partial T}$ is the partial differential equation (4.1), considering the resonant frequency variation with temperature including the effect on the resonator's material property. In order to analytically derive the variation of resonant frequency with temperature in the range of 273 - 573 K, equations (4.1-4.4) have been used. Values of E_0 = 167.5 GPa, ρ_0 = 2.330 x 10^3 kg/m^3, B = 15.8 MPa/K, and T_0 = 317 K for silicon [119,120].

$$\frac{\partial f}{\partial E} = \frac{1}{2}.L(T)^{-1}.E(T)^{-1/2}\ .\ \rho(T)^{-1/2} \tag{4.5}$$

$$\frac{\partial f}{\partial \rho} = -\frac{1}{2}\ L(T)^{-1}.E(T)^{\frac{1}{2}}.\rho(T)^{-3/2} \tag{4.6}$$

$$\frac{\partial f}{\partial L} = -\ L(T)^{-2}.E(T)^{\frac{1}{2}}.\rho(T)^{1/2} \tag{4.7}$$

$$\frac{\partial E(T)}{\partial t} = -E_0.e^{-T_0/T}.\frac{-T_0}{T_2} \tag{4.8}$$

$$\frac{\partial \rho\ (T)}{\partial T} = -3.\rho(T_0).\left(1 + \alpha(T - T_0)\right)^{-4}.\alpha \tag{4.9}$$

$$\frac{\partial L(T)}{\partial t} = \alpha . L_0 \tag{4.10}$$

Substituting equations 4.6 – 4.11 in equation 4.5, will result in:

$$\frac{\partial f}{\partial T} = \frac{\alpha . \left[\left(\frac{E_0 . T_0}{\alpha . T} . e^{\frac{-T_0}{T}} \right) + \left(\frac{3\rho(T_0). E(T)}{\rho(T).(1 + \alpha(T - T_0))^4} \right) - L_0 . L(T). E(T) \right]}{2L(t)\sqrt{E(T).\rho(T)}} \tag{4.11}$$

Figure. 4.1 shows the variation of silicon's Young's modulus with temperature increase. This relationship is almost linear and can be approximately modelled by this equation:

$$E(T) = 169{,}760 - 12.919\,T \tag{4.12}$$

This equation will eventually be used for the finite element modelling.

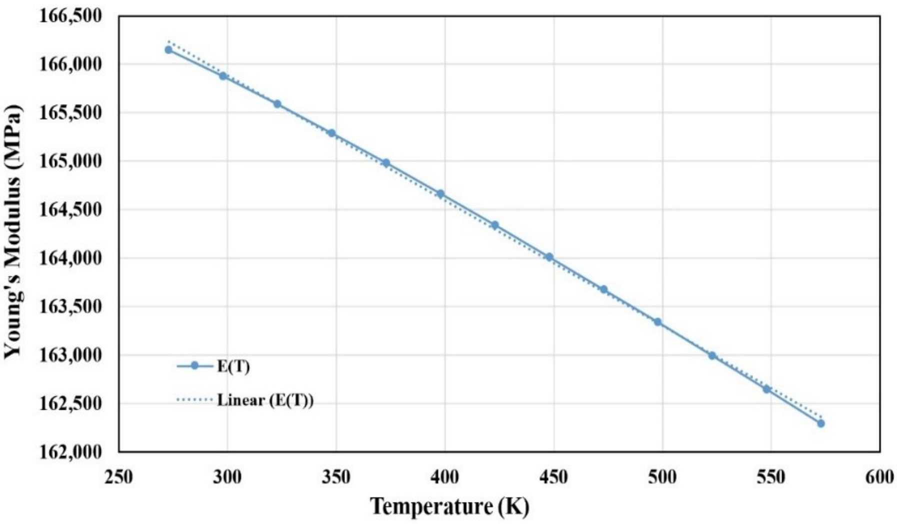

Figure. 4. 1: Almost linear decrease in silicon's Young's modulus with increase in temperature.

The analytically derived variation of the resonant with temperature led to equation 4.12, with a correction coefficient to calibrate the model to the FEM results ($K_c = 1$), is shown in Figure. 4.2.

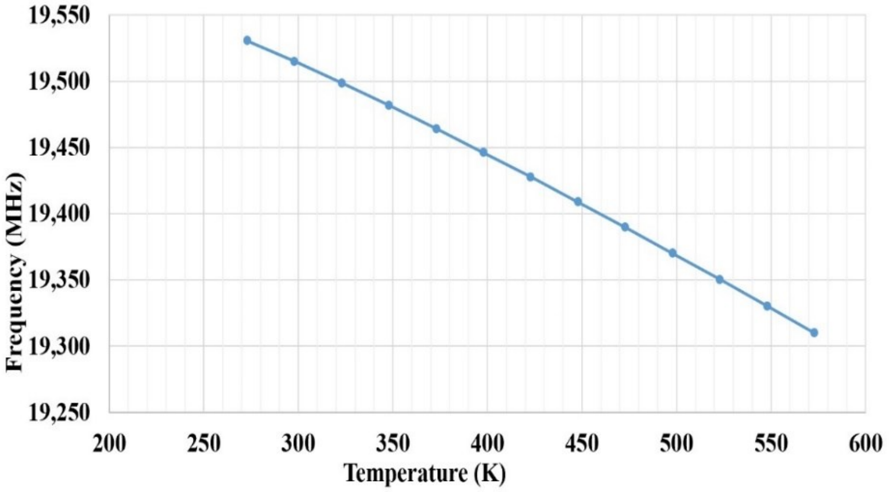

Figure. 4. 2: Analytically derived 1st mode resonant frequency variation with Temperature Constant coefficient (Kc =1).

4.2 Temperature Variation Effect on SOI Layer Using FEM

The effect of temperature variation from 273- 573 K for the two different SOI thickness 10 µm for PiezoMUMPs and 5.5 µm for PZTMEMS was first assessed considering only the SOI layer. Using the linear approximation of Young's modulus value of silicon based on section 4.1.2, the temperature variation was evaluated by applying a T-fixed boundary condition on the SOI layer. The next section presents a comparison between the analytical and the FEM results obtained for the PiezoMUMPs resonator considering the SOI only.

4.2.1 Analytical and FEM Simulations Results Comparison

A temperature range of 273 – 573 K was applied when simulating both the PiezoMUMPs and the PZTMEMS resonators considering the SOI layer only, and results for first mode resonant frequency are compared to the previous analytical one.

Figure. 4.5 shows the gradual linear decrease in resonant frequency with temperature increase, for both the analytical and FEM results for both resonators. Using the empirically derived correction factors for both designs, the resonant frequencies determined by the analytical and FEM techniques were made to be equal at a reference temperature of T = 323 K The correction factors K_{c1} and K_{c2} were found to be 1.005 and 1.015 for the PZTMEMS and PiezoMUMPs processes respectively, when only SOI layer was included. A comparison of these results is shown in Figure.4.5. It is evident that with the introduced correction factors, both the analytical and FEM results track each other over a wide temperature range, indicating that the temperature effect on resonant frequency can be accurately evaluated using the calibrated analytical equation.

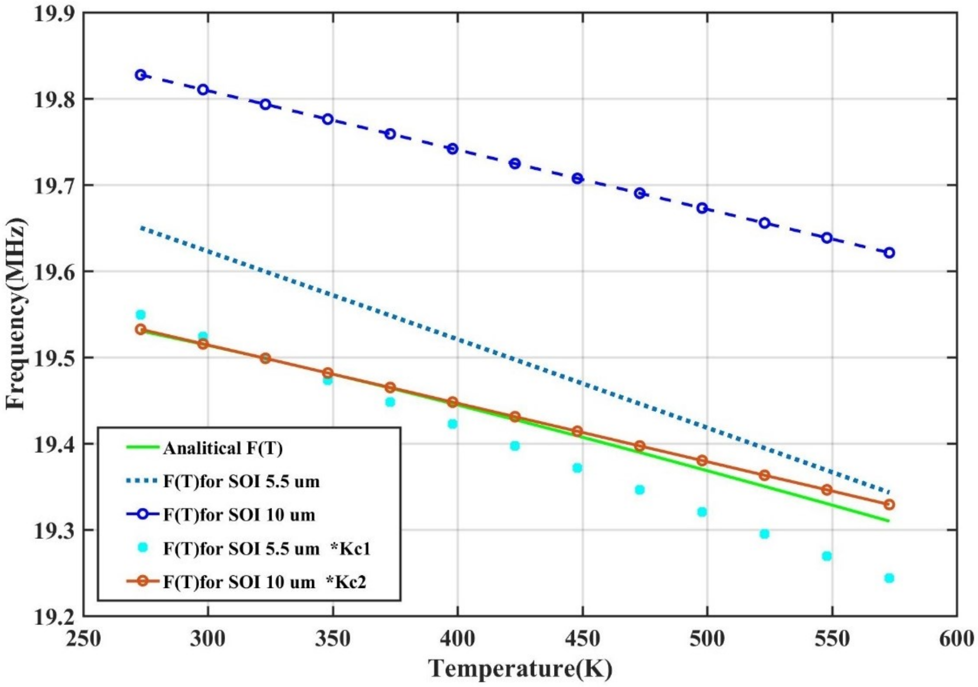

Figure. 4. 3: Comparison between FE and analytical results for the resonant frequency versus temperature.

4.2.2 Temperature Variation Effect on PZTMEMS and PiezoMUMPs Resonators

To have more precise FEM analysis results for both the PZTMEMS and PiezoMUMPs resonators, simulations were carried out including all material layers over a temperature change of 273 - 573 K. A comparison of the FEM results when only the SOI layer is included and when all layers are included was carried out and the results are shown in Figure. 4.6 and Figure. 4.7 for the PZTMEMS and the PiezoMUMPs process respectively. In PZTMEMS first mode resonant frequency, a difference of almost 3 MHz between the corresponding FEM results can be noticed. However, in the case of the PiezoMUMPs process, the corresponding FEM results are much closer. This can be explained by the fact that the ratio of the SOI to Piezo layer thickness in the case of the PiezoMUMPs process is 20 while that of the PZTMEMS process is 5.5 µm. This means that the piezoelectric film in the PZTMEMS process has more effect on the resulting resonant frequency and cannot be ignored in the final FEM simulations.

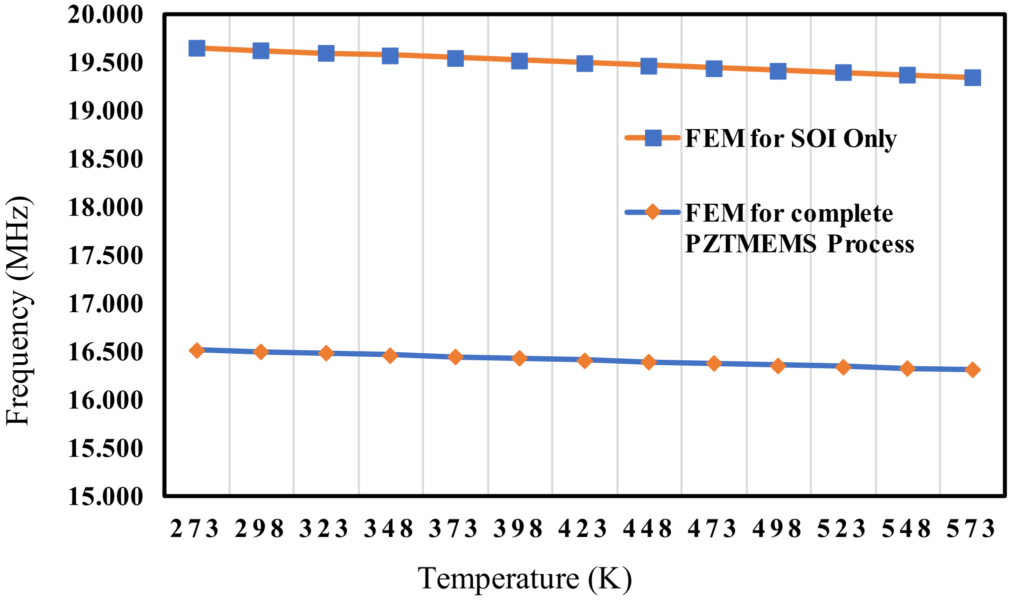

Figure. 4. 4: Comparison of the 1st mode resonant frequency versus temperature change for the PZTMEMS when only the SOI layer is included and when all layers are included.

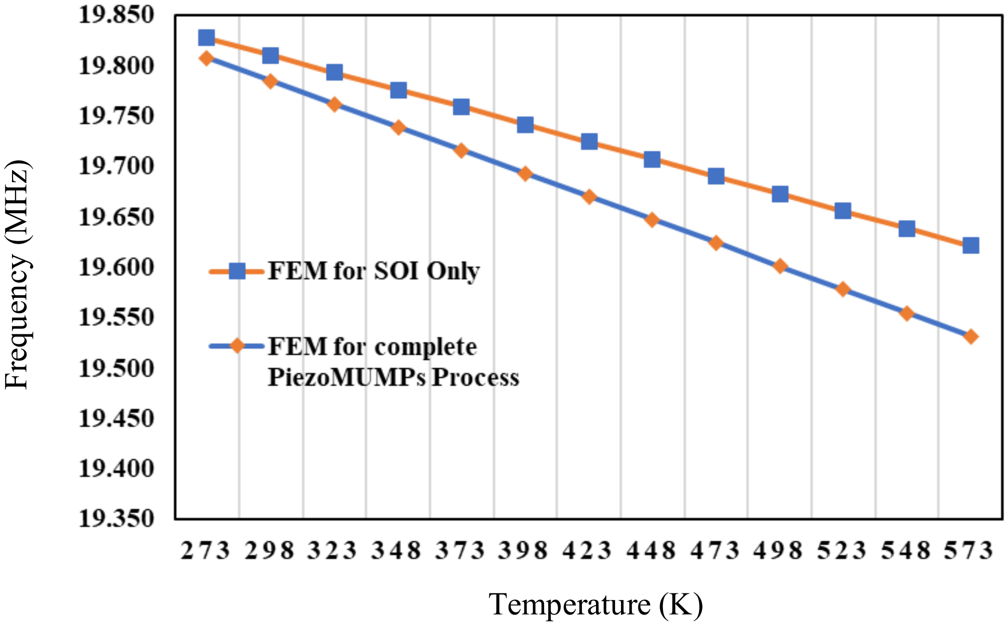

Figure. 4. 5: Comparison of the 1st mode resonant frequency versus temperature change for the PiezoMUMPs when only the SOI layer is included and when all layers are included.

4.2.3 Quality Factor

Total quality factor can be approximately determined via the total loss of air damping (Q_{AIR}), thermo-elastic effects (Q_{TED}), anchor losses (Q_{ANCHOR}) and other electrical and intrinsic material losses, as equation no. 2.14 listed in Chapter 2, section 2.5.1.1. It has already been shown in previous work that TPoS MEMS resonators are less sensitive to air damping losses, and the magnitude of Q_{TED} decreases with temperature. Anchor losses have a significant effect compared to thermo-elastic losses (at room temperature) and air damping losses [3]. In this case only anchor losses were investigated for both the designed resonators. Over a temperature range of 273 - 573 K, anchor loss simulation results show that the PZTMEMS process has a significantly higher quality factor than the PiezoMUMPs at the third mode resonant frequency. The corresponding values for Q_{Anchor} simulated at 273 K are 1,800 and 300 for PZTMEMS and PiezoMUMPs respectively. The change in the quality factor over the considered temperature range is relatively small and it was found to be 1.03% for PZTMEMS and 2.18% for PiezoMUMPs. This means that fine thermal tuning of the resonators can be carried without significantly affecting the quality factor.

4.3 Design and Simulation of the 5th order PiezoMUMPs resonator

CoventorWare FEM simulations were carried out to predetermine the resonant frequency as well as to assess thermal and voltage tunability, following a mesh convergence study based on modal analysis, a mesh element volumetric size of 5 x 5 x 2 µm was deduced as was discussed in Chapter 3, Sec 3.5. Figure. 3.9. Fine frequency tuning can be achieved using thermal and voltage tuning and the temperature dependent frequency shift has already been investigated in micro-ovenised aluminium nitride (AlN) lateral contour-mode MEMS resonators [12]. Based on the same idea, using the PiezoMUMPs technology, a heater element has been integrated in the body of the resonator for SOI surface heating. Figure. 4.3 shows a simplified schematic of the proposed design (RES2_5E_TH), where this resonator is composed of a 10 µm thickness of single-crystalline silicon SOI rectangular structure acting as the lateral bulk acoustic resonator. The resonator and tether dimensions are 250 x 350 µm and 20 x 38 µm, respectively, and the 0.5 µm thick Piezoelectric AlN layer has a dimension of 230 x 330 µm. This resonator consists of two interdigitated electrodes and an integrated thermal heating element of width 5 µm, as shown in Figure. 4.3 The electrode shape has been chosen to support the 5th order lateral contour mode [121].

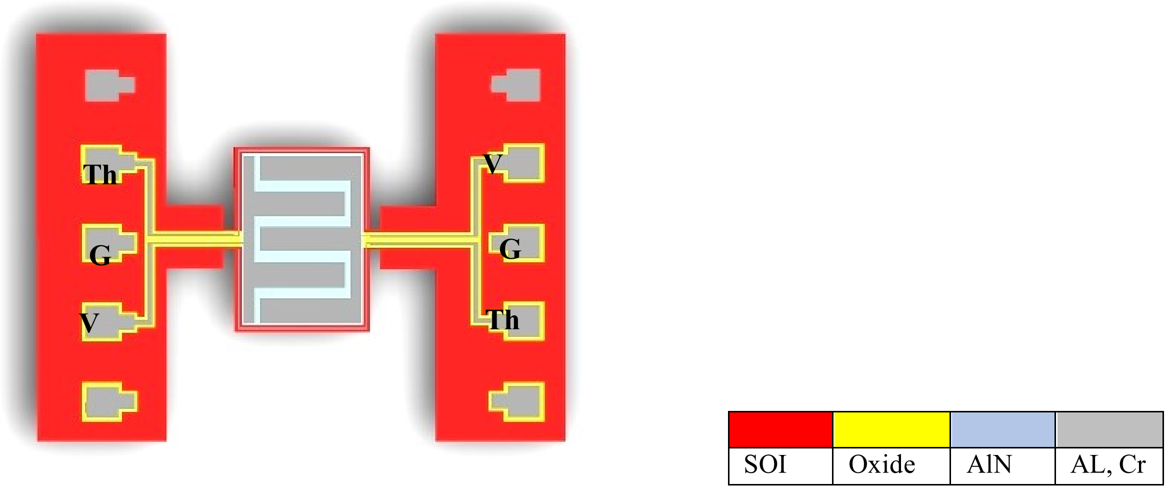

Figure. 4. 6: Simplified diagram of the rectangular resonator outlining the pads used for voltage tuning including two current heating elements.

Applying zero displacement boundary conditions to the anchor parts of the resonator model and neglecting the Piezoelectric effect in Mem-Mech modal analysis, the fifth lateral bulk mode resonant frequency as found to be 59.83 MHz as shown in Figure. 4.4.

A Finite Element (FE) model was developed using CoventorWare in order to design and simulate the Piezoelectric resonator. The model was discretized with 20-node hexahedral elements and the grid size was prescribed in mesh convergence study Sec 3. To determine the quality factor, Q_f of the designed resonator, anchor losses had to be evaluated, since it is well known that when a MEMS device resonates, some portion of the elastic energy propagates through the tethers into the surrounding structure to which the device is attached. In anchor loss analysis, the assumption is that elastic waves do not reflect from the substrate back into the resonator. Thus, instead of modelling the whole substrate a cubical region of the substrate is included for this analysis [125].

Extracting the lumped circuit's elements (Butterworth-VanDyke model) mentioned in Chapter 2, Sec 2.5.2.1 [36], including parallel (f_p) and series resonance frequencies (f_s) as were defined in (Eq.2.17) and (Eq.2.18) respectively. Other parameters like inductance L_m, capacitance C_m, and electromechanical coupling, k_{eff} (Eq.2.20) of the designed resonator model also were found using CoventorWare, FastPZE simulator [130]. The motional resistance R_m was deduced, as Q_f was obtained from anchor loss analysis.

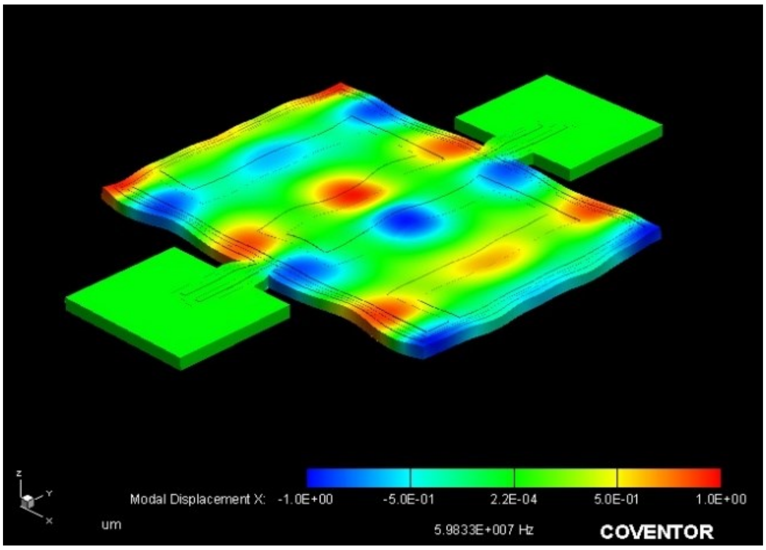

Figure. 4. 7: Modal Analysis shows the 5th mode shape having resonant frequency of 59.83MHz.

Following Mem-Mech modal simulation, the fast frequency response simulation (FastPZE) was conducted to obtain a high frequency response over a 30- 60 MHz frequency range, and the simulation necessary static mechanical and electrical boundary conditions has to be specified [125], in results the key lumped model BVD parameter are shown in Table.4.1 [121].

Table.4. 1: Extracted lumped circuit's parameters BVD - Fast PZE Results [121].

Motional resistance, *Rm*	353 Ω
Motional inductance, *Lm*	2.7 mH
Motional capacitance, *Cm*	2.56 fF
Series resonance frequency, *fs*	60.163 MHz
Parallel resonance frequency, *fp*	60.174 MHz
k_{eff}^2	0.00034
Q-factor	2919
Capacitance to ground, C_0	7.457 pF

4.4 Experimental Validation of Tuning Mechanisms

MEMS resonators operating in the lateral-mode and with piezoelectric actuation, have been successfully implemented with applications including filters and clock generators as a replacement of the quartz crystal component. These MEMS components can be effectively integrated within low power and low-noise oscillators [10,11,12].

Yet, the shift in the resonant frequency due to environmental conditions such as temperature and pressure variations, or fabrication process tolerances such as those due to geometrical dimensions and material properties variations is still considered to be a drawback for MEMS resonators [13]. Therefore, the capability of fine tuning of the resonant frequency is an important feature in some high precision applications [10]. The fabricated designed 5-element electrode resonator (RES3_5E_CT) received from MEMSCAP, including the U-shaped integrated surface heating elements, is shown in Figure. 4.8 [121].

4.4.1 Fabrication and Characterisation

The resonator (RES2_5E_TH), was characterized and tested for experimental validation of thermal and voltage tuning. Figure. 4.8 shows the micrograph of the designed and fabricated LBAW PiezoMUMPs resonator (RES2_5E_TH) including the integrated heating elements.

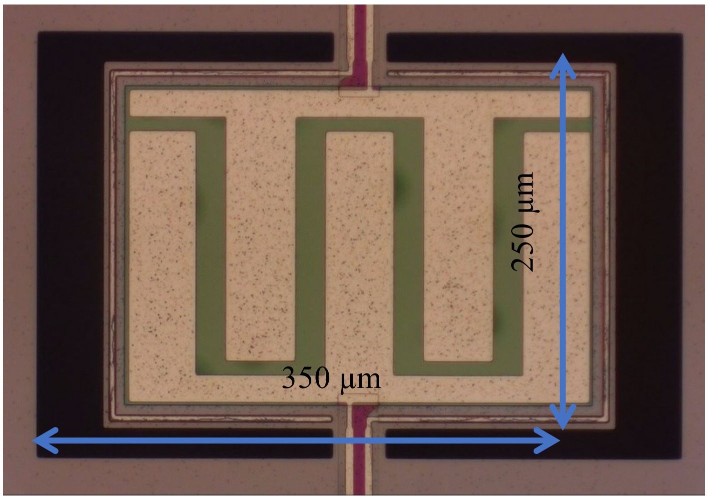

Figure. 4. 8: Micrograph of the designed and fabricated (RES2_5E_TH) including the integrated heating elements.

In order to have access to the five IDT Piezo MUMPs resonator, a two-port pocket vector network analyser (VNA) with 4000 steps points and a frequency range of 60.5–61.5 MHz has been used. This device is connected to a designed PCB using a couple of SMI connectors (Drive/ Sense), as shown in Figure. 4.9.

The frequency response of the designed resonator at room temperature was obtained from which the resonant frequency, quality factor and motional resistance were found to be 61.348 MHz, 3153 and 353 Ω respectively, as shown in Figure. 4.10. These results are close to the simulated values of 60.367 MHz for the resonant frequency and 2,874 for the quality factor.

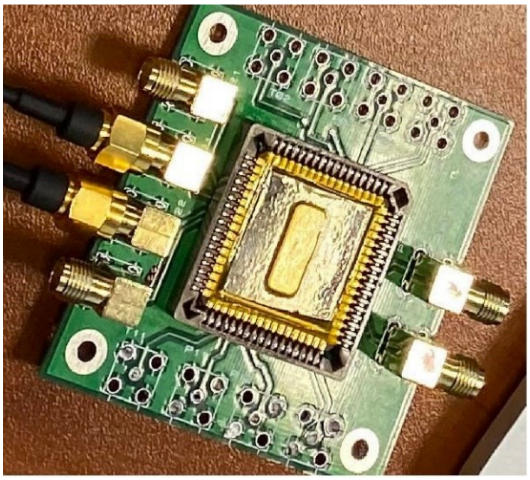

Figure. 4. 9: The PCB having the fabricated die interfaced through SMI connectors.

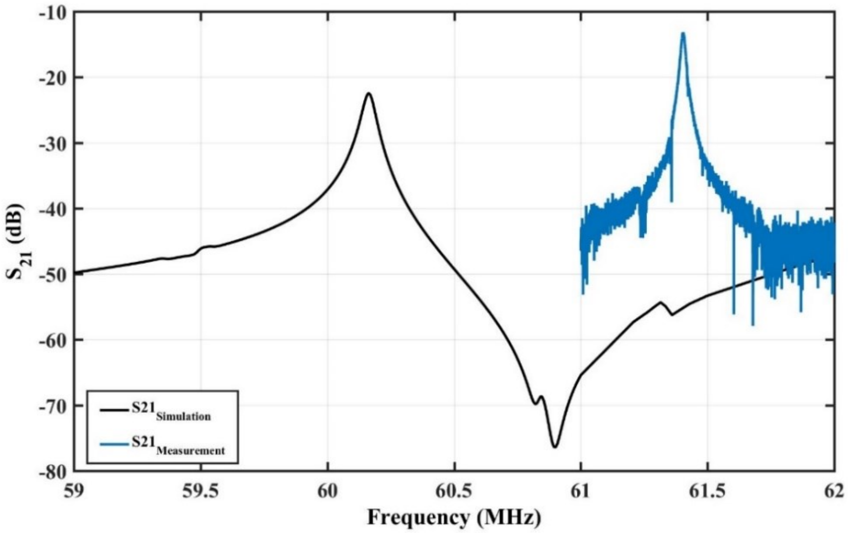

Figure. 4. 10: Plot of the transmittance spectrum |S21| for the 5th mode (f_{res} simulation = 60.367 MHz, f_{res} measured = 61.348 MHz).

4.4.2 Fine Tuning in LBAW PiezoMUMPs Resonator

Fine tuning is investigated via thermal tuning and voltage tuning where the resonant frequency of the structure can be modified by inducing additional stresses in the device. In thermal tuning the elastic properties are also varied via the application of a temperature change. This will lead to a variation in the resonant frequency and the quality factor which are here investigated experimentally for the fabricated prototypes.

4.4.2.1 Thermal Tuning

In the case of thermal tuning, heating the design such that the temperature increase, ΔT, is proportional to the power dissipated per unit volume, as it was noted that the temperature increase of the device will also result in variations of the Young's modulus, density and the dimensional length, L [120].

In addition, the thermal tuning, is approached either by;

Ovenisation: This method is applied by placing the MEMS dice in the Oven and heating the whole structure of the resonator.

Electrothermal: This method was suggested to heat the SOI layer either by heating the SOI surface only, or by heating the SOI bulk.

Characterisation results showing the effect of temperature variation induced via electrothermal tuning on the resonant frequency and quality factor of the fabricated MEMS resonators will be presented.

4.4.2.1.1 Ovenisation Tuning

This tuning method was carried out on (RES2_5E_TH) using Vötsch test chamber, by placing the PCB board including the fabricated MEMS Die, connected to a two port VNA through 50 Ω SMA thermal cables to determine the resonant frequency shift due to temperature change. Experimental results of the thermal effect on the resonant frequency exhibit a linear decrease over a range of 278 to 358 K. The experimental and simulated frequency-temperature slopes have almost the same value of -2.025 kHz/K, as shown in Figure. 4.11 (a), (b) where the transmission magnitude plots for the same temperature range are presented. The measured heater resistance was found to be around 19 Ω at room temperature. There is a constant difference between the simulated and measured resonant frequency which can be attributed to process variations. However, it can be noted that the change in the resonant frequency with temperature characteristic has the same gradient for both the simulated and experimental results.

It should be noted that the resonant frequency change with temperature is expected to follow the same trend even for other LBAW modes having different number of electrodes.

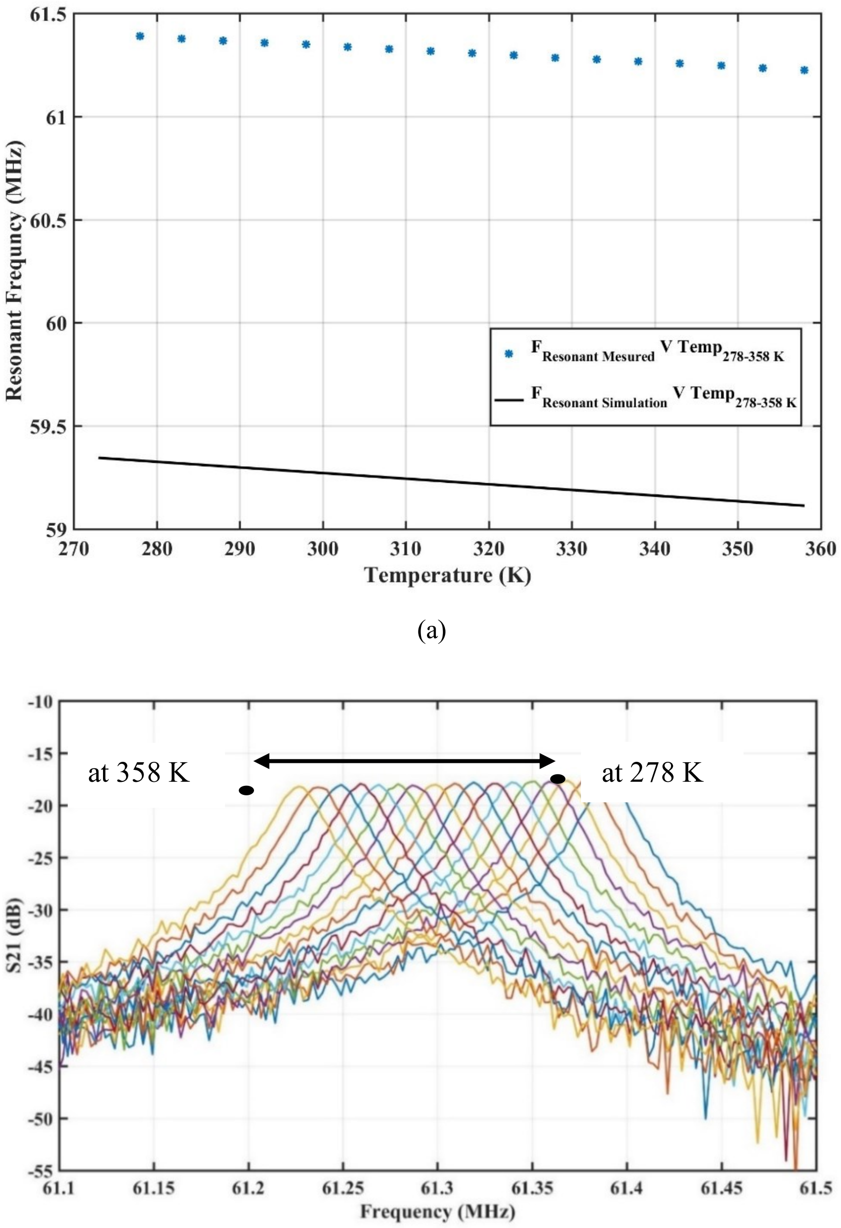

(a)

(b)

Figure. 4. 11: (a) Linear decrease in the resonant frequency (simulation and measured) versus temperature for the range of 278-358 K. (b) shows the measured transmission magnitude plots for different temperatures in steps of 5 K.

4.4.2.1.2 Electrothermal Tuning

Two different techniques were investigated in this section:

- **SOI Surface Heating;** An electrothermal heating element was implemented to the resonator structure by designing a U-shape heating element 5µm wide aluminium electrodes in contact with SOI were symmetrically positioned around the edge of the resonator, as it was shown in Figure. 4.3, the (RES2_5E_TH) including the symmetrical U-shaped surface heating elements. The narrow cross section of the heating element prevented it from handling the necessary current to heat the SOI surface of the resonator, which prevented any experimental findings from being recorded.
- **SOI Bulk Heating**; by placing two heating metal elements in both sides of the resonator (RES3_5E_CT) as shown in Figure. 4.12, so current will pass in closed loop circuit between these two metal elements, and the resistance (31 Ω) between these two electrodes can also be used to infer the temperature of the resonator.

Figure. 4.13 shows the micrograph of the designed and fabricated contour mode MEMS resonator (RES3_5E_CT) including two metal heating electrodes for a closed loop current circuit with bonding wires are shown, the other two metal elements have an oxide layer underneath to be connected to the pocket VNA, for resonant measurements as shown in Figure. 4.14. To achieve a different current supply, a voltage supply of 9 V and a series variable resistance ranging from 166Ω to 15kΩ were used. The results of the transmission magnitude plots for different heating currents are displayed in Figurers 4.15 and 4.16 respectively, and the effects of current variation on resonant frequency were recorded in Table. 4.2.

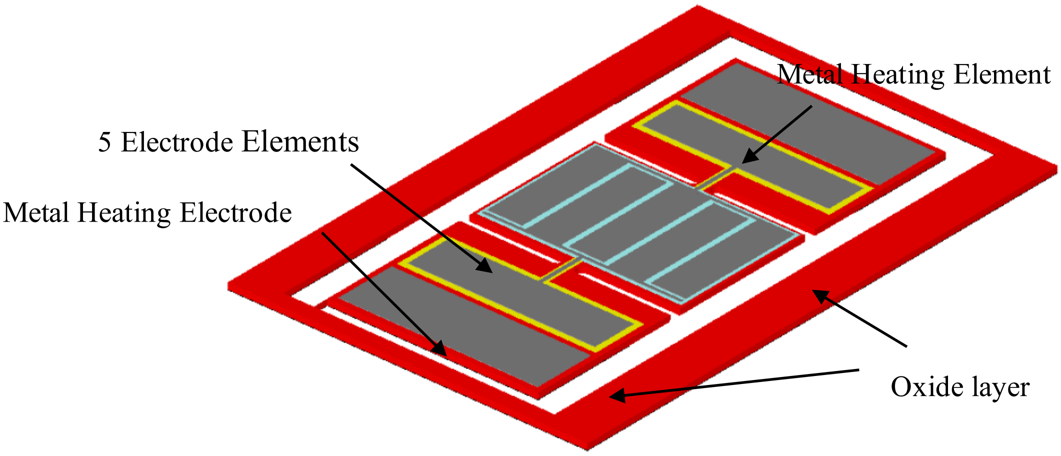

Figure. 4. 12: Simplified diagram of the rectangular resonator (RES3_5E_CT) Outlining the pads used for electrothermal tuning elements.

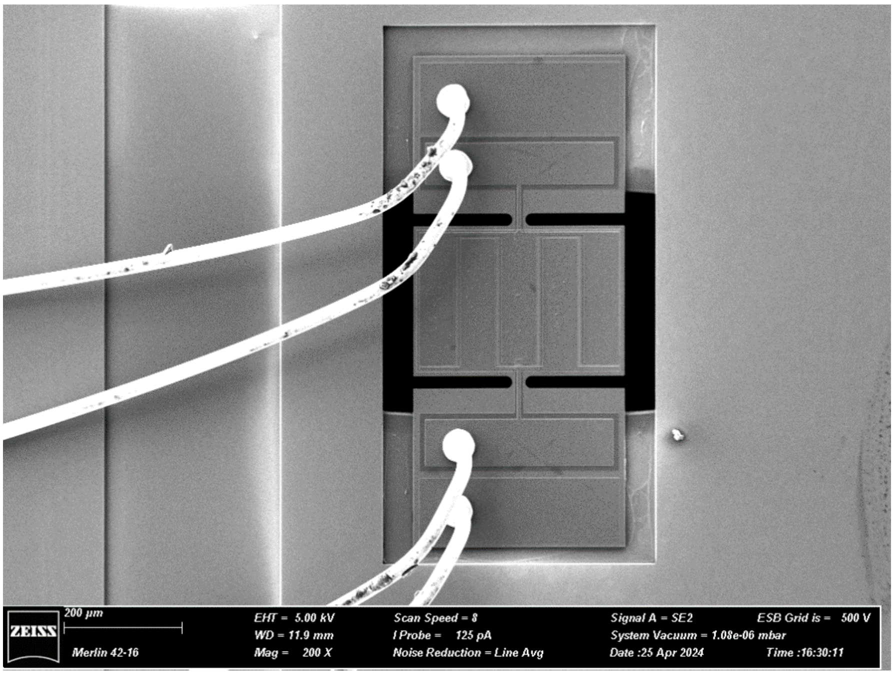

Figure. 4. 13: Micrograph of the designed and fabricated LBAW PiezoMUMPs resonator including two electrothermal elements.

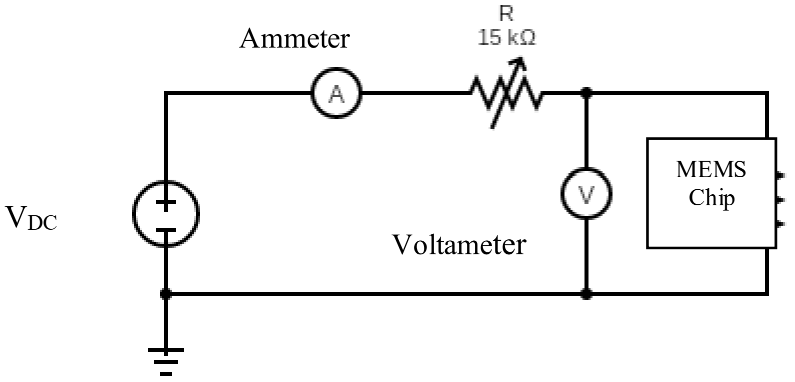

Figure. 4. 14: The electrical circuit for current in mA variation using variable resistance in KΩ in series with two thermal electric element's and RES3_5E_CT in a MEMS Chip.

Table.4. 2: Total resistance in series (Rs) effect on resonant frequency, electric power, and resistance of SOI layer.

R_s (KΩ)	f_r (MHz)	Q_f	I (mA)	V (V)	P (mW)	R_{bulk} (Ω)
0.166	61.368	1116	39.80	1.26	50.148	31.66
0.351	61.392	1123	29.50	0.92	27.140	31.19
0.491	61.410	1165	16.90	0.53	8.974	31.42
1.031	61.413	1201	8.38	0.26	2.170	30.91
1.491	61.414	1227	5.78	0.18	1.029	30.80
2.191	61.414	1239	3.80	0.12	0.456	31.58
4.631	61.415	1264	1.80	0.06	0.099	30.56
9.231	61.416	1219	0.98	0.03	0.027	28.57
13.831	61.419	1121	0.62	0.02	0.012	30.65
15.031	61.418	1200	0.59	0.02	0.012	33.90

From Table. 4.2, It is observed that the resonance frequency decreases linearly with increasing electrical power as it is shown in Figure. 4. 17, it is also was noticed that the SOI Bulk resistance R_{bulk} was almost stable. with magnitude of 31Ω as it is shown in Figure. 4.18.

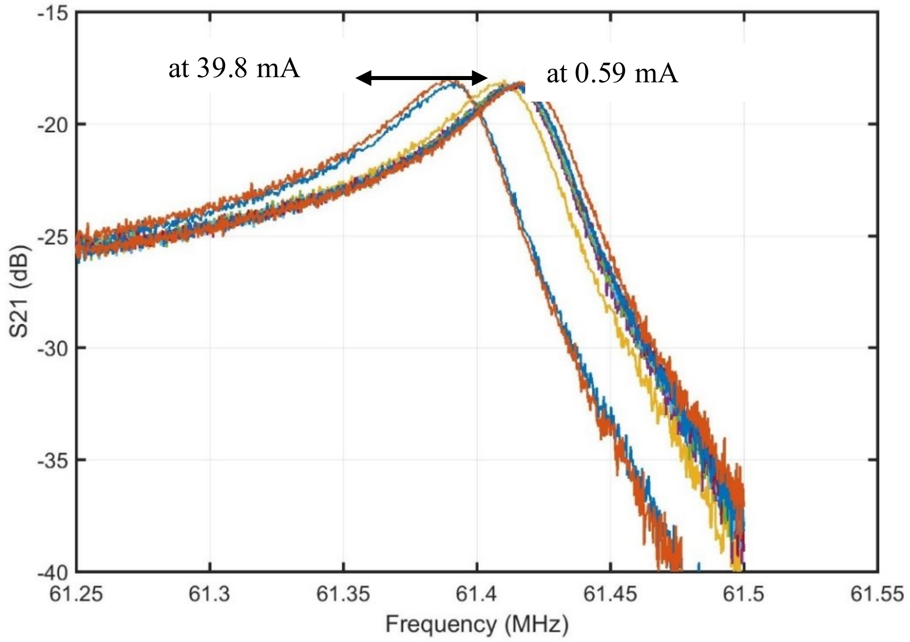

Figure. 4. 15: The transmission magnitude plots for different heating current mA.

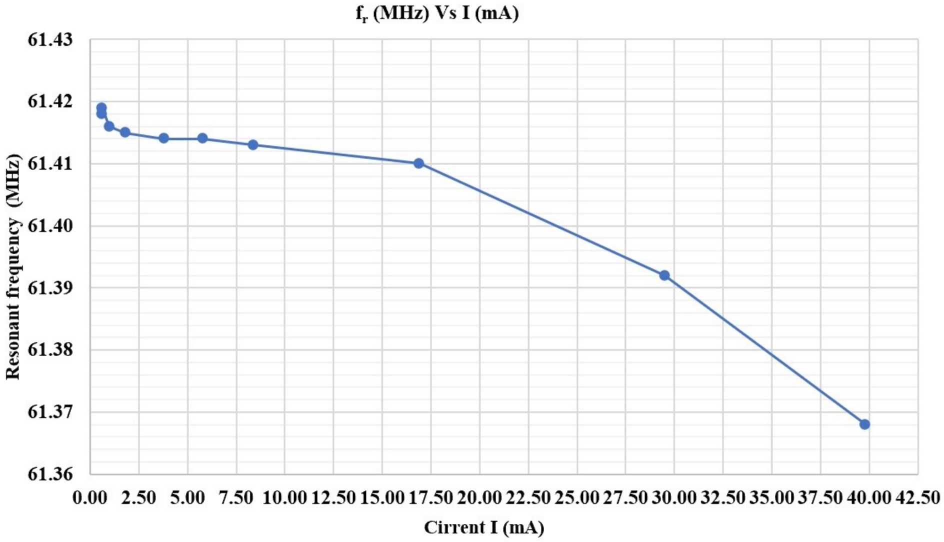

Figure. 4. 16: Linear decrease in the resonant frequency (measured) versus passing heating current for the range of 0-40 mA

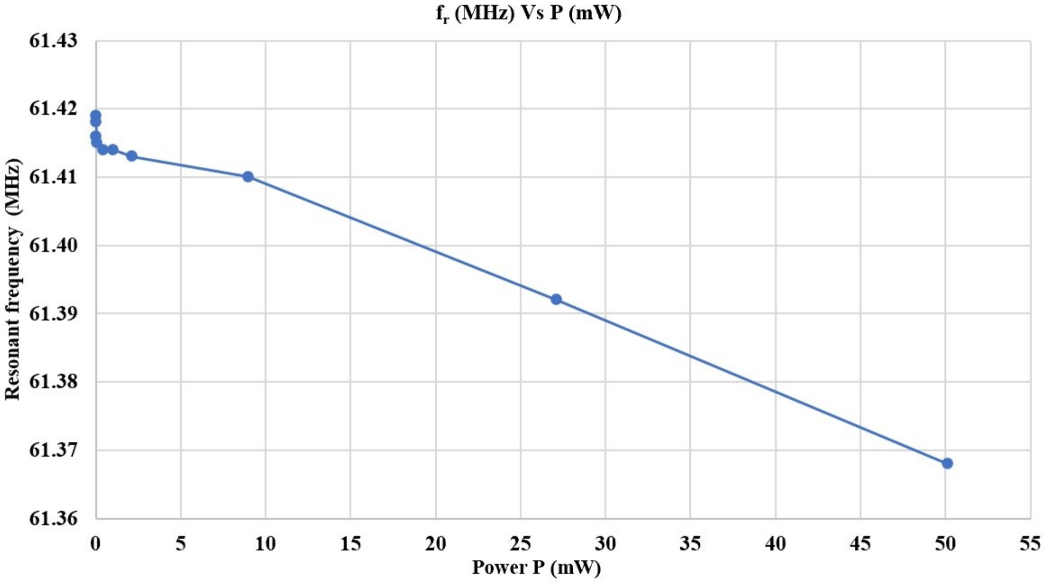

Figure. 4. 17: Change in the resonant frequency (measured) versus electrical heating power for the range of 0- 50 mW, showing an aproximatlly linear decrease.

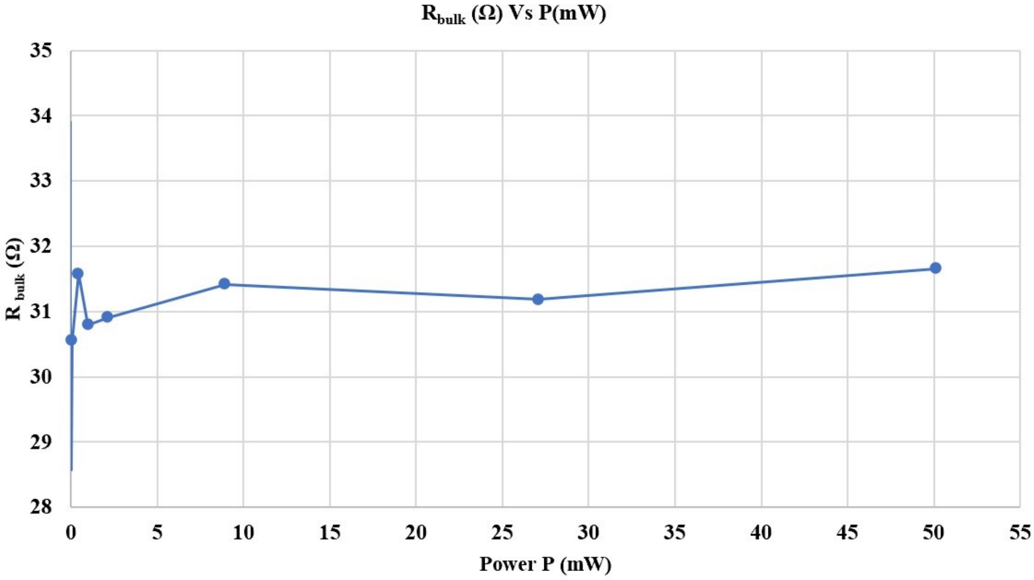

Figure. 4. 18: SOI bulk resistance almost constant over electrical heating power range.

4.4.2.2 Voltage Tuning

The resonant frequency can be tuned by applying a DC voltage to the piezoelectric material on top of the resonator in order to introduce a change in the stress of the piezoelectric layer relative to the silicon layer. Voltage tuning was also investigated experimentally and a decrease in the resonant frequency of -3.75 kHz/V over a DC tuning voltage range of 1-9 V was observed as shown in Figure. 4.19 (a, b). Figure. 4.19 (a, b) shows the transmission magnitude plots for different tuning voltages.

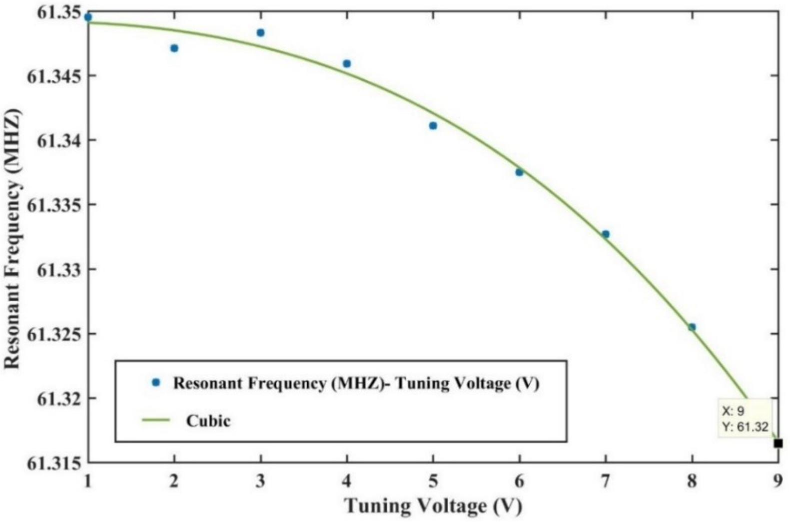

(a)

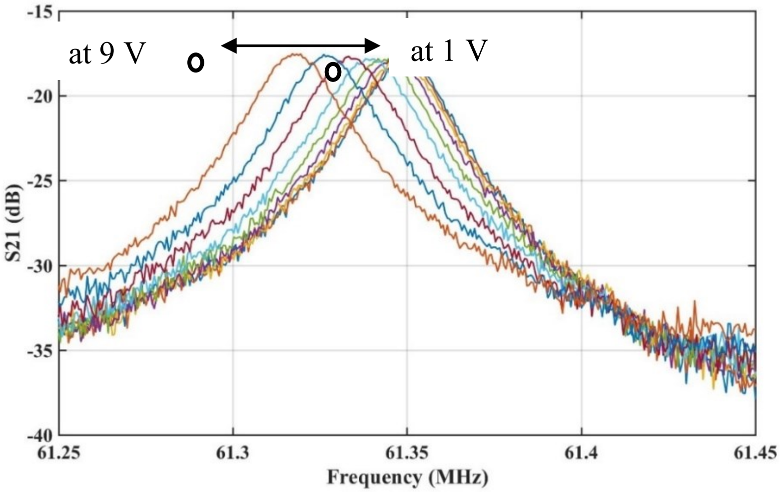

(b)

Figure. 4. 19: (a) Monotonic decrease in the resonant frequency over a voltage tuning range of 1-9 V. (b) The transmission magnitude plots for different tuning voltages in steps of 1V.

4.5 Discussion

One of the primary drawbacks of MEMS resonators was covered in this chapter: their resonant frequency is susceptible to modification due to external influences such as temperature or tolerances in the manufacturing process, such as differences in the geometrical dimensions and material quality [13]. Thus, the ability of a resonator to fine-tune its frequency is a crucial attribute in some high-precision applications. Therefore, three different techniques were successfully investigated for fine tuning: ovenisation, electrothermal heating, and voltage tuning. The fact that a frequency shift was observed without compromising the quality factor indicating that the LBAW PiezoMUMPs resonator operating in its fifth resonance mode may be fine-tuned.

Ovenisation tuning was carried out for experimental purposes but it is not practical to be implemented at the end-user application. Electrothermal tuning consumes significant power and may result in device degradation over time. Voltage tuning consumes no power and does not result in any device degradation but it requires higher voltages to achieve the same frequency variation. It should be noted that these tuning mechanisms can only partially compensate process-induced resonant frequency variations, but should be able to compensate for temperature-induced variations.

5. Electrostatically- Actuated Switches Using PiezoMUMPs

This chapter presents the design and fabrication of the three- and two-state mechanical contact type electrostatically-actuated MEMS switches for microwave band application utilizing PiezoMUMPs technology [7]. The objective of designing and fabricating the switch and the LBAW PiezoMUMPs resonator in the same die was to achieve a wide range of frequency tuning and a low-cost frequency switching mechanism in the VHF band. The design idea of this switch is based on the concept of a three state non-contact switch, this switch was fabricated using the technology of SOIMEMS and it has three main functions (ON-OFF and deep OFF) [91]. Starting with the same design structure as in [91], several switches were designed and their 3D models were built using CoventorWare software in order to explore the feasibility of utilising PiezoMUMPs technology in the design and simulate an electrostatic actuated switch. Figure. 5.1 shows a three state, non-contact one direction switch consists of two Drive Electrodes in opposite sides (D), two pair of Springs (S), one pair of Signal Line (SL) with signal line gap (g_s) between fingers and one Comb Finger with a gap (g_a) in each side.

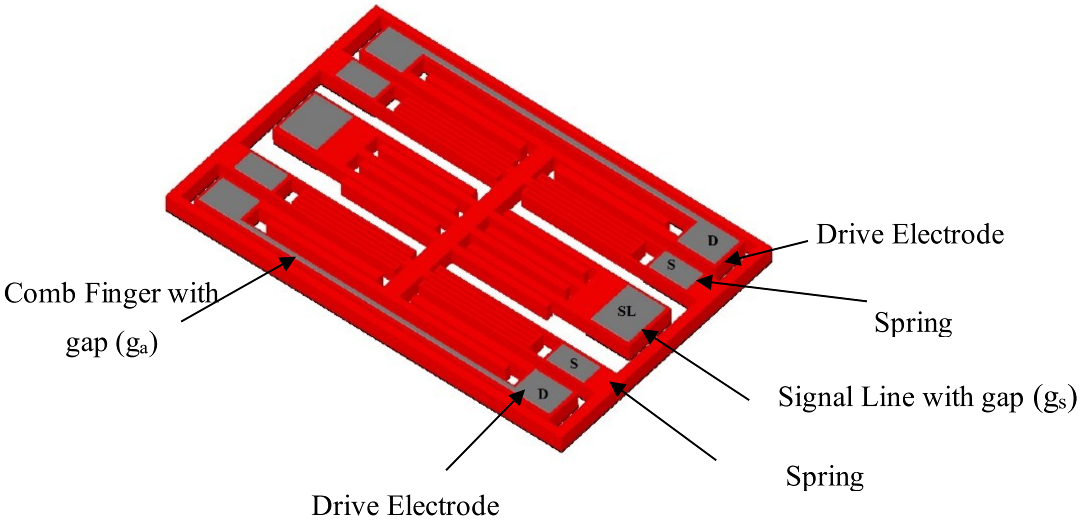

Figure. 5. 1: Three state non-contact one direction switch (SW1_1D_3S_FL_1_V0).

The mechanism principle of the proposed switches in this chapter is based on the movement of the electrostatic actuated electrodes. These electrodes can move laterally in one or both directions, changing the signal line they are in contact with state in the process. Furthermore, the chapter provides a thorough explanation of the design concerns, covering the design layout, spring geometry (including the number of turns), and the signal line contact surface profile. These switches are based on the mechanism of a capacitive mechanical-contact type switch; to achieve ON and OFF states the RF-MEMS switches utilize mechanical motion of suspended microstructures and the side wall of the lateral signal lines consists of doped SOI with no extra gold layer coating. Furthermore, switches optimizations work was done in order to: (i) improve the switching off function of a one-way switch (two states), thereby eliminating stiction in the on-state, (ii) addition of another set of signal lines in order to achieve two-way functionality and (iii) signal line contact surface optimization having three different profiles in order investigate the contact surface profile effect on signal coupling. These switches can be integrated with Piezo-actuated LBAW resonators to achieve the required frequency band switching, that gives a potential to conduct almost the same design methodology utilizing the technology of PiezoMUMPs, to be able to have a switchable array of different resonators in the same chip, thus achieving a cost reduction [126,127].

5.1 Design Concept and Process Description

The effects of changing the size and number of electrode elements on the pull-in voltage of the switches' design was examined using Finite Element Method (FEM) models. It was discovered that altering the springs' form improved the pull-in voltage. Table.5.1 outlines the different switches that are central to the analysis in this chapter, and additional optimizations are detailed in the subsequent sections.

Table.5. 1: The nomenclature of different switches discussed in the current Chapter.

Switch Notation	Direction	Number of states	Signal line contact surface type	Number of Comb fingers
(SW1_1D_3S_FL_1_V0)	1	3	Flat	1
(SW1_1D_3S_FL_5_V0)	1	3	Flat	5
(SW1_1D_3S_FL_7_V0)	1	3	Flat	7
(SW1_1D_3S_FL_14_V1)	1	3	Flat	14
(SW1_1D_2S_FL_7_V2)	1	2	Flat	7
(SW2_2D_2S_FL_7_V1)	1	2	Flat	7
(SW2_2D_2S_FL_8_V2)	1	2	Flat	8
(SW2_2D_2S_FL_7_V3)	1	2	Flat	7
(SW3_1D_2S_FL_14_V1)	2	2	Flat	14
(SW4_2D_2S_2FL_7_V1)	2	2	2 Flats	7
(SW2_2D_3S_FL_7_V4)	2	3	Flat	7
(SW2_2D_3S_ZL_7_V4)	2	3	ZigZag	7
(SW2_2D_3S_TL_7_V4)	2	3	Trapezoidal	7
(SW4_2D_2S_2TL_7_V1)	2	2	2 Trapezoidals	7

Figure. 5.2 shows (SW1_1D_3S_FL_7_V2) the three-state switch (ON-OFF and deep OFF) were number of electrodes are 28 and all in one-way lateral movement, one signal line (SL), pair of springs(S), this switch can be integrated with a 5th mode LBAW PiezoMUMPs resonator. Figure. 5.3 shows (SW2_2D_2S_FL_7_V2) the one direction, two-state switch.

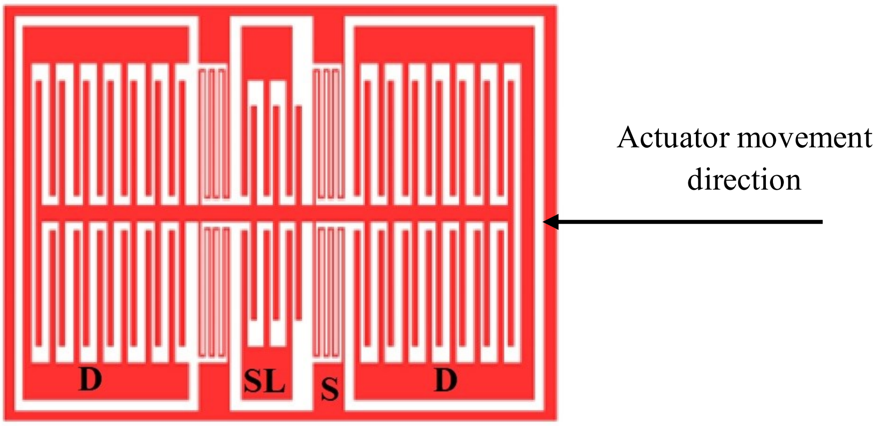

Figure. 5. 2: Three state non-contact one direction switch (SW1_1D_3S_FL_7_V2).

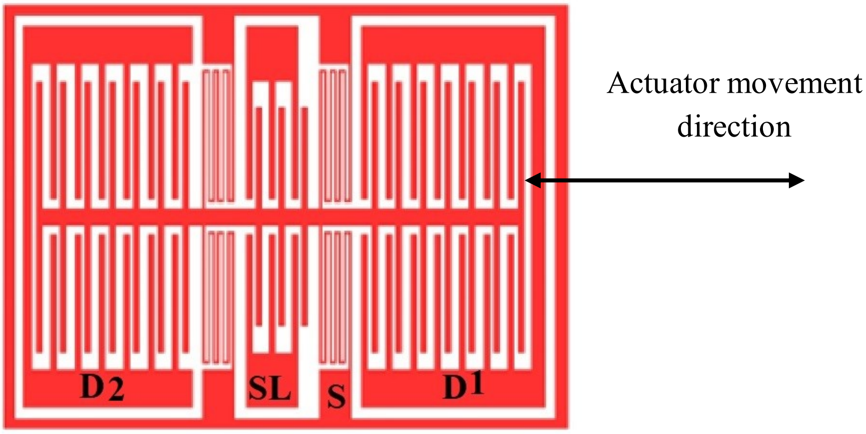

Figure. 5. 3: Two state,two-way (double throw) switch (SW2_2D_2S_FL_7_V2).

The switches were fabricated using the PiezoMUMPs process as described in detail in Chapter 2 section 2.8. In the SOI layer, features of 3 µm point to point surface contact profile can be achieved using Deep reactive-ion etching (DRIE), while open bottom cavities are achieved through backside etching. A cross-section showing the layers which make up both the switch and the resonator is shown in Figure. 5.4.

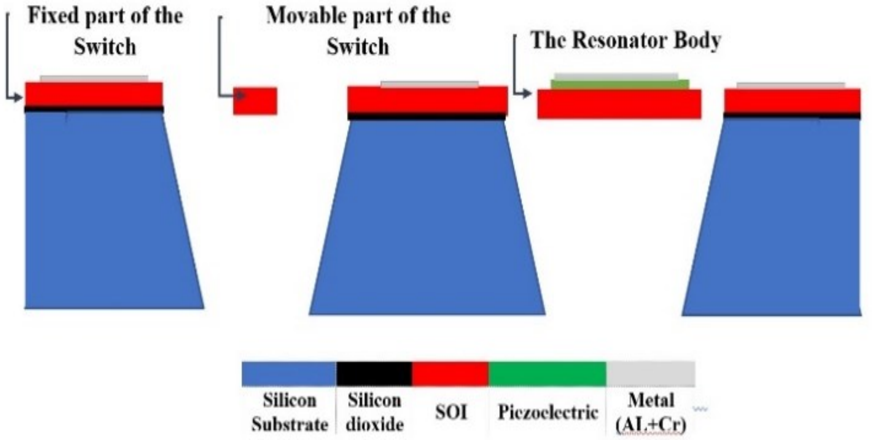

Figure. 5. 4: Cross-section of the designed switch and resonator.

5.2 Design steps and Geometry Adjustments

Commencing with the switch depicted in Figure. 5.1 (SW1_1D_3S_FL_1_V0), FEA-Cosolve simulations were conducted to determine the pull-in voltage. A DC analysis type and an accelerated convergence algorithm were chosen to evaluate the efficacy of the designed switch by reducing the pull-in voltage and enhancing the spring stiffness.

5.2.1 Switch Pull-in

Pull-in voltage is the most important performance parameter in switch design, and it can be lowered by adding more electrodes. Table. 5.2 illustrates the ways in which the three-state switch designs (SW1_1D_3S_FL_1_V0, SW1_1D_3S_FL_5_V0, and SW1_1D_3S_FL_7_V0) can be altered by adjusting the pull-in voltage in accordance with the number of comb driving fingers on the movable electrode.

Table.5. 2: Three different designs of a 3 state non-contact Switch, (a), (b), (c).

<table>
<tr><th>Switch 3D model</th></tr>
<tr><td>
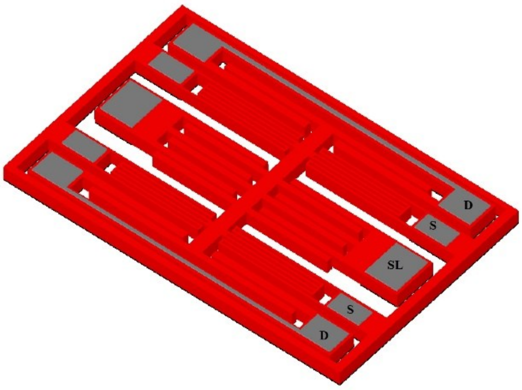

<table>
<tr><td>(a)</td><td>FEA Pull-in (V)</td><td>145</td></tr>
<tr><td>(SW1_1D_3S_FL_1_V0)</td><td>Number of comb fingers</td><td>1</td></tr>
</table>
</td></tr>
<tr><td>
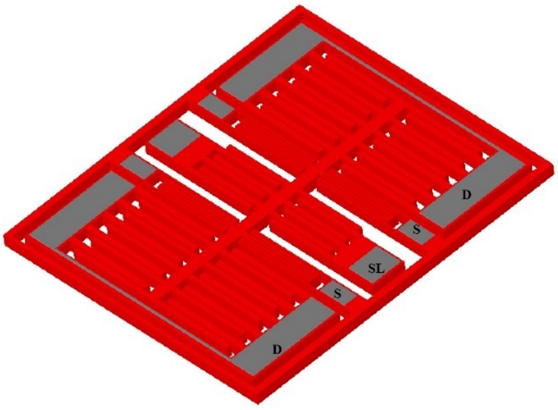

<table>
<tr><td>(b)</td><td>FEA Pull-in (V)</td><td>63</td></tr>
<tr><td>(SW1_1D_3S_FL_5_0)</td><td>Number of comb fingers</td><td>5</td></tr>
</table>
</td></tr>
<tr><td>
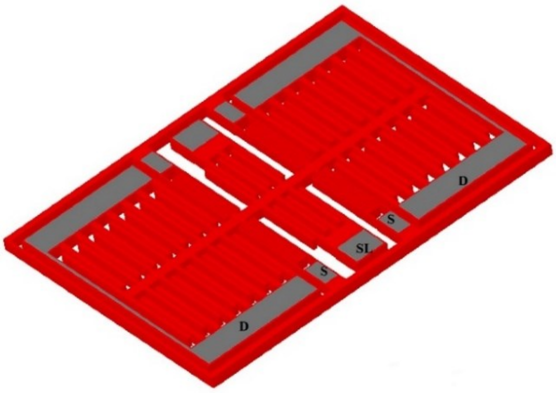

<table>
<tr><td>(c)</td><td>FEA Pull-in in (V)</td><td>55</td></tr>
<tr><td>(SW1_1D_3S_FL_7_V0).</td><td>Number of comb fingers</td><td>7</td></tr>
</table>
</td></tr>
</table>

5.2.2 Switch Spring Design

Due to the spring stiffness, the value of the pull-in voltage is considered high in the previous designs, so by changing the spring design, having a length x width of 160 X 24 µm, helped to reduce the pull-in voltage. Optimizing the spring design, increasing the number of comb drive Fingers, and changing the design from a 3-state switch to a 2-state switch. All these variations affect the pull-in voltage as presented in Table.5.3.

Table.5. 3: Different designs of a 2, 3 state non-contact Switch.

Switch Notation	Switch type/ Spring design	No of Comb Fingers	FEA Pull-in (V)
(SW1_1D_3S_FL_7_V1)	3 State  Two-anchored Points Spring, two Turns.	7	31
(SW1_1D_3S_FL_7_V2)	3 State  Two-sided anchored Spring, 3 Turns.	7	27
(SW2_2D_3S_FL_7_V2)	3 State  Two-sided anchored Spring, 3 Turns, Optimized dimensions.	7	21
(SW2_2D_3S_FL_8_V3)	3 State, Two-sided anchored Spring, 3 Turns, Optimized dimensions.	8	20.5
(SW3_1D_2S_FL_14_V1)	2 State, Two-sided anchored Spring, 3 Turns, Optimized dimensions.	14	14

The (SW3_1D_2S_FL_14_V1) switch geometry had to be optimized and the final devise parameters are described respectively in Table. 5.4, as well as both two-state (SW1_1D_2S_FL_7_V2) and a three-state (SW2_2D_3S_FL_7_V3), this switch optimization was investigated after geometry adjustments, all exhibited actuation motion, rendering a sidewall contact between adjacent signal fingers. The designs employ a serpentine spring structure which is also was optimized for low lateral bending stiffness, to minimise the pull-in voltage, and a total of four serpentine springs were used, located in such a way to restrict the movement in the required axial direction.

Table.5. 4: Design Parameters of (SW3_1D_2S_FL_14_V1).

Actuation finger length (μm)	120
Actuation finger width W_c, (μm)	8
Actuation finger gap g_a, (μm)	3.5
Actuation finger overlap length y_a, (μm)	110
Spring length, (μm)	146
Spring width (μm)	3
Device (SOI) thickness (μm)	10
Signal finger gap g_s (μm)	3
No. of actuator fingers (n)	14

5.3 Comparison

This section presents a comparison between both three (SW2_2D_3S_FL_7_V2) and two states (SW3_1D_2S_FL_14_V1) switches, and a discussion on coming sections in details including the effect of the design change on the pull-in voltage.

5.3.1 Three-State Switch Design

The three-state switch (SW2_2D_3S_FL_7_V3) design is based on two comb drive structures, having an actuation finger gap ga working in opposite directions as shown in Figure. 5.1. The operational modes of the switch are detailed in Table. 5.3. With no actuation voltage applied, the switch is in the off-state with an initial signal finger gap gs. In the on-state, the signal gap is reduced to zero, thus achieving mechanical contact. In the deep-off-state, the signal gap is further increased to achieve enhanced isolation. The deep-off actuator may also be used to retract the moveable signal fingers in the case of large stiction forces, provided that the gap between the actuation pairs is greater than gs+ga. The corresponding pull-in voltage, obtained using a coupled electromechanical simulation CoventorWare, Cosolve is 20.6 V. The implemented spring design consists of single anchor point and a total of six turns resulting in an overall spring constant of 67 N m-1. This value was confirmed via FEM simulations performed using CoventorWare, Mem-Mech. Further design details and parameters are listed in Table. 5.5.

Table.5. 5: Operation of the three-state switch.

State	Signal finger gap g_s (μm)	Left actuation finger gap g_a (μm)	Right actuation finger gap g_a (μm)
OFF	3	3.5	3.5
ON	0	0.5	6.5
Deep-OFF	6	6.5	0.5

5.3.2 Two-State Low-Voltage Switch Design

Although a three-state switch (SW3_1D_2S_FL_14_V1) design has been investigated, in practice for the VHF band, the deep-off state may not be required, since acceptable isolation is already achieved in the off-state. Therefore, a two-state switch design (SW2_2D_3S_FL_7_V2) is being proposed in order to minimise the pull-in voltage for the same device area, by having both actuators working simultaneously in the same direction as it was shown in Figure. 5.3. This lower actuation voltage makes the design more compatible with integrated circuit processes. The corresponding pull-in voltage, obtained using a coupled electromechanical simulation CoventorWare, Cosolve is 14V. A comparison of the displacement versus actuation voltage for both designs as shown and presented in Figure. 5.5.

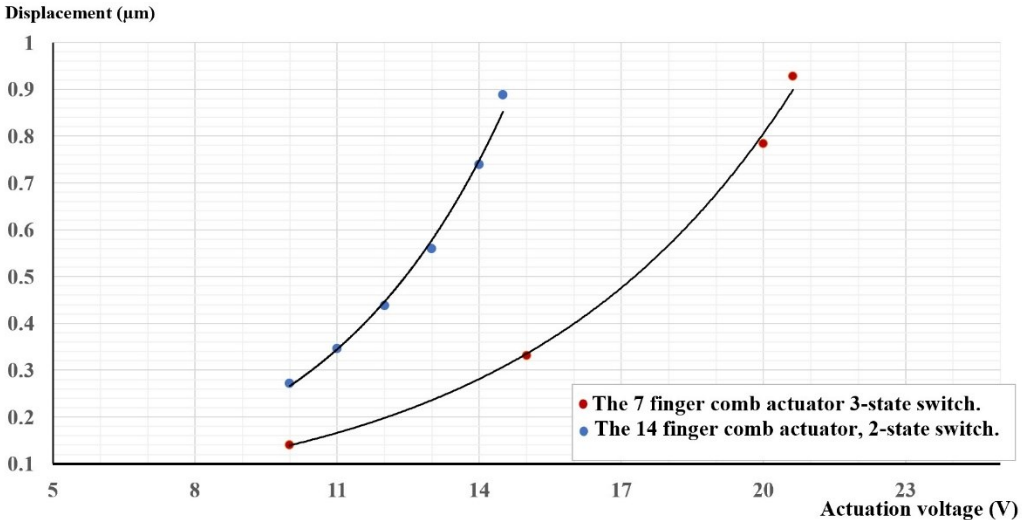

Figure. 5. 5: Maximum displacement versus actuation voltage for (i) the 7-finger comb actuator, 3-state switch (SW2_2D_3S_FL_7_V2) and (ii) the 14-finger comb actuator, 2-state switch (SW3_1D_2S_FL_14_V1).

5.4 Switch Optimization

This section explores different approaches to optimize switches to reduce the pull-in voltage and focuses on side wall stiction. It examines how the number of comb elements and the design of the actuation electrode affect the pull-in voltage and evaluates how the signal line contact surface affects signal coupling.

5.4.1 Actuation Electrode Design Optimization and The Pull-in Voltage

Two different types of switch actuation mechanisms adopted in this work, one-way switch with electrostatic actuation in one direction (SW3_1D_2S_FL_14_V1) as it is shown in Figure. 5.6, this switch is prone to stiction in the on-state, due to the mechanical contact of the signal sidewall surfaces. Figure. 5.7 shows a two-way switch with electrostatic actuation in two opposing directions (SW2_2D_3S_FL_7_V2), thus eliminating the problem of stiction in the on-state, by including a set of electrostatic fingers which are actuated during switch-off. The proposed design in Figure. 5.8 is a two-way switch (obtained using an extra set of signal lines) connected to two lateral bulk acoustic wave (LBAW) resonators (SW4_2D_2S_2FL_7_V1). The dimensions of (SW3_1D_2S_FL_14_V1) is 635x 360 μm^2, the signal line, and actuation electrode length are 129 and 150 µm respectively while the signal line gaps are 3 / 9 µm, and the electrode gaps is 3.5/10.5 µm, these dimensions are the same for (SW3_1D_2S_FL_14_V1).

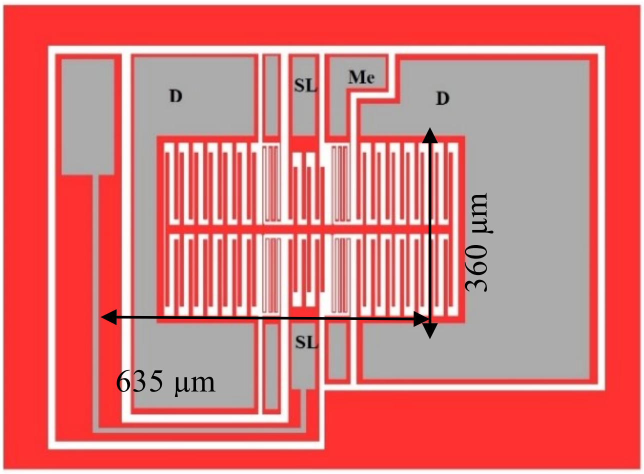

D	Drive
SL:	Signal Lines 1,2
ME:	Moveable electrode

Figure. 5. 6: One direction-actuated Switch (SW3_1D_2S_FL_14_V1).

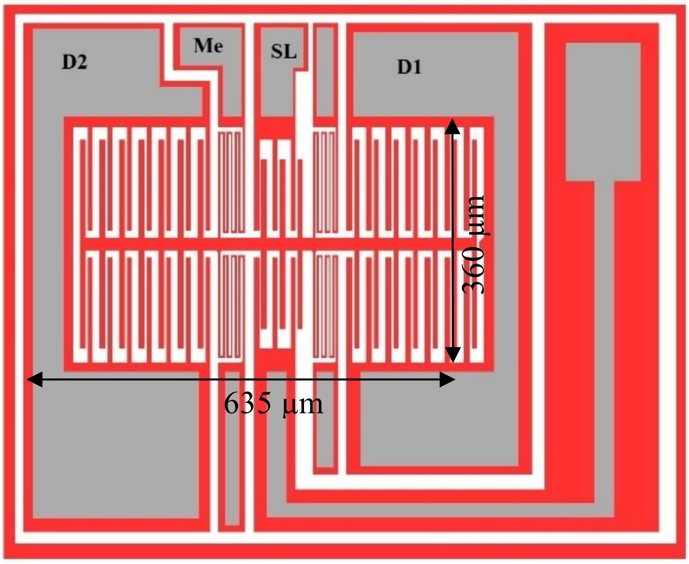

D1, D2:	Drive (on), Drive (off)
SL:	Signal Lines 1,2
ME:	Moveable electrode

Figure. 5. 7: Two direction-actuated Switch (SW2_2D_3S_FL_7_V2).

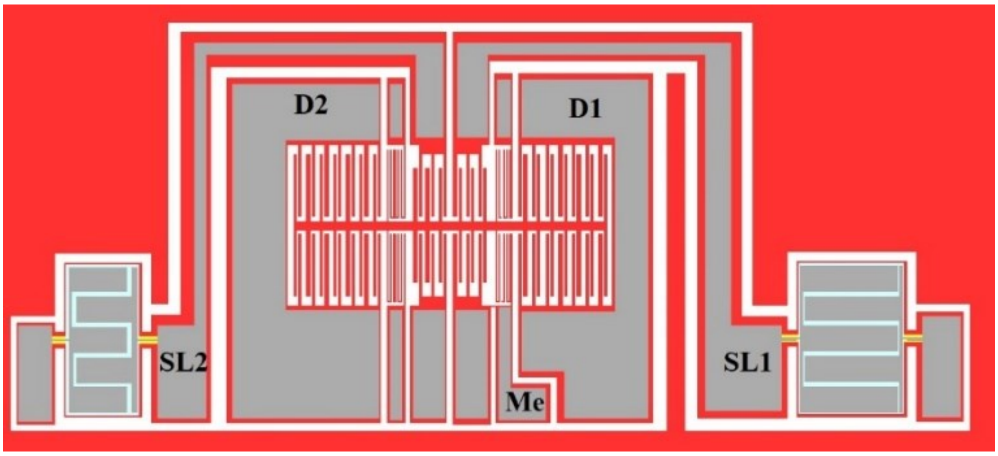

D1,D2:	Drive
SL:	Signal Lines 1,2
S:	Spring
ME:	Moveable electrode
R1,2 :	PiezoMUMPs LBAW resonators.

Figure. 5. 8: The two state, two-way (double throw) switch for two different resonant PiezoMUMPs Resonators (SW4_2D_2S_2FL_7_V1).

In all cases, the simulated spring stiffness constant is 18 N/m. This results in a switching time of approximately 0.90 µs. These simulations were conducted using coupled electrostatic and mechanical domains via CoventorWare, Cosolve module.

5.4.2 Signal Line Contact Surface Profile

This study examined how the various signal line surface characteristics given in Table.5.6 affected signal coupling. As it is shown three different surface contact profiles were designed to be tested in order to validate the effect of the contact surface in the value of the capacitors at ON and OFF states, all three surface profiles have a gap of 3µm at OFF state [127].

Table.5. 6: Different signal line surface profiles for a two state switch SW2_2D_2S_FL_7_V3 : (a) Flat SW2_2D_2S_FL_7_V4, (b) Zigzag SW2_2D_2S_ZL_7_V3, (c) Trapezoidal SW2_2D_2S_TL_7_V4.

Switch Signal Line Profile	**3D layout**
(a) Flat contact gap 3µm	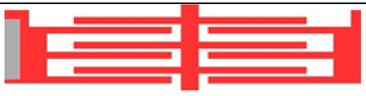
(b) ZigZag Contact point to Flat Surface gap 3 µm	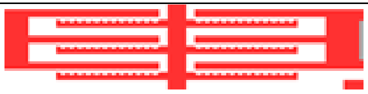
(c) Trapezoidal surface to Flat Surface gap 3 µm	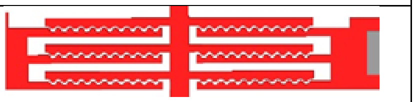

5.5 Fabrication and Testing

Both the three-state and two-state switch designs were fabricated and tested using two testing criteria. Utilizing Micro-tech probing needles for switch characterization for non-bonded switches. An alternative technique involved MEMS die was wire bonded for testing, designing multiple PCB boards to mount the MEMS die and access each switch through SMA connectors. The upcoming section will explain both measurement methods, with the results being included for comprehensive analysis.

5.5.1 Non-Wire Bonded Switches Prototypes

The micro-photograph for unidirectional three state switch (SW1_1D_3S_FL_14_V1) is shown in Figure. 5.9 this switch reached on state at pull-in voltage 17.6 V. The low voltage optimized switch (SW3_1D_2S_FL_7_V1) is shown in Figure. 5.10, this switch was integrated with a 60 MHz LBAW PiezoMUMPs resonator [120], and the signal path between the switch and the resonator was implemented using an aluminium layer over a silicon dioxide insulating layer.

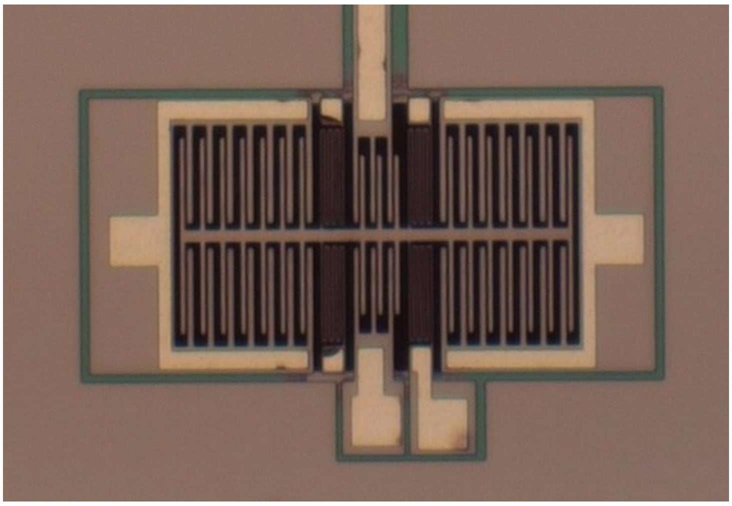

Figure. 5. 9: Micro-photograph of the fabricated three-state one direction switch ((SW1_1D_3S_FL_14_V1)) with a 14-finger comb actuator.

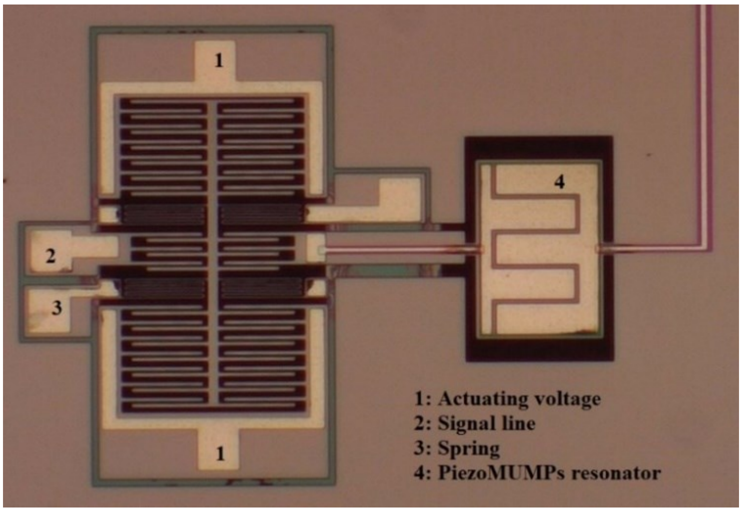

Figure. 5. 10: Micro-photograph of the low voltage optimized switch (SW3_1D_2S_FL_14_V1) integrated with the Piezo lateral bulk acoustic wave resonator.

The switch (SW3_1D_2S_FL_14_V1) was characterized using a Cascade Probing Station, as shown in Figure. 5.11, where the actuation voltage was applied using tungsten Cascade Micro-tech probing needles. Both signal finger gap g_s and actuation finger gap g_a of switch (SW3_1D_2S_FL_14_V1) measurements obtained using 100X lens and results are shown in Table.5.7.

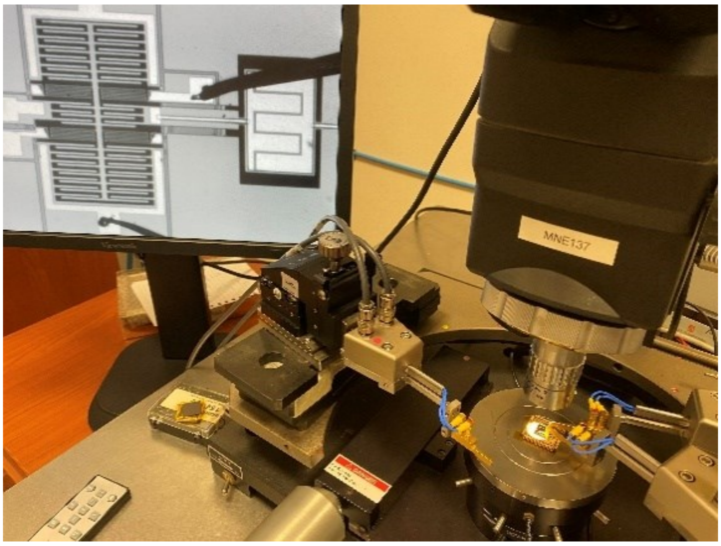

Figure. 5. 11: Experimental setup for the (SW3_1D_2S_FL_14_V1) two-state low voltage switch.

Table.5. 7: Measurements carried out using a 100X lens.

Gap	Designed	Measured
Signal finger gap g_s (µm)	3	3.1
Actuation finger gap g_a (µm)	3.5	3.6

The required actuation voltage was found to be 17 V in the case of the (SW3_1D_2S_FL_14_V1) two-state switch, Figure. 5.12 shows the switch in actuated ON state, as it was found in the ON-state the signal path was to be equivalent to a capacitance of 220 fF in series with a resistance of 6.4 kΩ at 1MHz.The presence of the series capacitance is due to the presence of a thin oxide on the contact SOI signal path fingers. The required actuation voltage was found to be 19.3 V in the case of the three-state switch, Figure. 5.13 shows the switch in actuated ON state [127].

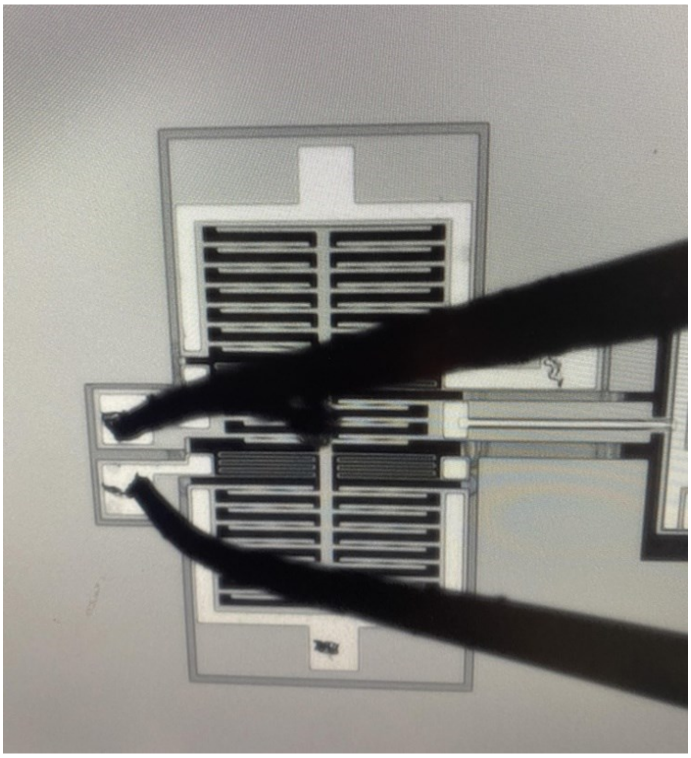

Figure. 5. 12: The two-state low voltage switch (SW3_1D_2S_FL_14_V1) in actuated ON state.

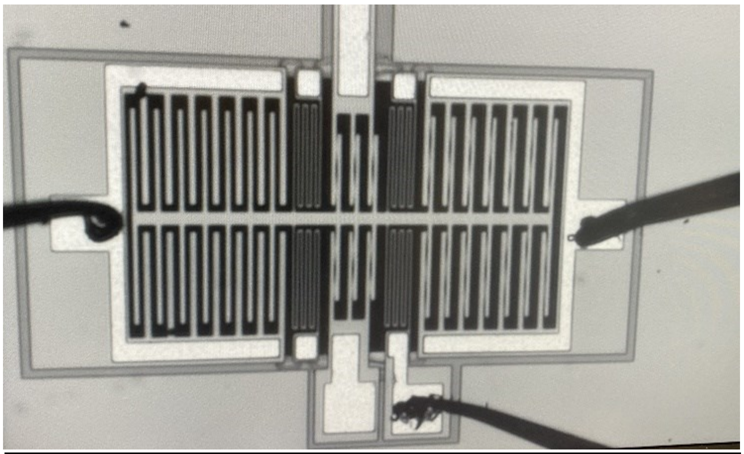

Figure. 5. 13: The three -state low voltage switch (SW2_1D_3S_FL_7_V4) in actuated ON state.

Table.5.8 shows simulated and measured pull-in voltage for designed and fabricated switches.

Table.5. 8: Simulated and measured pull-in voltages.

Switch Type	Simulated Pull-in Voltage (V)	Measured Pull-in Voltage (V)
SW3_1D_2S_FL_14_V1	14	13.6
SW2_2D_3S_FL_7_V4	21	17.6
SW4_2D_2S_2FL_7_V1	30	18.7

5.5.2 Wire Bonded Switches prototypes

Several PCB boards were specially designed to access every switch on the MEMS die to reduce the impacts of parasitic resistance and noise that were observed in previous experiments as shown in Figure. 5.14. These PCB designs incorporate additional circuitry elements essential for testing.

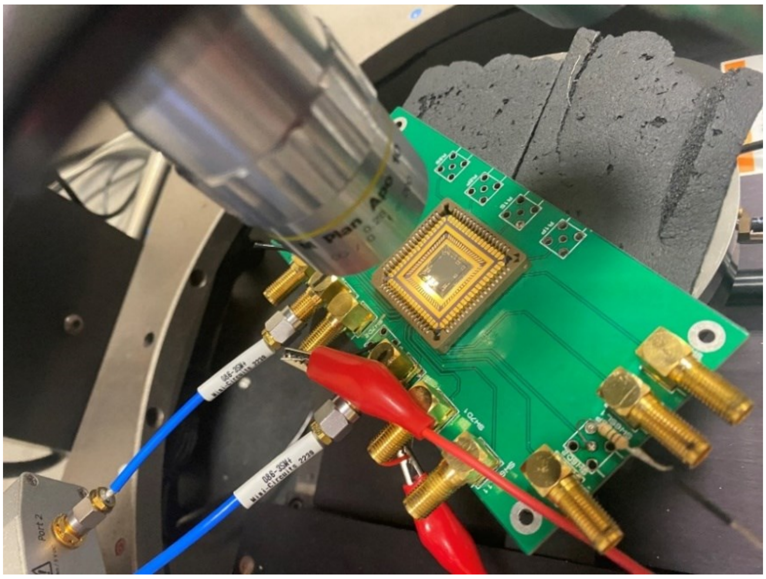

Figure. 5. 14: PCB designed for one of the fabricated MEMS switch under the microscope during the characterization experiment of (SW2_2D_3S_FL_7_V4) switch.

Figure. 5.15 shows micro-photographs of (SW2_2D_3S_FL_7_V4) having a signal line with a flat contact profile in the ON state and OFF state.

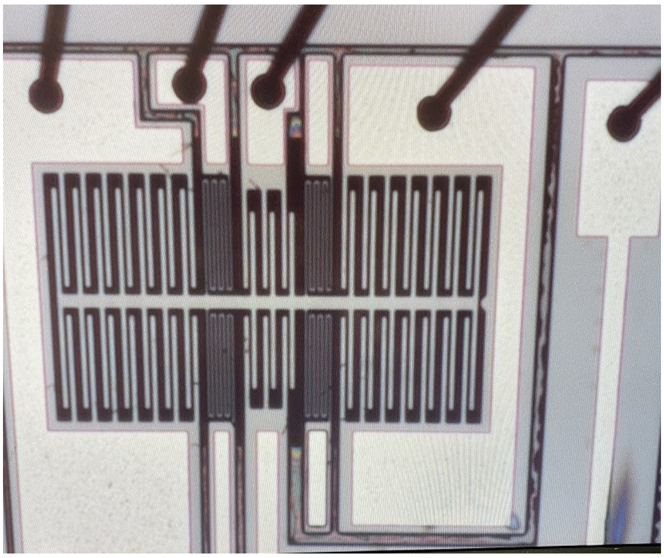

Figure. 5. 15: (SW2_2D_3S_FL_7_V4)with flat signal line surface profile .

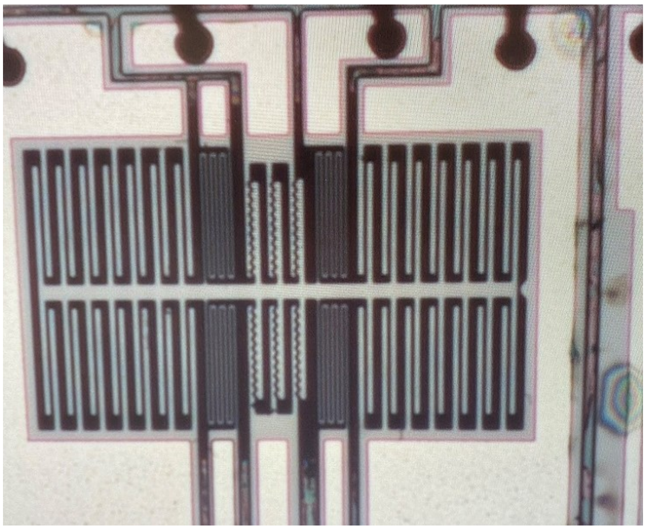

Figure. 5. 16: SW2_2D_3S_TL_7_V4 with trapezoidal signal line conact surface profile.

Figure. 5.17 shows micro-photographs of SW2_2D_3S_FL_7_V4_V1 showing the Comb fingures at “ON state”, and “OFF State”, as well as the signal line with a Flat contact surface profile.

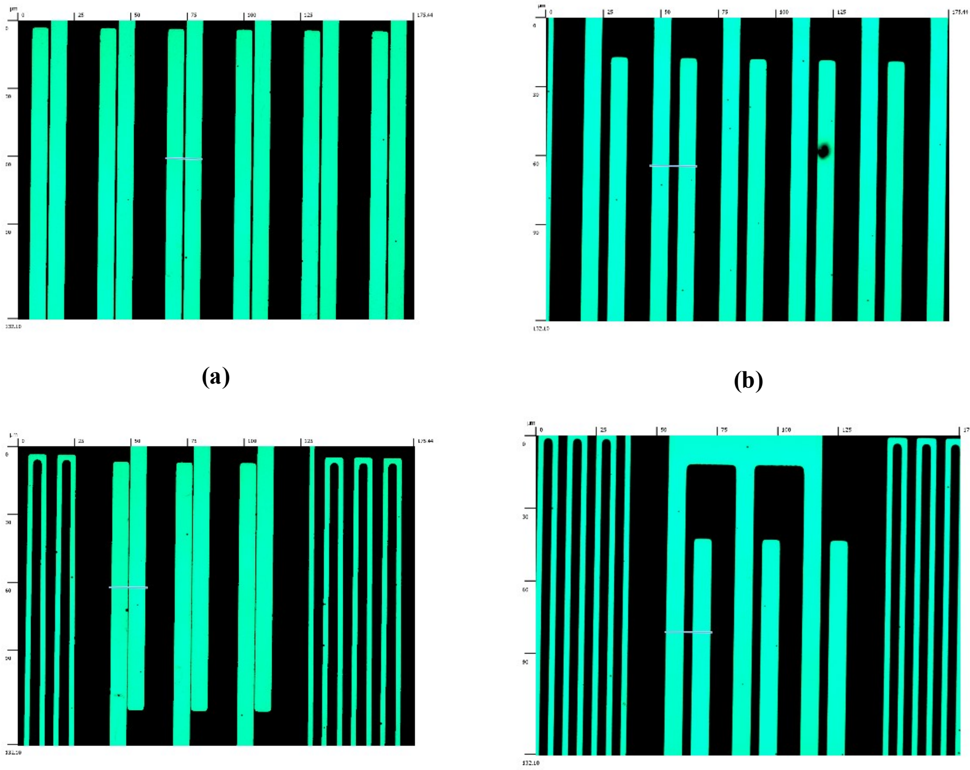

(a) (b)

(C) (d)

Figure. 5. 17**:** Micro-photographs of (SW2_2D_3S_FL_7_V4): (a) Comb fingures “ON state”, (b)) Comb fingures “OFF State”, (c) Signal line ON State Flat contact surface, (d) Signal line OFF State Flat contact surface.

Figure. 5.18 shows micro-photographs of (SW4_2D_2S_2TL_7_V1) having two signal line with a trapezoidal contact profile in the ON state (a) and OFF state (b), and the pull-in voltage at ON state was 15.7 V and 5.7 V at OFF state.

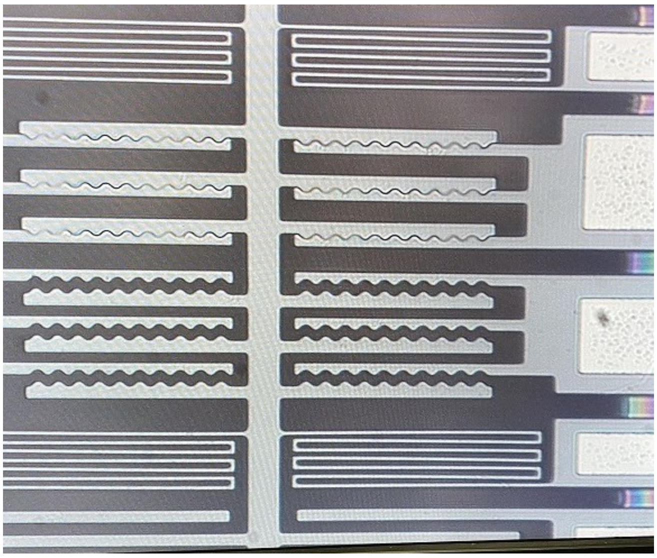

(a)

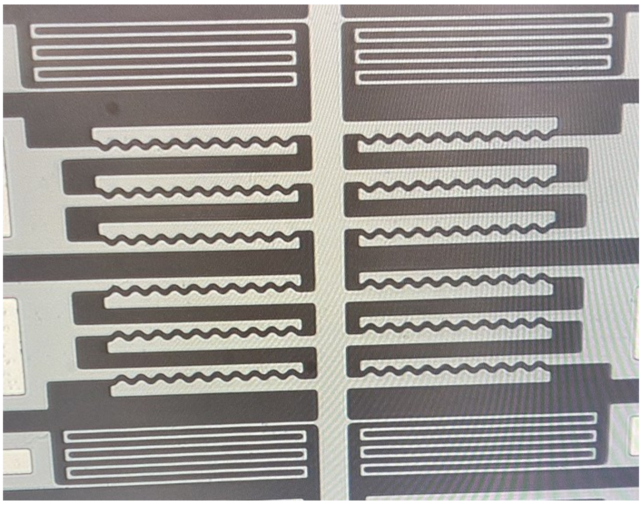

(b)

Figure. 5. 18**:** Micro-photographs of (SW4_2D_2S_2TL_7_V1) (a) One pare of Signal lines at ON State, (b) Both Signal lines at OFF State, “trapezoidal contact surface .

Figure. 5.15. shows the insertion loss for (a) the flat contact and (b) the trapezoidal contact. The operating frequency range for the flat contact is 1.2- 1.6 GHz while that for the trapezoidal contact is 1.3- 1.6 GHz.

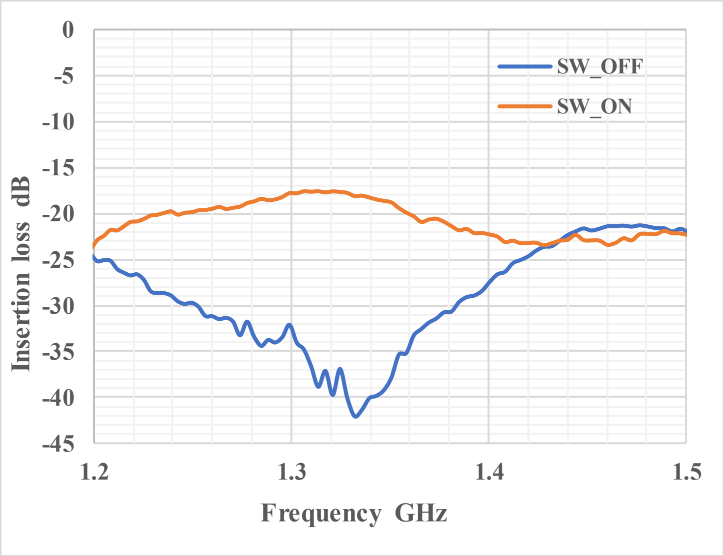

(a)

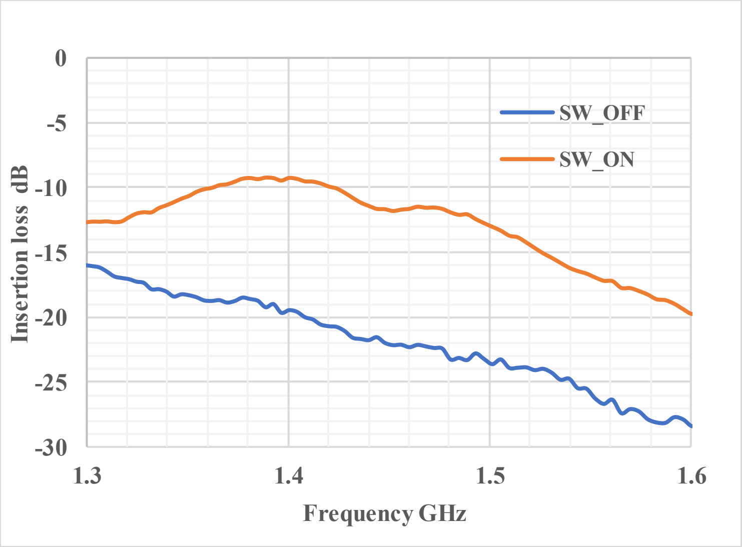

(b)

Figure. 5. 19: The insertion loss for (a) (SW2_2D_3S_FL_7_V4) the flat contact and (b) SW2_2D_3S_TL_7_V4 the trapezoidal contact.

5.6 Discussion

Experimental resistance measurements confirmed that these switches (two, and three state) have no electrical contact due to thin parasitic oxide which is formed on the surface of SOI structure. Furthermore, the coupling capacitance is most likely limited by the curved scallop profile resulting from DRIE process, employing a SEM microscope to take macro photos of the manufactured die, as seen in Figure. 5.20. The manufactured (SW2_2D_3S_FL_7_V4) SL flat contact profile's SEM picture in the OFF state is shown in Figure. 5.21.

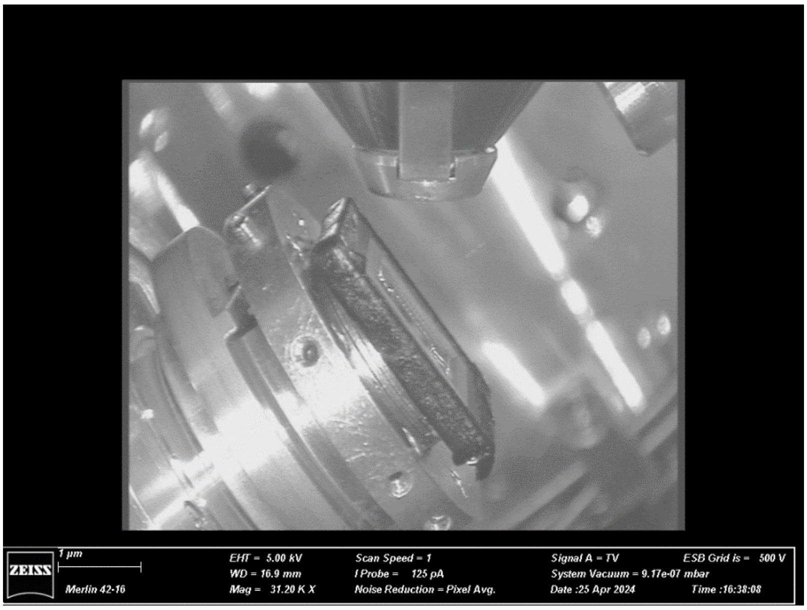

Figure. 5. 20**:** Scanning electron micrograph (SEM) of the fabricated die orientated 45°.

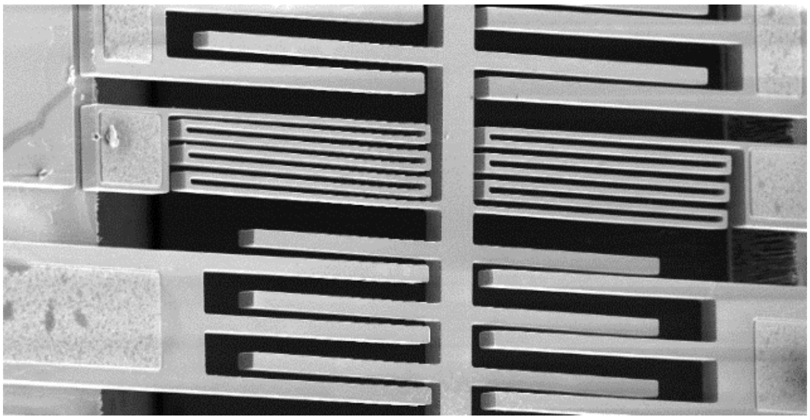

Figure. 5. 21**:** SEM Image of the fabricated (SW2_2D_3S_FL_7_V4) SL flat contact area.

Figure. 5.22 shows a vertical SEM image of the fabricated SL finger of (SW2_2D_3S_FL_7_V4) where the DRIE scallop profile is evident. From the SEM image, 30 scallops correspond to the 10 µm SOI thickness from which it can be deduced that the scallop diameter is 0.33 µm.

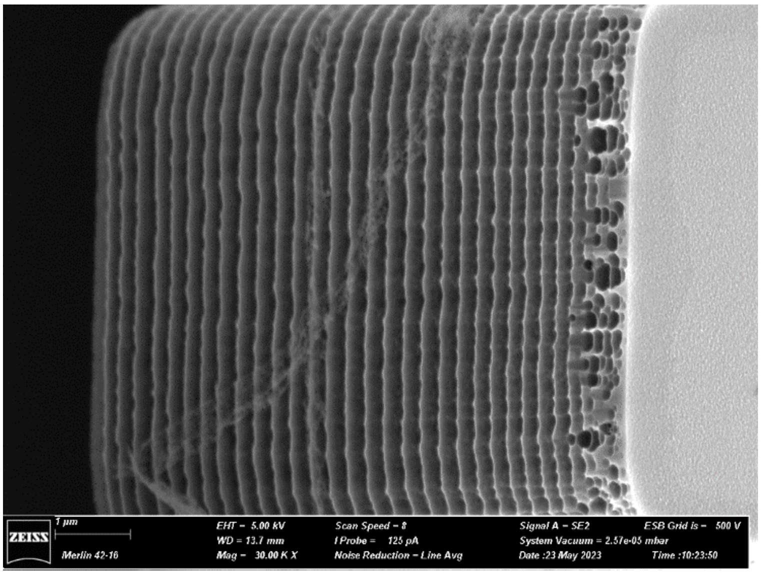

Figure. 5. 22**:** Vertical SEM Image of the fabricated Signal Line (SL) finger, showing the DRIE scallop profile.

In the ON state, the DRIE scallop tips of the SL fingers will be in mechanical contact, resulting in an air gap of approximately circular profile as shown in Figure. 5.23.

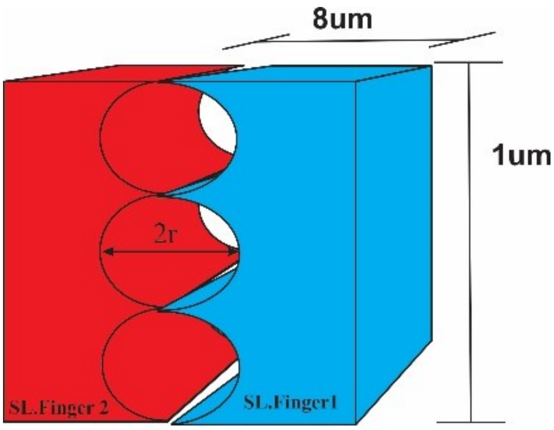

Figure. 5. 23: Diagram showing the two scalloped DRIE surfaces in contact, where the air gap diameter (2r) is estimated to be 0.33 µm.

Ignoring fringing effects, the corresponding capacitance value for one scallop section can be estimated as follows:

$$\boldsymbol{C} = \frac{\epsilon.\epsilon_r W}{2} \int_{-r}^{r} \frac{dx}{\sqrt{(r^2 - x^2)}} \tag{5.1}$$

where r is the scallop radius and W is the finger width.

This capacitance can be approximated by equivalent parallel plate capacitor having an air gap ğ of:

$$\boldsymbol{C} = \epsilon.\epsilon_r \frac{2rW}{\breve{g}} \tag{5.2}$$

In this case the parallel plate equivalent capacitor air gap ğ is found to be 0.21 µm.

FEM electrostatic simulations were subsequently carried out using the equivalent air gap of 0.21 µm for the ON state capacitance estimation of the three contact surface profiles (Flat, ZigZag and Trapezoidal). For the OFF state, the nominal air gap of 3 µm is used. Table.5.9 shows the corresponding capacitance values, for all signal fingers, obtained using FEM simulations.

Table.5. 9: Simulated capacitance values for different SL surface contact profiles in both OFF/ON states.

SL surface contact Profile	C_{OFF} (fF)	C_{ON} (fF)
a) Flat (SW2_2D_3S_FL_7_V4)	32.6	161.6
b) ZigZag (SW2_2D_3S_ZL_7_V4)	30.8	50.33
c) Trapezoidal (SW2_2D_3S_TL_7_V4	35.9	203.6

The capacitance reduction due to the parasitic oxide layer on the vertical surface of the SOI fingers is neglected since its contribution is minimal when compared to the air gap introduced by the scalloping DRIE surface as the permittivity of silicon oxide is relatively high and the oxide thickness is in the order of a few nm [128,129,130,131].

6. Conclusions and Future Work

6.1 Conclusions

The work presented in this dissertation has investigated the possibilities of applying PiezoMUMPs technology to the design and implementation of LBAW MEMS resonators that operate at 60 MHz in the VHF band. This work aimed to achieve an optimised design by investigating the effect of the resonator dimensions, number of electrodes, and tethers geometry on the resonant frequency including its Q_f, by means of FEM simulations. Results were validated by characterisation of several manufactured prototypes. Both the simulation and measured results showed that the PiezoMUMPs technology is applicable to the realisation of LBAW MEMS resonators to be used in VHF applications: this part was presented and discussed in detail in Chapter 3.

The investigation into fine-tuning methods, specifically thermal and voltage tuning, has shed light on the efficacy of these mechanisms in optimising the performance of LBAW MEMS resonators. The detailed study on thermal ovenisation tuning gave results that are in line with the theoretical expectations, highlighting its potential for enhancing the resonator's functionality. Additionally, the exploration of electrothermal tuning, particularly through SOI bulk electrothermal heating, provided valuable insights into alternative tuning approaches. This heating technique can possibly also be extended to resonator-based chemical sensors for resetting of chemically-functionalised films.

Voltage tuning results in limited range of about 30 kHz tuning range in comparison to thermal tuning which achieved a wider tuning range. The findings highlight the importance of selecting the most effective tuning method to achieve the desired performance for VHF LBAW PiezoMUMPs resonators. Furthermore, experimental results related to the three fine tuning techniques (ovenisation, on-chip thermal tuning and voltage tuning), which validated both analytical and simulation results were presented in Chapter 4

Besides fine frequency tuning techniques broad-band frequency tuning was investigated via the design of mechanical contact-type MEMS switches that can be integrated with piezo resonators utilising the same PiezoMUMPs process as discussed in Chapter 5. Integration of the MEMS switches on the same die as the resonators, results in a low-cost broadband tuning technique.

Part of the switch design work is to have a reliable operation by addressing stiction issues in the ON state using the bi-directionally actuated switches. The SOI DRIE process's intrinsic scalloping profile mostly affects the coupling capacitance of these switches. The performance changes as a function of various contact surface designs, was evaluated experimentally. The results show that the trapezoidal contact profile provides the best capacitive coupling in the ON state. It was observed that the OFF-to-ON signal coupling ratio is limited by the signal finger shape used in this work, indicating potential directions for future improvements by optimising the signal contact area and contact force via more complex signal contact surface patterns. Different switch topologies were considered including a double-throw switch to be able to switch between two frequency bands while using the same switch die area.

The fact that the designed switches were successfully fabricated represents a significant breakthrough in the field of RF MEMS switch resonators, demonstrating advancements in the integration of MEMS technology.

6.2 Future work

The impact of the tether dimensions and resonator shape on the device's resonant frequency and quality factor was investigated in depth. It was found that LBAW PiezoMUMPs resonators may operate in higher modes, such as the seventh and ninth modes, when the number of electrode components is increased. But in order to guarantee a high-quality factor, resonance in these higher modes requires modifications to the physical dimensions of the resonator. This specific study highlights the significance of meticulously optimising these factors for enhanced functionality and performance by illuminating the complex interaction between the resonant frequency, design parameters, and the quality factor of the resonators.

The existence of a parasitic oxide layer on the vertical surface of the SOI fingers causes a capacitance drop. This reduction is further aggravated because the air gap created by the scalloping deep reactive-ion etching (DRIE) surface outweighs the influence of the oxide layer. This is explained by the thickness of the oxide layer, which is usually on the order of a few nano metres, and the relatively high permittivity of the oxide layer.

Applying a layer of gold metal to the side walls is one recommended solution to this issue, where this gold layer deposition is an optional add-on to the existing PiezoMUMPs with extra cost. By reducing stiction-related problems, this extra layer of gold metal serves as a protective barrier, reducing the effects of the parasitic oxide layer and improving the overall performance and dependability of the switches [9].

The SOI electrothermal tuning technique can be extended beyond the RF application into the domain of resonator-based gas sensing: in these sensors the resonant frequency is shifted by a chemically-functionalised layer sensitive to a specific gas. Some chemically-functionalised layers can be reset to their original state by electrothermal heating. This is practically a straight-forward extension of the work carried out in this Ph.D. where chemically-functionalised polymer layers can be deposited onto the developed SOI-electrothermally heated resonator structures.

REFERENCES

[1] A. Potter, "Fabrication and Modelling of Piezoelectric RF MEMS Resonators", NSF Summer Undergraduate Fellowship in Sensor Technologies, University of Pennsylvania 2007.

[2] J.J. Yao, "RF MEMS from a Device Perspective", Journal of Micromechanics and Microengineering, vol. 10, pp. 9-38, 2000.

[3] R. Farrugia et al, "Performance analysis of an RF MEMS TPoS resonator using FE modelling," in 2015 Symposium on Design, Test, Integration and Packaging of MEMS/MOEMS (DTIP), DOI:10.1109/DTIP.2015.7161004,2015.

[4] S. Pourkamali, G. K. Ho, and F. Ayazi, "Vertical capacitive SiBARs," 18th IEEE Int. Conf. Micro Electro Mechanical Syst. (MEMS 2005), Jan-Feb 2005, pp. 211–214.

[5] R. Abdolvand et al, "Micromachined Resonators: A Review," Micromachines (Basel), vol. 7, (9), pp. 160, 2016. DOI: 10.3390/mi7090160.

[6] R. C. Ruby et al, "Thin film bulk wave acoustic resonators (FBAR) for wireless applications," in Ultrasonics Symposium, , DOI: 10.1109/ULTSYM.2001.991846, 2001.

[7] A. Cowen, G. Hames, K. Glukh and B. Hardy, "PiezoMUMPs Design Handbook", MEMSCAP Inc, vol. 1, 2014.

[8] J. Park et al, "A non-contact-type RF MEMS switch for 24-GHz radar applications," J Microelectromech Syst, vol. 18, (1), pp. 163-173, 2009.

[9] J. Pal et al, "A novel three-state contactless RF micromachined switch for wireless applications," IEEE Electron Device Lett., vol. 36, (12), pp. 1363-1365, 2015.

[10] B. Sviličića , "Tunability of Piezoelectric MEMS Ring Resonator Based Filter", Procedia Engineering, vol. 168, pp. 1517-1520, 2016.

[11] X. Lia, Y. Huanga, Y. Dub, Z. Lib, F. Baoa, J. Baoa, "Study of a 10 MHz MEMS oscillator with a TPoS resonator", Sensors and Actuators A: Physical Volume 258, Pages 59-67, 2017.

[12] A. Tazzoli, M. Rinaldi and G. Piazza, "Ovenized high frequency oscillators based on aluminum nitride contour-mode MEMS resonators", 2011 International Electron Devices Meeting, IEEE, DOI:10.1109/IEDM.2011.61315892011.

[13] W. Zhang, K. Hu, Z. Peng and G. Meng, "Tunable micro-and nanomechanical resonators", Sensors, vol. 15, (10), pp. 26478-26566, 2015.

---

[14] A. S. Algamili et al, "A Review of Actuation and Sensing Mechanisms in MEMS-Based Sensor Devices," Nanoscale Res Lett, vol. 16, (1), pp. 16, 2021. DOI: 10.1186/s11671-021-03481-7.

[15] R. de Oliveira Hansen et al, "Magnetic films for electromagnetic actuation in MEMS switches," Microsyst Technol, vol. 24, (4), pp. 1987-1994, 2017. DOI: 10.1007/s00542-017-3595-2.

[16] S. Siahpour, M. M. Zand and M. Mousavi, "Dynamics and vibrations of particle-sensing MEMS considering thermal and electrostatic actuation,".
DOI: 10.1007/s00542-017-3554-y.

[17] S. S. Ba Hashwan et al, "Recent Progress in the Development of Biosensors for Chemicals and Pesticides Detection," Access, vol. 8, pp. 82514-82527, 2020.

[18] S. Sathya et al, "Design of capacitance based on interdigitated electrode for BioMEMS sensor application," Materials Science in Semiconductor Processing, vol. 101, pp. 206-213, 2019.DOI: 10.1016/j.mssp.2019.06.005.

[19] R. S. Zoll et al, "MEMS-Actuated Carbon Fiber Microelectrode for Neural Recording," 2018. DOI: 10.1101/385153.

[20] A. M. Basuwaqi et al, "Effects of frequency and voltage on the output of CMOS-MEMS device," in Oct 2017, DOI:10.1109/PRIMEASIA.2017.8280361.

[21] J. Dennis, A. Ahmed and M. Khir, "Fabrication and Characterization of a CMOS-MEMS Humidity Sensor," Sensors (Basel, Switzerland), vol. 15, (7), pp. 16674-16687, 2015. DOI: 10.3390/s150716674.

[22] D. Wang et al, "Non-destructive On-Site Detection of Soybean Contents Based on An Electrothermal MEMS Fourier Transform Spectrometer," Jphot, vol. 11, (3), pp. 1-10, 2019. DOI: 10.1109/JPHOT.2019.2920273.

[23] B. Svili, E. Mastropaolo and R. Cheung, "Electrothermal actuation of mems resonator-based filters with piezoelectric sensing," in 2016 Progress in Electromagnetic Research Symposium (PIERS), 2016.

[24] B. Sviličić, E. Mastropaolo and R. Cheung, "Widely tunable MEMS ring resonator with electrothermal actuation and piezoelectric sensing for filtering applications," Sensors and Actuators. A. Physical., vol. 226, pp. 149-153, 2015.

[25] X. Lv et al, "A novel MEMS electromagnetic actuator with large displacement," Sensors and Actuators. A. Physical., vol. 221, pp. 22-28, 2015. DOI: 10.1016/j.sna.2014.10.028.

[26] P. Joshi et al, "Distributed MEMS Mass-Sensor Based on Piezoelectric Resonant Micro-Cantilevers," Jmems, vol. 28, (3), pp. 382-389, 2019. DOI: 10.1109/JMEMS.2019.2908879.

[27] N. Maluf and K. Williams, An Introduction to Microelectromechanical Systems Engineering. 2004. Book

[28] Younis MI (2011), MEMS linear and nonlinear statics and dynamics. Springer, Berlin.

[29] A. Elshenety et al, "A flexible model for studying fringe field effect on parallel plate actuators," Journal of Electrical Systems and Info Technology, vol. 7, (1), pp. 1-14, 2020. DOI: 10.1186/s43067-020-00022-7.

[30] Allen JJ (2005) Micro electro mechanical system design. CRC Press, Cambridge.

[31] G. N. Nielson and G. Barbastathis, "Dynamic Pull-in of parallel-plate and torsional electrostatic MEMS actuators," Jmems, vol. 15, (4), pp. 811-821, 2006. DOI: 10.1109/JMEMS.2006.879121.

[32] S. Yang and Q. Xu, "A review on actuation and sensing techniques for MEMS-based microgrippers," J Micro-Bio Robot, vol. 13, (1-4), pp. 1-14, 2017. DOI: 10.1007/s12213-017-0098-2.

[33] R. Costa Castelló, A. M. Shkel and A. Fargas Marquès. Modelling the electrostatic actuation of MEMS: State of the art 2005. Universitat Politècnica de Catalunya, 2005.

[34] L. Ma et al, "Comprehensive Study on RF-MEMS Switches Used for 5G Scenario," 2019. DOI: 10.1109/ACCESS.2019.2932800.

[35] A. Nikpourian, M. R. Ghazavi and S. Azizi, "Size-dependent nonlinear behaviour of a piezoelectrically actuated capacitive bistable microstructure," Int. J. Non-Linear Mech., vol. 114, pp. 49-61, 2019.

[36] G. Rezazadeh, A. Tahmasebi and M. Zubstov, "Application of piezoelectric layers in electrostatic MEM actuators: controlling of Pull-in voltage," Microsystem Technologies, vol. 12, (12), pp. 1163-1170, 2006.

[37] R. Nuryadi et al, "Resonance frequency change in microcantilever-based sensor due to humidity variation," in Materials Science Forum, 2013.

[38] J. Xu et al, "Piezoresistive microcantilevers for humidity sensing," J Micromesh Microengineering, vol. 29, (5), pp. 053003, 2019.

[39] R. Abdolvand, “Thin-Film- Piezoelectric on Substrate Resonators and Narrowband Filters", Ph.D thesis in School of Electrical and Computer Engineering Georgia Institute of Technology, 2008.

[40] S. Gao, H. Ao and H. Jiang, "Properties and performance of general piezoelectric materials on a novel cantilevered energy harvester," in IOP Conference Series: Materials Science and Engineering, 2019.

[41] I. F. Rivera, RF MEMS Resonators for Mass Sensing Applications. 2015.

[42] H. Bhugra and G. Piazza, Piezoelectric MEMS Resonators. 2017.

[43] M. A. Fraga et al, "Wide bandgap semiconductor thin films for piezoelectric and piezoresistive MEMS sensors applied at high temperatures: an overview," Microsystem Technologies, vol. 20, (1), pp. 9-21, 2014.

[44] G. Piazza, P. J. Stephanou and A. P. Pisano, "Piezoelectric Aluminum Nitride Vibrating Contour-Mode MEMS Resonators," Departmental Papers (ESE), pp. 223, 2006.

[45] H. Chandrahalim, S. Bhave, R. Polcawich, J. Pulskamp, D. Judy, R.Kaul, M. Dubey, “Influence of Silicon on Quality Factor, Motional Impedance and Tuning Range of PZT-Transduced Resonators”, in Solid-State Sensors, Actuators, and Microsystems Workshop, Hilton Head, 2008, pp. 360 – 363.

[46] H. Fatemi, M. Shahmo hammadi and R. Abdolvand, "Ultra-stable nonlinear thin-film piezoelectric-on-substrate oscillators operating at bifurcation," in Micro Electro Mechanical Systems (MEMS), 2014 IEEE 27th International Conference, DOI:10.1109/MEMSYS.2014.6765884 2014,

[47] M. Rinaldi, C. Zuniga and G. Piazza, "5-10 GHz AlN Contour-Mode nanoelectromechanical Resonators," Departmental Papers (ESE), pp. 493, 2009.

[48] S. D. Senturia, Microsystem Design. 2007. Book

[49] M. L. Johnston, " Thin-Film Bulk Acoustic Resonators on Integrated Circuits for Physical Sensing Applications", Ph.D thesis , 2012.

[50] O. Brand et al, Resonant MEMS: Fundamentals, Implementation, and Application. 2015.

[51] G. Piazza, P. J. Stephanou, and A. P. Pisano, "One and two port piezoelectric higher order contour-mode MEMS resonators for mechanical signal processing," Solid-State Electronics, vol. 51, (11-12), pp. 1596-1608, 2007.

[52] M. Rinaldi et al, "Super-high-frequency two-port AlN contour-mode resonators for RF applications," IEEE Trans. Ultrason. Ferroelectr. Freq. Control, vol. 57, (1), pp. 38-45, 2010.

[53] G. Piazza and A. P. Pisano, "Two-port stacked Piezoelectric Aluminium Nitride Contour-Mode Resonant MEMS," Sensors and Actuators A: Physical, vol. 136, (2), pp. 638-645, 2007.

[54] J. D. Larson et al, "Modified Butterworth-van dyke circuit for FBAR resonators and automated measurement system," in 2000, DOI:10.1109/ULTSYM.2000.922679.

[55] J. E. Lee, J. Yan and A. A. Seshia, "Low loss HF band SOI wine glass bulk mode capacitive square-plate resonator," J Micromech Microengineering, vol. 19, (7), pp. 074003, 2009.

[56] A. N. Cleland and M. L. Roukes, "A nanometre-scale mechanical electrometer," Nature, vol. 392, (6672), pp. 160-162, 1998.

[57] A. Ballato et al, "Dissipation in ceramic resonators and transducers," , DOI: 10.1109/FREQ.1996.5598831996.

[58] A. T. Lin, J. Yan and A. A. Seshia, "Electrostatically transduced face-shear mode silicon MEMS microresonator," in 2010 IEEE International Frequency Control Symposium, 2010.

[59] J. Lee and A. A. Seshia, "5.4-MHz single-crystal silicon wine glass mode disk resonator with quality factor of 2 million," Sensors and Actuators A: Physical, vol. 156, (1), pp. 28-35, 2009.

[60] K. Uchino and S. Hirose, "Loss mechanisms in piezoelectric: how to measure different losses separately," IEEE Trans. Ultrasonicc. Ferroelectric. Freq. Control, vol. 48, (1), pp. 307-321, 2001.

[61] J. Baborowski et al, "Piezoelectrically activated silicon resonators," in 2007 IEEE International Frequency Control Symposium Joint with the 21st European Frequency and Time Forum, DOI: 10.1109/FREQ.2007.4319269, 2007.

[62] M. W. U. Siddiqi, C. Tu and J. E. Lee, "Effect of mode order, resonator length, curvature, and electrode coverage on enhancing the performance of biconvex resonators," J Micromech Microengineering, vol. 28, (9), pp. 094002, 2018.

[63] R. Lifshitz and M. L. Roukes, "Thermoelastic damping in micro-and nanomechanical systems," Physical Review B, vol. 61, (8), pp. 5600, 2000.

[63] R. Abdolvand et al, "Thin-film piezoelectric-on-silicon resonators for high-frequency reference oscillator applications," IEEE Trans. Ultrasonic. Ferroelectric.

Freq. Control, vol. 55, (12), pp. 2596-2606, 2008.

[65] J. G. Smits, "Eigenstates of coupling factor and loss factor of piezoelectric ceramics,"; 205 pp; Includes Dutch summary: 154 refs, 7 Sep 1978.

[66] S. Definitions, "Methods of Measurement for Piezoelectric Vibrators," DOI: 10.1109/IEEESTD.1966.120168,1966.

[67] G. K. Ho et al, "Piezoelectric-on-silicon lateral bulk acoustic wave micromechanical resonators", J Microelectromech Syst, vol. 17, (2), pp. 512-520, 2008.

[68] S. Gong, N. Kuo and G. Piazza, "GHz AlN lateral overmoded bulk acoustic wave resonators with af· Q of 1.17× 10 13," in 2011 Joint Conference of the IEEE International Frequency Control and the European Frequency and Time Forum (FCS) Proceedings, DOI:10.1109/FCS.2011.5977846, 2011.

[69] T. Manzaneque et al, "Piezoelectric MEMS resonator-based oscillator for density and viscosity sensing," Sensors and Actuators A: Physical, vol. 220, pp. 305-315, 2014.

[70] G. Piazza, P. J. Stephanou, and A. P. Pisano, "Single-chip multiple-frequency ALN MEMS filters based on contour-mode piezoelectric resonators," J Microelectromech Syst, vol. 16, (2), pp. 319-328, 2007.

[71] F. Ayazi, "MEMS for integrated timing and spectral processing," in 2009 IEEE Custom Integrated Circuits Conference, DOI: 10.1109/CICC.2009.5280888, 2009.

[72] F. Ayazi, R. Tabrizian and L. Sorenson, "Compensation, tuning, and trimming of MEMS resonators," in 2012 IEEE International Frequency Control Symposium Proceedings, 2012.

[73] F. Ayazi, L. Sorenson, R. Tabrizian, ‘Energy dissipation in micromechanical resonators. Micro-and Nanotechnology Sensors’, DOI: 10.1117/12.884731, 2011.

[74] K. Hashimoto, RF Bulk Acoustic Wave Filters for Communications, ISBN: 9781596933217, 2009.Book

[75] R. Tabrizian and F. Ayazi, "Tunable silicon bulk acoustic resonators with multi-face AlN transduction," in the Conference of the IEEE International Frequency Control and the European Frequency and Time Forum (FCS) Proceedings, DOI:10.1109/FCS.2011.5977886, 2011.

[76] J. C. Salvia et al, "Real-Time Temperature Compensation of MEMS Oscillators using an integrated micro-oven and a phase-locked loop," J Microelectromech Sys, vol. 19, (1), pp. 192-201, 2010.

[77] M. Shahmohammadi et al, "Passive tuning in lateral-mode thin-film piezoelectric oscillators," in the Conference of the IEEE International Frequency Control and the European Frequency and Time Forum (FCS) Proceedings, DOI: 10.1109/FCS.2011.59 773032011.

[78] H. M. Lavasani, W. Pan and F. Ayazi, "An electronically temperature-compensated 427MHz low phase-noise AlN-on-Si micromechanical reference oscillator," in the IEEE Radio Frequency Integrated Circuits Symposium, DOI: 10.1109/RFIC.2010.5477392 2010.

[79] W. Hsu and A. R. Brown, "Frequency trimming for MEMS resonator oscillators," in 2007 IEEE International Frequency Control Symposium Joint with the 21st European Frequency and Time Forum, DOI: 10.1109/FREQ.2007.43192472007.

[80] A. Hajjam et al, "A self-controlled frequency trimming technique for micromechanical resonators," in Proc. Solid-State Sensor, Actuator., Micro syst. Workshop, DOI: 10.31438/TRF.HH2012.19,2012.

[81] A. K. Samarao and F. Ayazi, "Post-fabrication electrical trimming of silicon bulk acoustic resonators using joule heating," in 2009 IEEE 22nd International Conference on Micro Electro Mechanical Systems, DOI: 10.1109/MEMSYS.2009.4805527,2009.

[82] H. Chandrahalim et al, "Influence of silicon on quality factor motional impedance and tuning range of PZT-transduced resonators," in 2008 Solid State Sensor, Actuator and Microsystems Workshop, DOI: 0-9640024-7-7/HH2008, 2008.

[83] B. Kim, R. H. Olsson and K. E. Wojciechowski, "Ovenized and Thermally Tunable Aluminum Nitride Microresonators," IEEE International Ultrasonics Symposium, DOI: 10.1109/ULTSYM.2010.5935635, 2010.

[84] D. E. Serrano, R. Tabrizian and F. Ayazi, "Tunable piezoelectric MEMS resonators for real-time clock," IEEE International Frequency Control and the European Frequency and Time Forum (FCS) Proceedings, DOI: 10.1109/FCS.2011.5977885, 2011.

[85] H. Fatemi, M. J. Modarres-Zadeh and R. Abdolvand, "Passive wireless temperature sensing with piezoelectric MEMS resonators," in 2015 28th IEEE International Conference on Micro Electro Mechanical Systems (MEMS), 2015.

[86] J. Pons-Nin et al, "Design and test of resonators using PiezoMUMPs technology," in 2014 Symposium on Design, Test, Integration and Packaging of MEMS/MOEMS (DTIP), DOI: 10.1109/DTIP.2014.7056666, 2014.

[87] C. Trigona et al, "Design and Characterization of PiezoMUMPs Microsensors with Applications to Environmental Monitoring of Aromatic Compounds via Selective Supramolecular Receptors," Procedia Engineering, vol. 87, pp. 1190-1193, 2014.

[88] H. Fatemi, M. J. Modarres-Zadeh and R. Abdolvand, "Passive wireless temperature sensing with piezoelectric MEMS resonators," in 2015 28th IEEE International Conference on Micro Electro Mechanical Systems (MEMS), 2015.

[89] L. L. Wong et al, "A feasibility study of piezoelectric micromachined ultrasonic transducers fabrication using a multi-user MEMS process," Sensors and Actuators A: Physical, vol. 247, pp. 430-439, 2016.

[90] CoventprWare, using ConentorWareDoc Ver 2010.000 Rev A Compatible with CoventorWare version 2010.000, © Coventor, Inc., 2010

[91] M. M. Saleem and H. Nawaz, "A systematic review of reliability issues in RF-MEMS switches," Micro and Nano systems, vol. 11, (1), pp. 11-33, 2019.

[92] J. J. Yao and M. Chang, "Surface micromachined miniature switch for telecommunications applications with signal frequencies from DC up to 4 GHZ," in Proceedings of the 1995 8th International Conference on Solid-State Sensors and Actuators and Euro sensors IX. Part 1 (of 2), 1995.

[93] Z. J. Yao et al, "Micromachined low-loss microwave switches," J Microelectromech Syst, vol. 8, (2), pp. 129-134, 1999.

[94] S. P. Pacheco, L. P. Katehi and C. Nguyen, "Design of low actuation voltage RF MEMS switch," in 2000 IEEE MTT-S International Microwave Symposium Digest (Cat. no. 00CH37017), 2000.

[95] J. Y. Park et al, "Monolithically integrated micromachined RF MEMS capacitive switches," Sensors and Actuators A: Physical, vol. 89, (1), pp. 88-94, 2001. DOI: https://doi.org/10.1016/S0924-4247(00)00549-5.

[96] J. Kim et al, "A mechanically reliable digital-type single crystalline silicon (SCS) RF MEMS variable capacitor," J Micromech Microengineering, vol. 15, (10), pp. 1854, 2005.

[97] A. Q. Liu et al, "Low-loss lateral micromachined switches for high frequency applications," J Micromech Microengineering, vol. 15, (1), pp. 157, 2004.

[98] F. Ke, J. Miao and J. Oberhammer, "A ruthenium-based multi metal-contact RF MEMS switch with a corrugated diaphragm," J Microelectromech Syst, vol. 17, (6), pp. 1447-1459, 2008.

[99] J. Kim et al, "Electrostatically driven low-voltage micromechanical RF switches using robust single-crystal silicon actuators," J Micromech Microengineering, vol. 20, (9), pp. 095007, 2010.

[100] H. U. Rahman, K. Y. Chan and R. Ramer, "Cantilever beam designs for RF MEMS switches," J Micromesh Microengineering, vol. 20, (7), pp. 075042, 2010.

[101] B. Liu et al, "Improving performance of the metal-to-metal contact RF MEMS switch with a Pt–Au micro spring contact design," J Micromech Microengineering, vol. 21, (6), pp. 065038, 2011.

[102] R. Stefanini et al, "Miniature MEMS switches for RF applications," J Microelectromech Syst, vol. 20, (6), pp. 1324-1335, 2011.

[103] S. Jaibir, K. Nagendra and D. Amitava, "Fabrication of low Pull-in voltage RF MEMS switches on glass substrate in recessed CPW configuration for V-band application," J Micromech Microengineering, vol. 22, (2), pp. 025001, 2012.

[104] A. Persano et al, "Reliability enhancement by suitable actuation waveforms for capacitive RF MEMS switches in III–V technology," J Microelectromech Syst, vol. 21, (2), pp. 414-419, 2011.

[105] D. Bansal et al, "Design of novel compact anti-stiction and low insertion loss RF MEMS switch," Microsystem Technologies, vol. 20, (2), pp. 337-340, 2014.

[106] D. Bansal et al, "Design of compact and wide bandwidth SPDT with anti-stiction torsional RF MEMS series capacitive switch," Microsystem Technologies, vol. 21, (5), pp. 1047-1052, 2015.

[107] M. Angira and K. Rangra, "Design and investigation of a low insertion loss, broadband, enhanced self and hold down power RF-MEMS switch," Microsystem Technologies, vol. 21, (6), pp. 1173-1178, 2015.

[108] M. Angira and K. Rangra, "A novel design for low insertion loss, multi-band RF-MEMS switch with low Pull-in voltage," Engineering Science and Technology, an International Journal, vol. 19, (1), pp. 171-177, 2016.

[109] A. Persano et al, "On the electrostatic actuation of capacitive RF MEMS switches on GaAs substrate," Sensors and Actuators A: Physical, vol. 232, pp. 202-207, 2015.

[110] S. Sim et al, "A 50–100 GHz ohmic contact SPDT RF MEMS silicon switch with dual axis movement," Microelectronic Engineering, vol. 162, pp. 69-74, 2016.

[111] A. G. Nair and E. S. Shajahan, "Design and simulation of radio frequency micro electro mechanical capacitive shunt switches," Procedia Computer Science, vol. 93, pp. 217-222, 2016.

[112] A. Chakraborty and B. Gupta, "Utility of RF MEMS miniature switched capacitors in phase shifting applications," AEU-International Journal of Electronics and Communications, vol. 75, pp. 98-107, 2017.

[113] H. Wei et al, "High on/off capacitance ratio RF MEMS capacitive switches," J Micromech Microengineering, vol. 27, (5), pp. 055002, 2017.

[114] M. Li et al, "Design and fabrication of a low insertion loss capacitive RF MEMS switch with novel micro-structures for actuation," Solid-State Electronics, vol. 127, pp. 32-37, 2017.

[115] S. Molaei and B. A. Ganji, "Design and simulation of a novel RF MEMS shunt capacitive switch with low actuation voltage and high isolation," Microsystem Technologies, vol. 23, pp. 1907-1912, 2017.

[116] H. R. Ansari and S. Khosroabadi, "Design and simulation of a novel RF MEMS shunt capacitive switch with a unique spring for Ka-band application," Microsystem Technologies, vol. 25, (2), pp. 531-540, 2019.

[117] H. Saleh et al, "Low actuation voltage cantilever-type RF-MEMS shunt switches for 5G applications," Microelectronics Reliability, vol. 136, pp. 114645, 2022.

[118] Doc Ver 10.1 Rev A Compatible with CoventorWare version 10.1

[119] F. Ayazi, R. Tabrizian and L. Sorenson, "Compensation, tuning, and trimming of MEMS resonators," in 2012 IEEE International Frequency Control Symposium Proceedings, DOI: 10.1109/FCS.2012.6243717, 2012.

[120] M. Bengashier, I. Grech, O. Casha, B. Portelli, R. Farrugia and E. Gatt, "A Feasibility Study on Piezoelectric MEMS Lateral Bulk Acoustic Wave Resonators including Thermal Effect," 2019 Symposium on Design, Test, Integration & Packaging of MEMS and MOEMS (DTIP), Paris, France, 2019.

[121] M. Bengashier, I. Grech, O. Casha, B. Portelli, and R. Farrugia, "Experimental Validation Of Tuning Mechanisms Applied On AlN Piezoelectric Contour Mode Mems Resonators", 2020 Symposium on Design, Test, Integration & Packaging of MEMS and MOEMS (DTIP*)*, Paris, France 2020.

[122] E.J. Boyd, L. Li, R. Blue and D. Uttamchandani, “Measurement of the temperature coefficient of Young's modulus of single crystal silicon and 3C silicon carbide below 273 K using micro-cantilevers”, Journal of Sensors and Actuators A: Physical, vol. 198, pp. 75-80, 2013.

[123] U. Gysin, S. Rast, P. Ruff, E. Meyer, D. W. Lee, P. Vettiger, C. Gerber, “Temperature Dependence of the Force Sensitivity of Silicon Cantilevers," Physical Review B, vol. 69, (4), pp. 045403, 2004.

[124] E. Iervolino, M. Riccio, F.Santagata, J.Wei, A.W. van Herwaarden, A. Irace, G. Breglio, P.M. Sarro, “Resonance Frequency of Locally Heated Cantilever Beams", Journal of Sensors and Actuators A: Physical, vol. 190, pp. 6-12, February 2013.

[125] MEMS design and Tutorials, Application Notes, Physical and System-Level Design Tutorials, Coventorware@2012.www.coventor.com.

[126] M. Bengashier, I. Grech, O. Casha, R. Farrugia and B. Portelli, "Investigation of a Mechanical Contact Type RF-MEMS Switch for VHF Band Applications," 2021 Symposium on Design, Test, Integration & Packaging of MEMS and MOEMS (DTIP), Paris, France, 2021.

[127] M. Bengashier, I. Grech, O. Casha, R. Farrugia and B. Portelli, "Investigation of a Mechanical Contact Type RF-MEMS Switch for VHF Band Applications," 2023 Symposium on Design, Test, Integration & Packaging of MEMS and MOEMS (DTIP), Valletta, Malta.

[128] Tian W, Li P, Yuan L. "Research and analysis of MEMS switches in different frequency bands". Micromachines. 2018 Apr; 9(4):185.

[129] D. Yang et al, "Room temperature oxidation kinetics of Si nanoparticles in air, determined by x-ray photoelectron spectroscopy," J. Appl. Phys., vol. 97, (2), 2005.

[130] J. Kiihamäki, Fabrication of SOI Micromechanical Devices. 2005.

[131] Y. C. Choi et al, "The improvement of performance through minimizing scallop size in MEMS based micro wind turbine," Micromachines, vol. 12, (10), pp. 1261, 2021.